



A Review on Interface Engineering of MXenes for Perovskite Solar Cells

Cite as

Nano-Micro Lett.
(2023) 15:123

Srikanta Palei¹, G. Murali², Choong-Hee Kim¹, Insik In² ✉, Seul-Yi Lee¹ ✉, Soo-Jin Park¹ ✉

Received: 27 January 2023

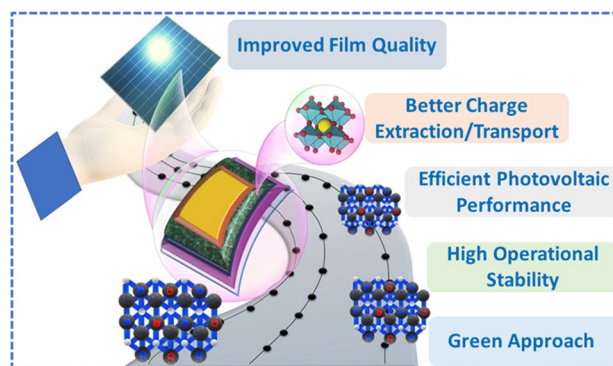
Accepted: 21 March 2023

© The Author(s) 2023

HIGHLIGHTS

- This review discusses the roles of MXenes in different positions/layers in perovskite solar cells.
- The issues in different layers/interfaces and their addressal with the incorporations of MXenes in perovskite solar cells are elaborately discussed.

ABSTRACT With an excellent power conversion efficiency of 25.7%, closer to the Shockley–Queisser limit, perovskite solar cells (PSCs) have become a strong candidate for a next-generation energy harvester. However, the lack of stability and reliability in PSCs remained challenging for commercialization. Strategies, such as interfacial and structural engineering, have a more critical influence on enhanced performance. MXenes, two-dimensional materials, have emerged as promising materials in solar cell applications due to their metallic electrical conductivity, high carrier mobility, excellent optical transparency, wide tunable work function, and superior mechanical properties. Owing to different choices of transition elements and surface-terminating functional groups, MXenes possess the feature of tuning the work function, which is an essential metric for band energy alignment between the absorber layer and the charge transport layers for charge carrier extraction and collection in PSCs. Furthermore, adopting MXenes to their respective components helps reduce the interfacial recombination resistance and provides smooth charge transfer paths, leading to enhanced conductivity and operational stability of PSCs. This review paper aims to provide an overview of the applications of MXenes as components, classified according to their roles as additives (into the perovskite absorber layer, charge transport layers, and electrodes) and themselves alone or as interfacial layers, and their significant importance in PSCs in terms of device performance and stability. Lastly, we discuss the present research status and future directions toward its use in PSCs.



KEYWORDS MXenes; Perovskite solar cells; Additives; Interfacial layer; Electrodes

✉ Insik In, in1@ut.ac.kr; Seul-Yi Lee, leesy1019@inha.ac.kr; Soo-Jin Park, sjpark@inha.ac.kr

¹ Department of Chemistry, Inha University, 100 Inharo, Incheon 22212, South Korea

² Department of Polymer Science and Engineering, Department of IT-Energy Convergence (BK21 Four), Chemical Industry Institute, Korea National University of Transportation, Chungju 27469, South Korea



1 Introduction

Solar technology converts solar energy directly into electrical energy through photovoltaic cells. Solar cells have attracted great attention from the energy community to meet the increasing demand for sustainable green, and clean energy sources. Apart from wafer-based Si solar cells that are widely available on the market, perovskite solar cells (PSCs) have achieved the highest power conversion efficiency (PCE) of 25.7% in 2021, which is inching towards the theoretical efficiency of about 31% [1–3]. Furthermore, a recent study shows halide PSCs can surpass the Shockley-Queisser (SQ) PCE limit of 33.7% (predicted for a single-junction solar cell) [4]. Most importantly, PSCs are in an advantageous position for ease of fabrication and their affordable cost coming from solution-based processing [5–7].

Perovskite materials, such as MAPbI₃, FAPbI₃, and CsPbI₃, have been spotlighted due to their excellent bandgap tunability, excellent light absorption *co*-efficient ($> 10^5 \text{ cm}^{-1}$), good charge carrier mobility ($2\text{--}40 \text{ cm}^2 \text{ V}^{-1} \text{ s}^{-1}$), and long carrier-diffusion length in the PSCs. Despite the stellar performance, the perovskite device remains a long-standing issue due to the structural and chemical instability originating from the degradation factors related to the intrinsic shortcomings of the perovskite materials as well as at their interfaces. Researchers have explored various pathways to improve stability and performance efficiency, for instance, the development of passivating materials, enlargement of the grain sizes or single crystals, solvent engineering, additive engineering, and interface engineering [6, 8–13].

Recently, MXenes, as emerging two-dimensional (2D) layered materials, have drawn interest in various applications, including photocatalysts, light emitting diodes, transparent electrodes, nanofiltration, water purification, electromagnetic interference shielding, antibacterial activity, supercapacitors, sensors, and more [14–22]. 2D nanomaterials such as graphene, *g*-C₃N₄, WS₂, MoS₂, and black phosphorous have been demonstrated as potential additives in the perovskite absorber layer in PSCs owing to their excellent electrical and optical properties [23–28]. MXenes have been used as all-round materials starting from additives, electron transport layers (ETL), hole transport layers (HTL), and interfacial layers to electrodes in

PSCs due to their excellent electrical conductivity ($2 \times 10^4 \text{ S cm}^{-1}$), high charge carrier density ($3.8 \times 10^{22} \text{ cm}^{-3}$), high mobility ($1 \text{ cm}^2 \text{ V}^{-1} \text{ s}^{-1}$), high transparency, and tunable work function (WF) through controlled surface chemistry [29, 30]. With the introduction of Ti₃C₂T_x MXene into MAPbI₃-based perovskite solar cells in 2018, there has been a tremendous surge in the use of MXenes in the photovoltaic community [31].

In this review, we aim to provide a comprehensive understanding of MXenes and their roles as additives or themselves alone in different components (classified according to photoactive absorber layer, ETL, HTL, and electrodes) and interfaces of the PSCs. In Sect. 1, we begin by introducing a brief overview of the recent research trend of PSCs. In Sect. 2, we have classified MXenes according to their roles as additives (into perovskite absorber layer, charge transport layers, and electrodes) and themselves alone in PSCs. In Sect. 3, we discuss MXenes as an interfacial layer on each layer of PSCs, followed by a discussion of MXenes' roles in improving morphological features, electrical conductivity, mechanical stability, and WF tuning to impact electron transfer and extraction mechanism and thereby increasing the operational stability of PSCs. In Sect. 4, we suggest the future direction of an interfacial design/engineering that will realize the advent of an overarching framework for advanced PSC technology.

2 MXenes in Perovskite Solar Cells

2.1 Synthesis of MXenes

MXenes are 2D transition metal carbides, nitrides, and carbonitrides with the general formula $M_{n+1}X_nT_x$ ($n = 1\text{--}4$), where 'M' represents an early transition metal (Sc, Ti, Zr, Hf, V, Nb, Ta, Cr, Mo, etc.), 'X' represents carbon and/or nitrogen, and 'T_x' stands for the surface terminations including $-\text{O}$, $-\text{OH}$, $-\text{F}$, etc. [32–34]. In 2011, Ti₃C₂T_x MXene was first reported by Naguib et al. [35]. MXenes with a distinct combination of M and X elements, number of elements at M or X sites (solid solutions at M or X sites, $(M', M'')_{n+1}X_nT_x$, where M' and M'' are two different metals), number of atomic layers (*n*), ordering (in-plane or *i*-MXene or out-of-plane or *o*-MXene) of atoms, and compositions

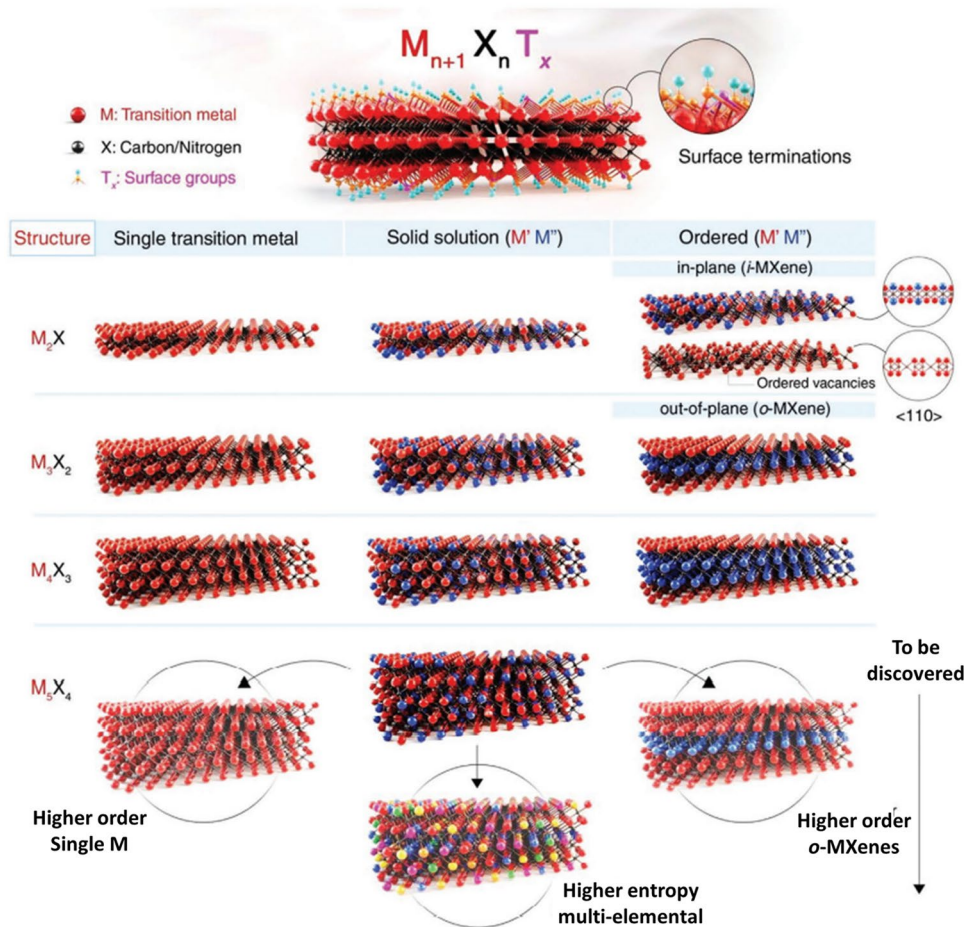


Fig. 1 Schematic display for 2D MXene's structures having a general formula of $M_{n+1}X_nT_x$, (M =an early transition metal, X =carbon and/or nitrogen, and T_x =surface terminations of the outer metal layers, $n=1-4$, examples: Ti_2CT_x , $Ti_3C_2T_x$, $Nb_4C_3T_x$, and $(Mo, V)_5C_4T_x$) [37]. One or more transition metal atoms may occupy the M sites of MXenes to create ordered structures or solid solutions. The ordered double transition metal MXenes can be divided into three types: in-plane ordered structures (i-MXenes), in-plane vacancy structures, and out-of-plane ordered structures (o-MXenes), where either one layer of M'' transition metal or two layers of M'' transition metal are sandwiched between two layers of M' transition metal. Other configurations might be feasible, such as the bottom row of the M_5X_4 structure with one, two, or three layers of M'' sandwiched between layers of M' . Predicted structures like higher-order single M or o-MXenes and high-entropy MXenes that have not been empirically proven are represented by the faded images at the bottom of the schematic. Copyright © 2021 AAAS Publishing

of surface functional groups (T_x) were produced, as represented in Fig. 1 [36]. For certain combinations of transition metals, ordered MXenes are energetically more stable than their solid-solution counterparts. MXenes with monolayer or multilayer morphology are usually synthesized from the $M_{n+1}AX_n$ (MAX) phase precursors by eliminating monoatomic layers of the A element, which is from group 13 or 14 (e.g., Al, Ga, Si, or Ge). However, some of the MXenes are also synthesized from non-MAX phase precursors [37, 38]. The high reactivity of the A element and relatively weak strength of $M-A$ bonds compared to $M-X$ bonds allow the selective etching of A layers from the MAX phase, typically

in aqueous solution using either direct hydrogen fluoride (HF) or in-situ HF (produced through LiF/HCl mixture) [33, 39, 40]. Over the years, apart from HF-based methods, such as using HF/other acids, HF/oxidants, NH_4HF_2 , HCl/fluoride salt as etchants, several new synthesis methods include Lewis acidic molten salts assisted etching, alkali treatment under hydrothermal condition, treatment with organic bases, etching in organic solvents, salt-solution-based acoustic synthesis, electrochemical etching, etc. [41–56].

The type and composition of surface functional groups of MXene depend significantly on etching process, and they are mainly electronegative in nature, enabling to pull electron

density away from the M atoms of MXenes (*i.e.*, shifting the Fermi energy (E_F) of MXenes to a lower energy). That is, the electronic structure and WF of MXenes can be easily tuned by controlling the surface functional groups' compositions [57, 58]. In addition to an E_F shift, surface dipoles induced by surface functional groups play a significant role in tuning the WF of MXenes [59, 60]. Computational calculations such as density functional theory (DFT) through altering the M and X elements and surface functional groups can also predict several other intriguing characteristics of MXenes, such as a wide range tunability of the WF between 1.6 and 8.0 eV, superconductivity, topological insulator behaviors, metal-to-semiconductor transition, and metal-to-insulator transition [59, 61–66]. Particularly, fine-tuning the WF brings a perfect energy offset between the perovskite active layer and the charge transport layer by adjusting the vacuum level and obtaining the optimal energy-level alignment at interfaces in PSCs applications. Optimizing energy offsets is necessary to achieve effective charge separation and/or collection. The various roles of MXenes as components themselves or additives into the components in PSCs, in terms of passivating defects, crystallinity, electrical conductivity, mechanical flexibility, and moisture resistance, are discussed in the following sections.

2.2 PSCs

PSCs have been perceived as the next-generation photovoltaic candidates for commercial applications due to their high PCEs, easy and scalable solution fabrication processes, and low fabrication cost [67, 68]. For high-performance PSCs, the perovskite absorber layer is the most important. The characteristics such as crystallinity, surface coverage,

compactness, uniformity, phase purity, internal trap defect density, grain size distribution, and grain boundaries of the perovskite absorber layers are the pivot players in determining the PCE performance of PSCs [69, 70]. A typical planar (or mesoporous) n-i-p or inverted p-i-n PSC consists of a photoactive absorber layer, an ETL, a HTL, and two (back and front) electrodes. The front electrode is based on a glass/flexible substrate facing simulated solar light. The solar light is incident on an absorber layer, and the electrons excite from the valence band to the conduction band, forming electron–hole pairs [8, 71]. These photogenerated charge carriers are extracted by the respective ETL and HTL and then moved to the electrodes (Fig. 2a). These distinctive features determine the stability and current–voltage hysteresis. Several key factors such as bulk, surface defects and reduced charge extraction/transportation, moisture, humidity, heat, and electric field can impede the solar cell device performance and longevity [72]. These impediments can be controlled via solvent engineering, additive engineering, compositional engineering, interface engineering, device engineering, and encapsulation (Fig. 2b) [8, 73–76]. Furthermore, until now, the highest efficiency devices are Pb-based PSCs. Due to the Pb toxicity, several alternatives such as lead-free PSCs, double-PSCs, and 2D Ruddlesden-Popper (RP) and Dion-Jacobson (DJ) PSCs have been examined as promising candidates in the perovskite photovoltaic arena [77–80]. We have excluded an insightful discussion on the topics mentioned above and suggest you refer to this paper [72]. In this review, we discuss various roles of MXenes as components or parts in PSCs, as depicted in the schematic (Fig. 3). Thus, we categorized the functions of MXenes depending on the positions and the roles of MXenes as additives in the perovskite absorber layer/ETL/HTL/electrodes or as ETL/HTL/electrodes along with as interfacial layers. The

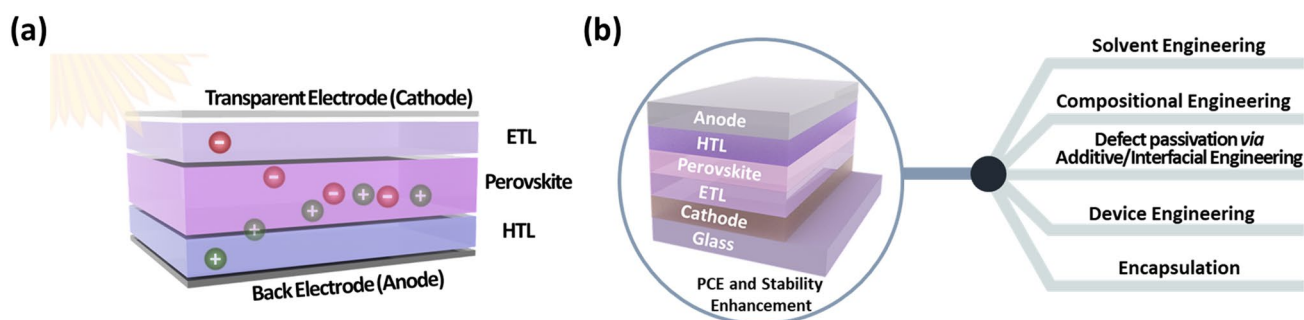


Fig. 2 Schematics showing **a** stacking of different layers in a typical PSC and **b** the prominent ways for improving PCE and stability of PSCs

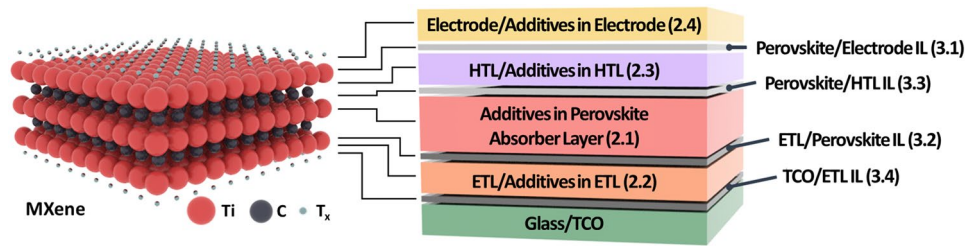


Fig. 3 MXenes in PSCs: Various roles of MXenes as components or parts of the components in regular n-i-p PSCs. The device structure of Glass/TCO/ETL/Perovskite/HTL/Electrode with different ILs, positions of MXenes and numbers in the parenthesis indicate the Section numbers. IL stands for “interfacial layer,” and TCO stands for “transparent conducting oxide”

discussion about their respective pros and cons is presented in the following sections.

2.3 MXenes as Additives in Perovskite Absorber Layers

First up, the PCE performance of a PSC depends on the light-absorbing perovskite film layer that generates the charge carriers (electrons and holes). The charge carriers are separated and collected at the respective electrodes [81]. The quality of the perovskite film is determined by crystal sizes and grain boundaries. Large crystal sizes with fewer grain boundaries are essential for maximum charge transfer and high-performance [82, 83]. In 2018, Guo et al. introduced the $\text{Ti}_3\text{C}_2\text{T}_x$ MXene into a $\text{CH}_3\text{NH}_3\text{PbI}_3$ (MAPbI₃) perovskite absorber layer [31]. This is the first report on an MXene’s application in a PSC. $\text{Ti}_3\text{C}_2\text{T}_x$ MXene slows the crystallization rate and enlarges the size of MAPbI₃ crystals with no pin holes. The O–H···I[−] van der Waals interaction between the methylammonium iodide (MAI) and the additive restricts uniform nucleation on the tin oxide (SnO_2) layer and rather generates lesser nuclei, implying slow crystal growth or retardation of the nucleation process [84]. After annealing, the small crystals grow into large crystals. Perovskite films with $\text{Ti}_3\text{C}_2\text{T}_x$ MXene additives show an improvement in light absorption owing to enhanced scattering of incident light from the large crystals [85, 86]. PSC with a device structure of indium tin oxide (ITO)/ SnO_2 /MAPbI₃:(0.3 wt%) $\text{Ti}_3\text{C}_2\text{T}_x$ /2,2',7,7'-tetrakis(N,N-di-p-methoxyphenyl-amine)9,9'-spirobifluorene (Spiro-OMeTAD)/Au achieved a PCE of 17.4%, which is 12% higher than the PCE (15.6%) of the control device. The device with the optimal amount of additives also showed an increased open-circuit voltage (V_{oc}), current density (J_{sc}), and fill factor (FF). The increase in V_{oc} is ascribed to the passivation of

the perovskites by $\text{Ti}_3\text{C}_2\text{T}_x$, spurring the hole extraction and reduced recombination at the perovskite/HTL interface [87]. A schematic of a PSC with $\text{Ti}_3\text{C}_2\text{T}_x$ additive and J – V curves with 0, 0.01, 0.02, 0.03, 0.5, and 1 wt% of $\text{Ti}_3\text{C}_2\text{T}_x$ MXene additives are shown in Fig. 4a–b. The optimal amount of additive is 0.03 wt%. On further increase in wt%, the additives form aggregates on the surface of the perovskite films, resulting in charge trapping centers. Hence, the device performance degrades with excessive additives. The charge transfer resistance of the perovskite film with additive also reduced from 7000 to 1800 Ω , indicating fast charge transfer, and hence the J_{sc} was increased [31]. All-inorganic CsPbI₃ perovskite has a near-ideal bandgap and thermal stability and is a suitable candidate for the development of perovskite/Si tandem solar cells. But when exposed to moisture, CsPbI₃ experiences a quick phase change. Especially, the preferred p-i-n structure for perovskite/Si tandems shows a large performance difference compared to other perovskite compounds. Heo et al. reported a surface-engineered CsPbI₃ layer with oxidized $\text{Ti}_3\text{C}_2\text{T}_x$ MXene (OMXene) nanoplates to form effective and stable p-i-n-structured CsPbI₃ perovskite solar cells [88]. In addition to improving charge separation at the perovskite-electron transporting layer interface through an improved electric field, OMXene acts as a physical barrier against moisture.

As a result, the p-i-n devices based on CsPbI₃/OMXene dispersion with 10 wt% concentration attained the PCEs of 19.7% for 0.096 cm² cells and 14.6% for 25 cm² in mini-modules. The pristine cell has a PCE of 18.1% with a V_{oc} , J_{sc} , and FF of 1.18 V (1.21 V), 19.05 (19.85) mA cm^{−2}, and 80.3% (81.6%), respectively. Furthermore, the encapsulated minimodule showed good stability, maintaining 85% of the initial efficiency over 1000 h while being exposed to 85 °C at a relative humidity (RH) of 85% and 1-sun light soaking.

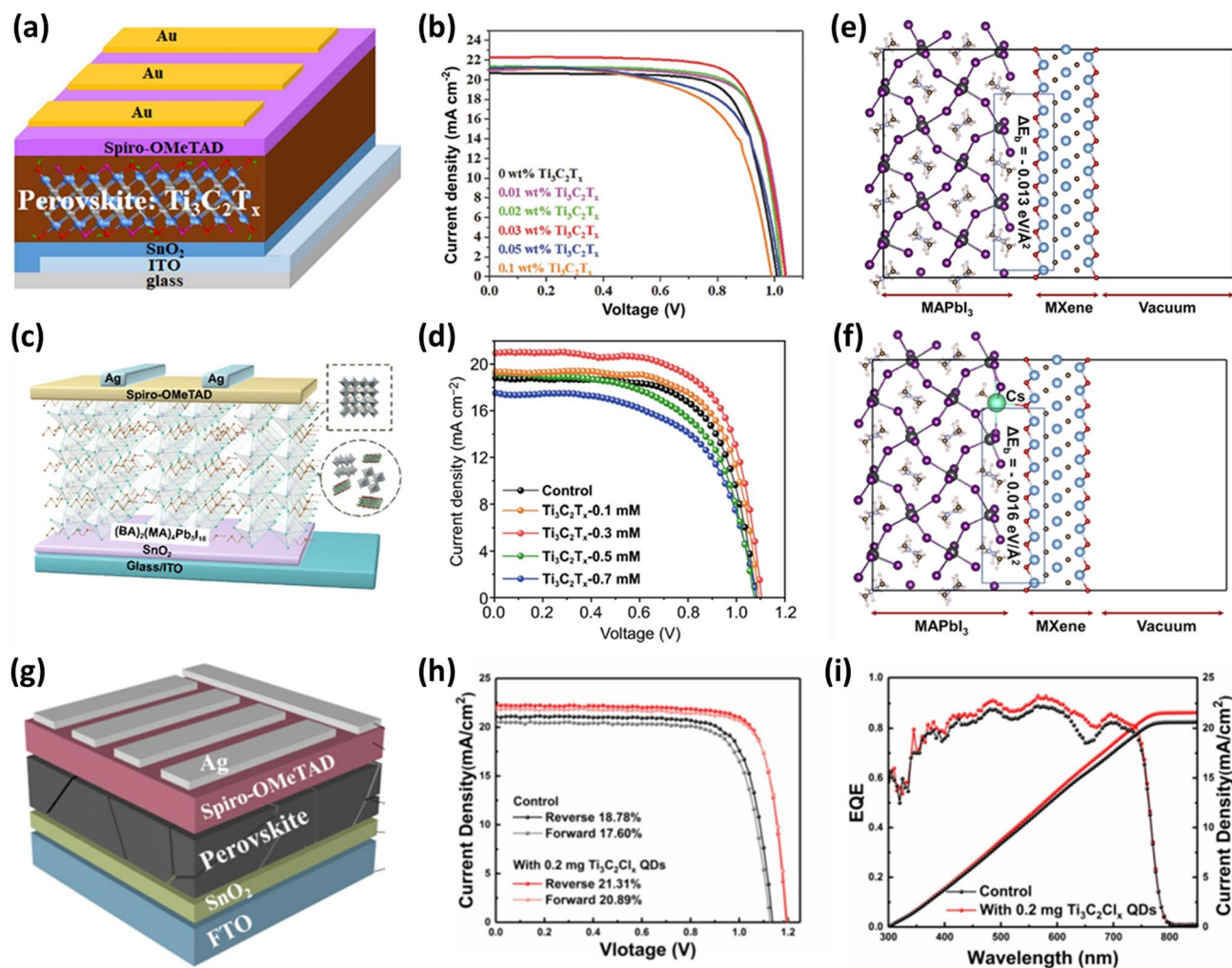


Fig. 4 **a** Schematic of MAPbI₃ planar PSCs with MXenes additives in the absorber layer. **b** *J*–*V* characteristics curves of PSCs with different amounts of Ti₃C₂T_x [31]. Copyright © 2018 WILEY–VCH Verlag GmbH & co. KGaA, Weinheim. **c** Schematic diagram of PSCs with the structure of Glass/ITO/SnO₂/2D perovskite/Spiro-OMeTAD/Ag. **d** *J*–*V* curves of PSCs with different amounts of Ti₃C₂T_x doping [96]. Copyright © 2018 Springer. **e** The atomic structures showing the interface between the MAPbI₃ (100) surface and the Ti₃C₂O₂ MXene without Cs⁺ and **f** with Cs⁺ [97]. Copyright © 2021 Cell Press. **g** Schematic illustration of the device structure. **h** Reverse and forward scans for the pristine and 0.2 mg mL⁻¹ Ti₃C₂Cl_x QDs-treated PSC devices. **i** EQE of the devices (the pristine and 0.2 mg mL⁻¹ Ti₃C₂Cl_x QDs-treated) [98]. Copyright © 2022 Elsevier B.V

Zhou et al. reported an inorganic Cl-terminated Ti₃C₂ (Ti₃C₂Cl_x) MXene to passivate the surface defect states and grain boundaries of CsPbBr₃ film. The addition of Ti₃C₂Cl_x MXene enlarges the crystal sizes. The solvent volatilization produced the Ti₃C₂Cl_x-tailored PbBr₂ film with a high porosity [89]. CsBr can be diffused into these pores to grow the perovskite grain with sizes compared to pre-expanded volume and thus result in a high-quality CsPbBr₃ perovskite film with large and compact grains. The residual stress in the soft perovskite lattice distorts the surface lattices, leading to low device performance. Introducing Ti₃C₂Cl_x MXene

removes the residual stress owing to a strong Pb–Cl binding energy (301 kJ mol⁻¹), paving the way for a high device efficiency [90]. In further work, Saranin et al. introduced MXene doping into the perovskite absorber layer in inverted perovskite solar cells [91]. MXene doping in the absorber layer significantly decreases charge recombination caused by deep trap states. More charges are collected at the perovskite/phenyl-C₆₁-butyric acid methyl ester (PCBM) interface compared to reference devices. The MXene-based tailored cells outperformed the pristine devices and exhibited PCEs of 18.6% and steady power output.

2D RP PSCs have received significant interest owing to their exceptional stability against moisture. The bulky cations in 2D RP perovskites restrict the internal movement of ions and allow the passage of organic ions, thus resulting in the hydrophobic nature of the absorber layer [92, 93]. However, low crystallinity, disordered orientation, and inferior charge transport constrain the PCE of 2D PSCs [94, 95]. Jin et al. explored $\text{Ti}_3\text{C}_2\text{T}_x$ MXene nanosheets as additives in 2D RP $(\text{BA})_2(\text{MA})_4\text{Pb}_5\text{I}_{16}$ perovskite absorber layer to fabricate the perovskite films with excellent electrical conductivity and mobility [96]. A homogeneous and highly crystalline perovskite film with $\text{Ti}_3\text{C}_2\text{T}_x$ MXene nano-dopants was formed. After adding an optimal concentration of 0.3 mM $\text{Ti}_3\text{C}_2\text{T}_x$ nanosheets, the PCE of PSC with a configuration of ITO/ SnO_2 / $(\text{BA})_2(\text{MA})_4\text{Pb}_5\text{I}_{16}$ - $\text{Ti}_3\text{C}_2\text{T}_x$ MXene/Spiro-OMeTAD/Ag increased from 13.7% (without additive) to 15.7%. The $\text{Ti}_3\text{C}_2\text{T}_x$ nanosheets doped-PSC also exhibited an increased J_{sc} of 20.87 mA cm^{-2} , V_{oc} of 1.11 V, and FF of 67.8%. The schematic of the PSC, 2D RP layered structure, and J - V curves of the PSC with different concentrations are shown in Fig. 4c–d. The enhanced crystallinity, orientation, and passivated trap states led to an accelerated charge transfer process in the vertical direction and are responsible for this improved performance. The unencapsulated PSCs with $\text{Ti}_3\text{C}_2\text{T}_x$ nanosheets exhibited excellent stability in ambient settings with an RH of 55% [96].

In 2021, Bati et al. produced $\text{Ti}_3\text{C}_2\text{T}_x$ MXene nanosheets doped with cesium (Cs) and added them to a lead iodide (PbI_2) precursor solution for PSCs via a two-step deposition approach [97]. The theoretical and practical study demonstrated that Cs is crucial for enhancing PCE. The perovskite crystallization with doped $\text{Ti}_3\text{C}_2\text{T}_x$ MXene results in larger crystal grains, long lifetime charge carriers, and reduced charge recombination. The PSCs combined with Cs-doped $\text{Ti}_3\text{C}_2\text{T}_x$ MXene (ITO/ SnO_2 / $\text{FA}_{1-x}\text{MA}_x\text{PbI}_{3-x}\text{Br}_x$:Cs- $\text{Ti}_3\text{C}_2\text{T}_x$ /Spiro-OMeTAD/Au) achieved a high PCE of 21.6% (19.0% for the pristine device) with increased V_{oc} , J_{sc} , and FF. The increased V_{oc} is ascribed to the filling of Cs^+ ions into the surface MA^+ vacancy. Moreover, with the introduction of Cs^+ , the interaction between MXene and perovskite film increases with a binding energy of $-0.016 \text{ eV \AA}^{-2}$. In contrast, without Cs^+ , the binding energy between the perovskite film and MXene is $-0.013 \text{ eV \AA}^{-2}$ (Fig. 4e–f). Additionally, the unencapsulated Cs- $\text{Ti}_3\text{C}_2\text{T}_x$ MXene-doped PSC device exhibited stability by retaining 65% of its initial PCE after 2000 h [97].

High photovoltaic performance and large-scale commercialization of planar PSCs depend on the perovskite layer having a high crystallinity and long-term stability against high humidity. In 2021, Liu et al. used one-step deposition to incorporate $\text{Ti}_3\text{C}_2\text{Cl}_x$ quantum dots (QDs) as additives in the perovskite precursor solution [98]. During the film crystallization process, the strong interaction between the Cl terminations of $\text{Ti}_3\text{C}_2\text{Cl}_x$ QDs and Pb^{2+} ions slowed down the crystallization rate and induced the preferred grain orientation. This resulted in a high-quality perovskite film with high crystallinity, fewer trap-states, and less residual tensile strain. $\text{Ti}_3\text{C}_2\text{Cl}_x$ QDs also quickened charge extraction and benefitted band alignment between the SnO_2 ETL and the perovskite layer due to their top–bottom rising gradient distribution. As a result, the PSC with 0.2 mg mL^{-1} $\text{Ti}_3\text{C}_2\text{Cl}_x$ QDs and a device structure of fluorine-doped tin oxide (FTO)/ SnO_2 /Perovskite + $\text{Ti}_3\text{C}_2\text{Cl}_x$ QDs/Spiro-OMeTAD/Ag) achieved an improved efficiency of 21.3% (18.8%) and V_{oc} of 1.19 V with minimal hysteresis (Fig. 4g–h). The Cl-terminated Ti_3C_2 QDs can also prevent potential deprotonation of protonated organic amine in the perovskite, improving the overall stability. The $\text{Ti}_3\text{C}_2\text{Cl}_x$ QDs (0.2 mg mL^{-1}) device shows a higher integrated J_{sc} of 21.60 mA cm^{-2} than the pristine device (20.64 mA cm^{-2}). The calculated J_{sc} is less than the observed J_{sc} by less than 5% discrepancy (Fig. 4i). Additionally, the unencapsulated device demonstrates exceptional long-term humidity stability by retaining over 84% of its initial PCE after aging for 1000 h at 40% RH in the dark at room temperature [98].

The solution method is the most common route to fabricate the perovskite films. The solution method is categorized into one-step and two-step sequential processes [99–101]. In the simple and facile one-step solution method, it is difficult to achieve uniform and compact perovskite films owing to the anisotropic growth of perovskites [102]. In the two-step process, the PbI_2 layer is formed first, and then the MAI solution is dropped to react, and thus high-quality perovskite films without cracks and pinholes are formed. Crack and pinhole-free perovskite films are pertinent for highly efficient PSCs [103]. However, low reactivity leads to incomplete conversion of PbI_2 , and hence compact films are not formed owing to the presence of residual PbI_2 . As a result, the device performances are degraded [104, 105]. In 2021, to increase the reactivity of PbI_2 by generating porous channels, Zhao et al. added 2D monolayer $\text{Ti}_3\text{C}_2\text{T}_x$ ($\text{T}_x = -\text{O}$, $-\text{OH}$, and $-\text{F}$) MXene nanosheets into the PbI_2

layer [106]. This modification enhanced the subsequent PbI_2 reaction with MAI to transform into MAPbI_3 completely. As a result, the quantity of remaining PbI_2 in the perovskite film was reduced, and the size of the perovskite grain increased (Fig. 5a). Additionally, $\text{Ti}_3\text{C}_2\text{T}_x$ MXene controls the perovskite WF, resulting in a better energy-level alignment that makes carrier extraction and injection easier (Fig. 5b). The functional groups on the surface of $\text{Ti}_3\text{C}_2\text{T}_x$ were found to interact with the poorly coordinated Pb^{2+} in perovskites to passivate defects, having a significant impact on reducing hysteresis and inhibiting nonradiative recombination. Finally, by adding 0.03 wt% of the $\text{Ti}_3\text{C}_2\text{T}_x$ additive, the PSC with a device configuration of FTO/ SnO_2 / MAPbI_3 : $\text{Ti}_3\text{C}_2\text{T}_x$ /Spiro-OMeTAD/Au achieved a PCE of 19.3%, demonstrating an improvement of about 18% over the control device (Fig. 5c) [106].

A promising contender for inorganic double perovskite solar cells without lead is $\text{Cs}_2\text{AgBiBr}_6$ PSC. The reported PCE of $\text{Cs}_2\text{AgBiBr}_6$ is approximately 3%, which limits its photovoltaic capability. Yang et al. used D149 indoline dye to make the TiO_2 ETL more sensitive and $\text{Ti}_3\text{C}_2\text{T}_x$ MXene nanosheets to $\text{Cs}_2\text{AgBiBr}_6$ to improve the crystallization [107]. $\text{Cs}_2\text{AgBiBr}_6$ and D149 indoline dye both have the potential to influence the photocurrent. Furthermore, the DFT was used to calculate the interface properties and electron structure. Fermi level pinning is effectively reduced while the perovskite maintains its semiconductor properties, thanks to weak van der Waals forces at the interfaces of $\text{Cs}_2\text{AgBiBr}_6$ and $\text{Ti}_3\text{C}_2\text{T}_x$. The high WF of $\text{Ti}_3\text{C}_2\text{T}_x$ modifies the Fermi level of the valence band of $\text{Cs}_2\text{AgBiBr}_6$, which results in increased carrier mobility. The device showed enhanced long-term stability and PCEs of 4.5% under 1-sun illumination and 7.2% under 200 lx indoor light

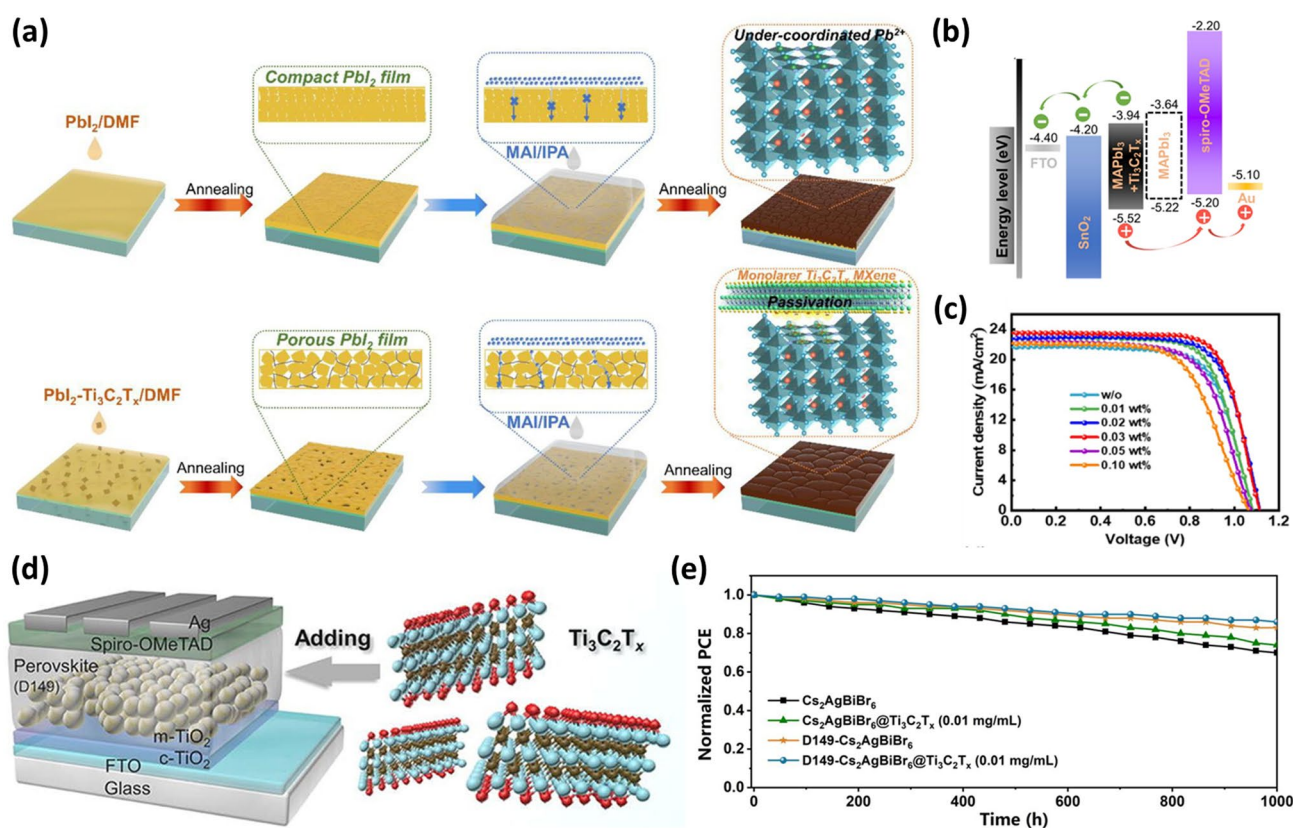


Fig. 5 a Mechanism diagram illustrating the preparation of high-quality two-step-processed perovskite films assisted by $\text{Ti}_3\text{C}_2\text{T}_x$ additive. b Device configuration of the planar PSCs and its energy-level diagram with and without $\text{Ti}_3\text{C}_2\text{T}_x$ doping. c J-V curves of the champion PSCs with different contents of $\text{Ti}_3\text{C}_2\text{T}_x$ [106]. Copyright © 2021 Elsevier B.V. d Schematic of the PSC with $\text{Ti}_3\text{C}_2\text{T}_x$ MXene additive in the perovskite absorber layer. e The stability of the PSC devices with and without D149 sensitized TiO_2 and/or $\text{Ti}_3\text{C}_2\text{T}_x$ doping in ambient air at RH ~ 20% without encapsulation at 25 °C [107]. Copyright © 2022 Elsevier B.V.

illumination. Furthermore, the unencapsulated devices based on $\text{Cs}_2\text{AgBiBr}_6$, $\text{Cs}_2\text{AgBiBr}_6 @ \text{Ti}_3\text{C}_2\text{T}_x$ (0.01 mg mL^{-1}), D149- $\text{Cs}_2\text{AgBiBr}_6$ and D149- $\text{Cs}_2\text{AgBiBr}_6 @ \text{Ti}_3\text{C}_2\text{T}_x$ (0.01 mg mL^{-1}) exhibited long-term stability by retaining 70%, 74%, 83%, and 86% of their initial PCEs after 1000 h of storage at 25 °C in air at about 20% RH (Fig. 5d–e) [107]. Bykkam et al. used a 2D MXene as an additive in MAPbI_3 perovskite at concentrations ranging from 0 to 20 vol% with a 5 vol% increment [108]. With an increase in the vol.% of the 2D MXene, the perovskite peak at $2\theta = 14.2^\circ$ shifts slightly towards the lower angle. The continuous change in peak position reflects the homogeneous distribution of strain during perovskite crystal formation and stresses induced by the 2D MXene additive. However, the perovskite film with 5 vol% additive has fewer defects and improves the photoresponse of the PSC. On further increase in additive concentration, stacking of 2D MXene occurs in the perovskite active layer, hindering the light propagation across the perovskite film and reducing the photogeneration of charge carriers. The best PSC device with 5 vol% 2D MXene additive attained the highest PCE of 13.6%, V_{oc} of $\sim 0.81 \text{ V}$, $J_{sc} \sim 27.6 \text{ mA cm}^{-2}$, and FF of $\sim 61.1\%$. This is higher than the PCE of 11.4% in the PSC without 2D MXene [108].

Din et al. explored the synergistic effect of high-quality NiO_x HTLs deposited by ion beam sputtering on ITO substrates and the $\text{Ti}_3\text{C}_2\text{T}_x$ MXene doping of MAPI perovskite layers to increase the PCE of p-i-n PSCs [109]. The 18 nm-thick NiO_x films are pinhole-free and have large-scale uniform surface morphology. For non-stoichiometric NiO_x , the grazing-incidence X-ray diffraction revealed a 0.75% enlargement of the face-centered cubic lattice. Atomic force microscopy studies revealed that doping increased the size of MAPI polycrystalline grains from 430 ± 80 to $620 \pm 190 \text{ nm}$. The best PSC with 0.15 wt% MXene doping with a device structure of ITO/ NiO_x /MXene-doped MAPI/ PC_{61}BM /BCP/Ag showed a PCE of 16% (14% for the undoped PSC), which is a 14.3% improvement. However, the band gap of the MXene-doped MAPI layer was found to have a one order of magnitude higher density of defect states ($\sim 10^{19} \text{ cm}^{-3} \text{ eV}^{-1}$ for the MXene-doped MAPI and $\sim 10^{18} \text{ cm}^{-3} \text{ eV}^{-1}$ for the undoped-MAPI), which lowers the favorable effect of the total area of bigger MAPI grain boundaries, reducing the J_{sc} of the MXene-doped devices. The WF drops from -5.26 to -5.32 eV with MXene doping, which raises the V_{oc} and FF, and thus is credited with improving the PCEs of PSCs. Such different results are attributed to large and partly delaminated

multilayer MXene sheets and an increased density of states in the bandgap [109].

To improve the PCE of PSCs using a one-step coating method, Li et al. added 2D $\text{Ti}_3\text{C}_2\text{T}_x$ and V_2CT_x MXene to a PbI_2 precursor solution to fabricate perovskite films [110]. The addition of $\text{Ti}_3\text{C}_2\text{T}_x$ and V_2CT_x additives boosted the hydrophobicity of the perovskite film, showing water contact angles of 85.4° and 69.8° , respectively, as compared to 52.9° for the pristine film. Furthermore, the additives also enhanced the shape and grain size of the perovskite films. The PCEs of PSCs with $\text{Ti}_3\text{C}_2\text{T}_x$ and V_2CT_x additives attained 17.6% and 17.2%, respectively, compared to the device without additives (15.0%). Moreover, a distinct morphology with uniform grain size and organized layered crystal particles can be observed for perovskite films employing the V_2CT_x additive, indicating that the V_2CT_x additive controls the formation of perovskite crystal films. Due to the improved crystallinity and perovskite film quality, the V_2CT_x additive integrated devices can preserve 68.3% of the initial PCE after 15 days, which is greater than the devices without additives by 9.7% and with $\text{Ti}_3\text{C}_2\text{T}_x$ as additive by 47.2%. Thus, V_2CT_x in photovoltaics offers a practical way to enhance the performance of PSCs [110].

2.4 MXenes as ETLs or Additives in ETL

2.4.1 MXenes as ETLs

Yang et al. used $\text{Ti}_3\text{C}_2\text{T}_x$ MXene nanosheets as a novel kind of ETL in planar structured PSCs that have undergone low-temperature processing [111]. The metallic $\text{Ti}_3\text{C}_2\text{T}_x$ can be improved as an ETL by applying a UV-ozone treatment that boosts the surface Ti–O bonds without affecting the bulk properties, such as high electron mobility. The schematic and cross-sectional SEM image of the PSC device with a configuration of ITO/ $\text{Ti}_3\text{C}_2\text{T}_x$ /MAPbI₃/Spiro-OMeTAD/Ag are displayed in Fig. 6a–b, respectively. The thickness of the $\text{Ti}_3\text{C}_2\text{T}_x$ layer is found to be $18 \pm 3 \text{ nm}$. Figure 6c shows a schematic illustration of the energy-level diagram for each component of the PSC device. The shift in WF of $\text{Ti}_3\text{C}_2\text{T}_x$ from -5.52 to -5.62 eV after UV-ozone treatment enables faster electron transport. The PCE of PSC increased to 5% in the case of $\text{Ti}_3\text{C}_2\text{T}_x$ ETL without UV-ozone treatment and to 17.2% with a $\text{Ti}_3\text{C}_2\text{T}_x$ ETL film after 30 min of UV-ozone treatment because of an improved electron transfer.

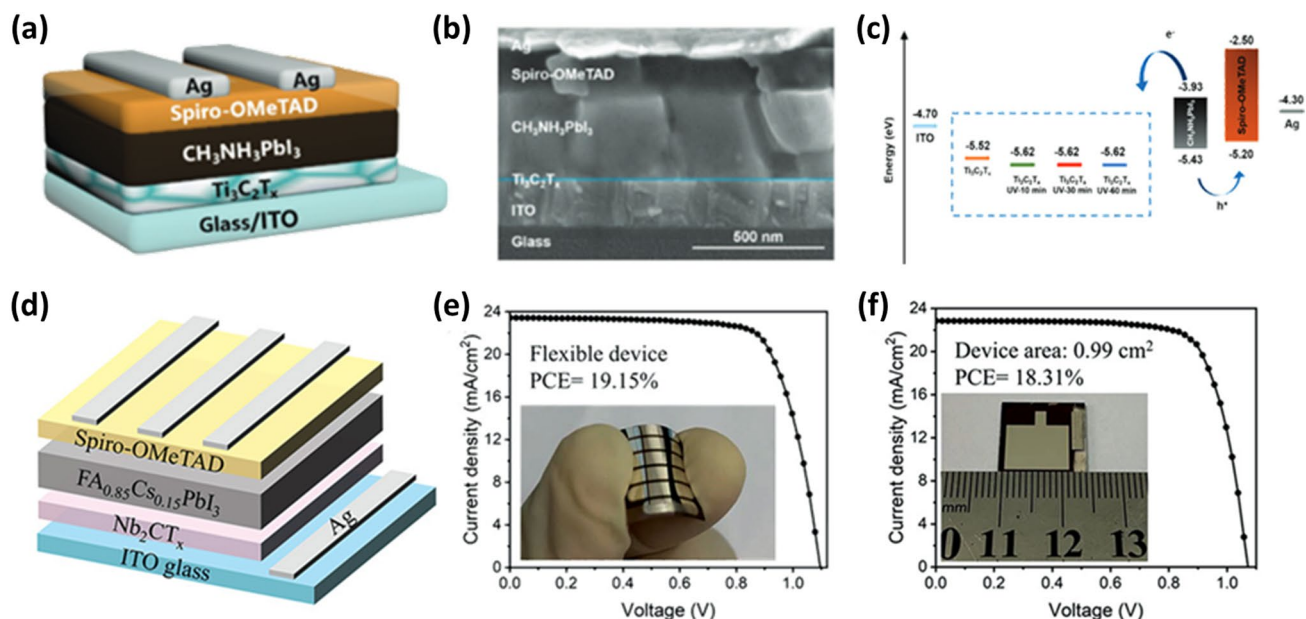


Fig. 6 **a** Device architecture of ITO/ETL/MAPbI₃/Spiro-OMeTAD/Ag based on Ti₃C₂T_x with/without UV-ozone treatment as ETL. **b** Cross-sectional SEM image of the PSC device. **c** Schematic energy-level diagram of each layer [111]. Copyright © 2019 WILEY–VCH Verlag GmbH & Co. KGaA, Weinheim. **d** Schematic device structure of ITO/Nb₂CT_x/FA_{0.85}Cs_{0.15}PbI₃/Spiro-OMeTAD/Ag, and. **e** *J*–*V* curves of the flexible and **f** the large area devices [112]. Copyright © 2022 Wiley–VCH GmbH

The UV-ozone treated Ti₃C₂T_x ETL suppressed recombination at the ETL/perovskite interface [111].

Zhang et al. fabricated 2D Nb₂CT_x MXene nanosheets ETL and incorporated them into the perovskite absorber layer [112]. The WF of Nb₂CT_x was tuned from 4.65 to 4.32 eV by replacing its –F groups with –NH₂ groups through hydrazine (N₂H₄) treatment to match the conduction band minimum of the perovskite layer. Additionally, incorporating N₂H₄-treated (T-Nb₂CT_x) MXene nanosheets with abundant NH₂ groups slows the crystallization rate of the perovskite precursor by forming a hydrogen bond with iodine ions, which encourages the creation of high-quality and oriented perovskite films. As a result, the PSC with a device configuration of ITO/Nb₂CT_x/FA_{0.85}Cs_{0.15}PbI₃/Spiro-OMeTAD/Ag demonstrated a maximum PCE of 21.79% with T-Nb₂CT_x MXene ETLs and T-Nb₂CT_x MXene nanosheet additive. The highest PCE values of 19.2% and 18.3% were realized for the corresponding flexible and large-area devices (Fig. 6d–f). After 1500 h of storage, the unencapsulated devices still retain 93% of the original PCEs. This research illustrates the wide range of potential applications for 2D Nb₂CT_x MXene in photoelectric devices [112].

Despite many benefits of 2D Ti₃C₂T_x MXene, including high transparency, high conductivity, variable WF, and solution processability, the performance of the MXene-based PSC is still subpar to that of the conventional TiO₂- or SnO₂-based equivalent. The MXene/perovskite interface has some critical problems that need to be resolved. Wang et al. adopted a room-temperature solution technique followed by oxygen plasma treatment to use Ti₃C₂T_x MXene as ETL in PSCs [113]. Oxygen plasma treatment was demonstrated to form abundant Ti–O bonds randomly distributed on MXene and disrupt portions of Ti–C bonds. In addition to reduced trap states and better electron transport along the interface, the surface change made MXene WFs variable. In addition, contact angle and topography measurements were used to extensively analyze the surface tension of MXene and the related perovskite morphology. The device stability was improved, thanks to the PbO contacts between perovskite and MXene. The champion device attained a high PCE of 18.9% with a steady state output *J*_{sc} of 21.5 mA cm^{–2}. The unencapsulated PSC with plasma-treated ETL demonstrated long-term stability by retaining 90% of its initial PCE after 750 h of storage in ambient air at 25 °C and RH of ~50% [113].

MXenes are appealing for use in PSCs due to their distinct features that result from surface functional groups and oxidation. Yang et al. oxidized $\text{Ti}_3\text{C}_2\text{T}_x$ hydrocolloid to adjust its characteristics for an ETL in low-temperature processed PSCs [114]. The energy levels were calculated using the Vienna ab initio simulation package code, which is based on DFT. $\text{Ti}_3\text{C}_2\text{T}_x$ can be oxidized to produce Ti–O bonds and significantly minimize the macroscopic defects in a spin-coated film. However, after substantial oxidation, the material changes from metallic to semiconductor. In the case of a hybrid of oxidized and pristine $\text{Ti}_3\text{C}_2\text{T}_x$, better matching of energy levels between perovskite and ETL layer results in a champion PCE of 18.3%. The improved electron mobility in the ETL, which encourages electron transport and lowers electron–hole recombination, is responsible for improving the PCE. This work illustrates the significant potential of MXene-derived materials in low-temperature processed PSCs [114].

2.4.2 MXenes as Additives in ETLs

SnO_2 ETLs are extensively used in planar and flexible devices due to a lower annealing temperature (below 185 °C), and better electrical and optical properties [115, 116]. These ETLs have disadvantages of de-wetting property, low transmittance, and conductivity. On the other hand, TiO_2 ETL is also commonly used for high PSC devices and requires a high annealing temperature of 450–500 °C [117]. Furthermore, the PSC with the SnO_2 nanoparticle-modified TiO_2 ($\text{SnO}_2@ \text{TiO}_2$) composite ETL processed at low temperature shows a high PCE of 21.3%. However, the amorphous nature of TiO_2 at low temperatures limits the PCE of the devices [118, 119]. In 2020, Huang et al. used a multi-dimensional conductive network (MDCN) heterojunction structure made of TiO_2 , SnO_2 , and $\text{Ti}_3\text{C}_2\text{T}_x$ MXene as the electron transport layer to fabricate stable and efficient planar PSCs [120]. Based on an oxygen vacancy scrambling effect, the zero-dimensional anatase TiO_2 quantum dots are in-situ rooted on three-dimensional SnO_2 nanoparticles, forming nanoscale $\text{TiO}_2/\text{SnO}_2$ heterojunctions, and are surrounded by 2D conductive $\text{Ti}_3\text{C}_2\text{T}_x$ sheets. The fabrication process for the $(\text{FAPbI}_3)_{0.97}(\text{MAPbBr}_3)_{0.03}$ perovskite thin film with the MDCN ETL is carried out using a controlled low-temperature annealing technique first in an environment of air and later in N_2 (Fig. 7a). The optical quality, the crystallinity of the perovskite layer, and internal interfaces are all

improved by the optimal MXene concentration of 0.02 wt% contributing more carriers with effective and speedy transfer in the device. The resulting PSCs with MDCN ETL-air and N_2 attained a champion PCE of 19.1%, compared to the PCE of 16.8% for the pristine device with SnO_2 ETL. Furthermore, the device with MDCN ETL retained nearly 85% of its initial performance for over 45 days in air with a humidity of 30–40%; in contrast, the pristine (control) device only retained about 75% of its initial performance [120].

Defect-free polycrystalline perovskite films are highly desirable for fabricating an effective and stable PSC. However, the use of molecular materials in conventional defect reduction methods suffers from their complicated procedures, poor durability, and limited effects. Zheng et al. used a hybrid film made of SnO_2 nanoparticles and $\text{Ti}_3\text{C}_2\text{T}_x$ MXene nanoflakes as ETL in a planar regular-structure PSC [121]. The $\text{SnO}_2/\text{MXene}$ colloidal suspension is spun onto ITO substrates to form the ETL, and then the perovskite layer ($\text{MA}_{0.15}\text{FA}_{0.85}\text{PbI}_x\text{Br}_{3-x}$) is spin-coated on the previously coated ETL via a typical two-step deposition technique (Fig. 7b). The film properties of the top perovskite layers, such as compactness, crystal size, surface roughness, crystallinity, optical absorption, defect density, and so on, are changeable by varying the $\text{Ti}_3\text{C}_2\text{T}_x/\text{SnO}_2$ ratios (0–2.2 wt%) in ETLs. Compared to a pristine device with SnO_2 ETL, the defect density in perovskite films with an optimized 1.4 wt% hybrid ETL is significantly reduced from 5.65×10^{15} to $2.25 \times 10^{15} \text{ cm}^{-3}$. However, the electrical conductivity of the hybrid ETL is decreased, most likely because of the geometric configuration of the added MXene. As a result, the PCE of PSCs with 1.5 wt% $\text{Ti}_3\text{C}_2\text{T}_x/\text{SnO}_2$ ratio is boosted significantly from 16.28 to 20.35%, along with J_{sc} and FF increasing from 20.65 and 0.71 to 23.65 mA cm^{-2} and 0.76 (Fig. 7c). However, V_{oc} (1.111 to 1.113 V) remained almost stable. Furthermore, the environmental stability of the unencapsulated devices is dramatically enhanced by retaining 74% of their initial PCE after 768 h of storage under an air environment at 25 °C with an RH of 30% [121].

To address the issue of the instability of the APbX_3 structure and lead toxicity, the inorganic $\text{Cs}_2\text{AgBiBr}_6$ double perovskite structure is a viable development route for PSCs. However, the optoelectronic application is severely constrained by the low J_{sc} and PCE owing to the low crystallization of $\text{Cs}_2\text{AgBiBr}_6$. Li et al. used a straightforward method to dope single-layered MXene nanosheets into titania ($\text{Ti}_3\text{C}_2\text{T}_x@ \text{TiO}_2$) to serve as a versatile ETL for stable

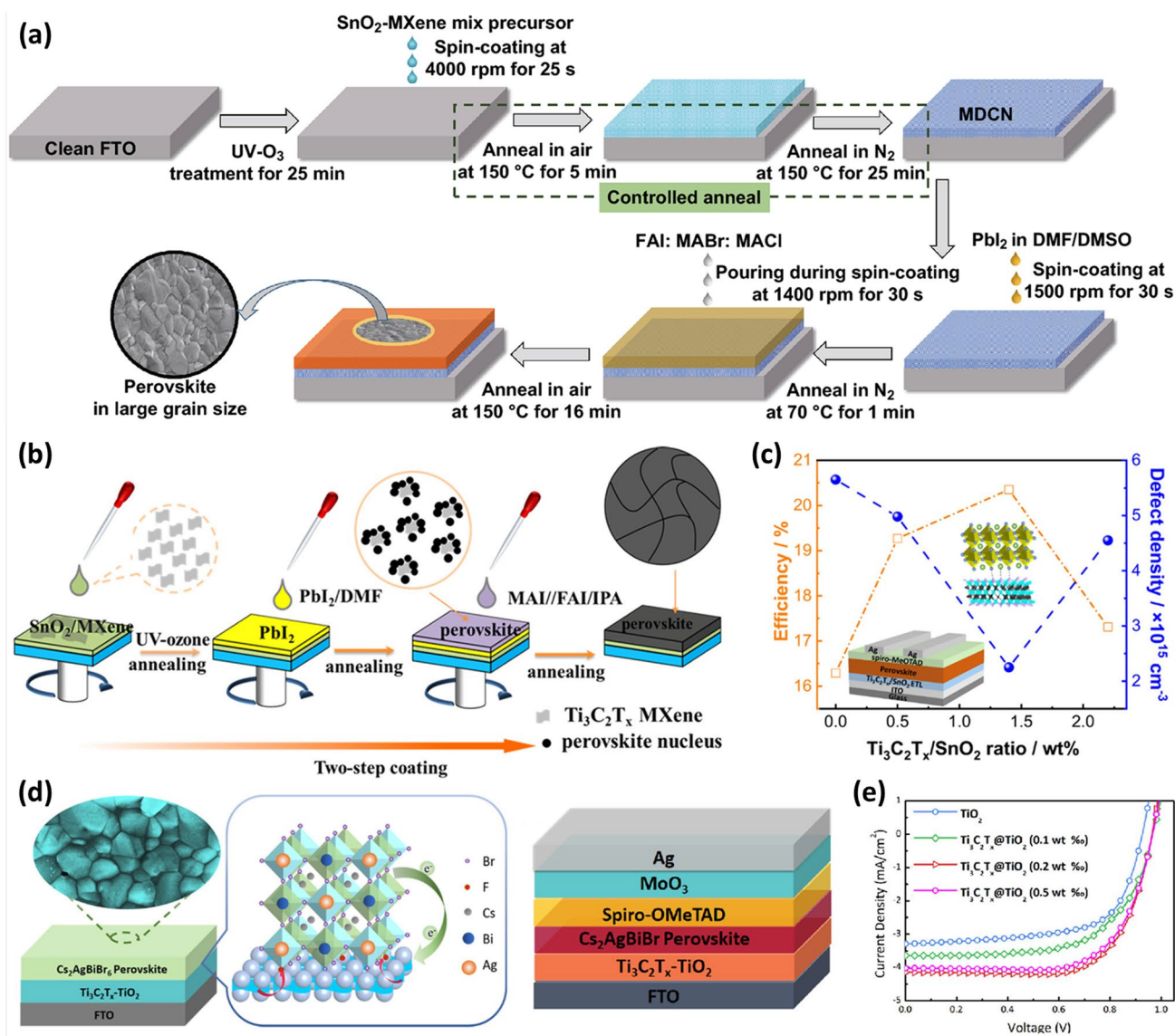


Fig. 7 **a** Fabrication process of perovskite layer on MDCN ETL [120]. – Copyright © 2020 Springer. **b** Schematic illustration of the preparation processes of the ETL and the perovskite film. **c** Schematic diagram of PSC and MXene with Perovskite, efficiency, and defect density values with respect to Ti₃C₂T_x/SnO₂ wt% [121]. Copyright © 2021 American Chemical Society. **d** Schematic of Cs₂AgBiBr₆/Ti₃C₂T_x@TiO₂ structure with scanning electron microscope (SEM) image illustrating film quality. **e** *J*-*V* curves of planar Cs₂AgBiBr₆ PSCs based on TiO₂ and different weight percentage of Ti₃C₂T_x@TiO₂ [122]. Copyright © 2021 American Chemical Society

and effective Cs₂AgBiBr₆ double PSCs [122]. In addition to considerably increasing TiO₂ electrical conductivity and electron extraction rate, single-layered MXene nanosheets also alter the surface wettability of the electron transport layer and promote the crystallization of Cs₂AgBiBr₆ double perovskite in solar cell devices. The Cs₂AgBiBr₆ double perovskite films based on both TiO₂ and Ti₃C₂T_x@TiO₂ ETLs have a similar grain size of 200–500 nm (Fig. 7d–e). The

TiO₂-based Cs₂AgBiBr₆ film contains large voids, which are pathways for current leakage. In contrast, the Ti₃C₂T_x@TiO₂-based Cs₂AgBiBr₆ film is smooth and void-free. As a result, compared to a device based on TiO₂ ETL, the PCE increased by more than 40% to 2.8%, and the hysteresis was significantly reduced. Additionally, the Ti₃C₂T_x@TiO₂ device demonstrated long-term operational stability. The Ti₃C₂T_x@TiO₂ device retained 93% of its initial PCE even

after 15 days of storage in ambient air [122]. Saranin et al. doped MXene in both MAPbI₃ perovskite absorber layer and PCBM layers in an inverted PSC (glass-ITO/NiO/Perovskite + MXenes/PCBM + MXenes/bathocuproine (BCP)/Ag). The MXene doping improves the band alignment at the perovskite/charge transport layer owing to the WF shift, which facilitates charge extraction at the electrodes. Hence the inverted PSC attained a PCE of 19.20% [91].

To reduce recombination losses and enhance the PCE of PSCs, defect passivation and customizing the perovskite charge transport layer interfaces are crucial. Chava et al. tailored the electrical characteristics of the ETL and the ETL/perovskite interface in inverted (pin) PSCs using Ti₃C₂T_x MXene [123]. A [6, 6]-phenyl-C₆₁-butyric acid methyl ester (MPC₆₁BM)-based ETL with MXene doping has improved electrical conductivity and band alignment at the ETL/perovskite interface. The n-doping of PC₆₁BM was confirmed by a red shift of the A_g (2) peak in the Raman spectrum, and a localized upshift of the Fermi level measured using scanning Kelvin probe force microscopy (SKPFM). As a result, PSC devices using M-PC₆₁BM as the ETL attained a higher PCE of over 18% than control devices using PC₆₁BM as the ETL, with a PCE of 15.55%. Furthermore, the PSC with MXene as an interfacial layer between the perovskite and ETL with a structure of ITO/NiO_x/MXene/MAPbI₃/PC₆₁BM/BCP/Ag attained a maximum PCE of 15.99% with a maximum V_{oc} , J_{sc} , and FF of 1.05 V, 20.74 mA cm⁻², and 74%, respectively. In comparison, the PSC with a standalone Ti₃C₂T_x MXene ETL showed a maximum of 2.06%, with a maximum V_{oc} , J_{sc} , and FF of 0.72 V, 5.57 mA cm⁻², and 50%, respectively. The addition of MXene to PSCs has demonstrated diverse effects, including improvement in carrier transport, passivation and trap state reduction, and better interfacial energy alignment [123].

Yang et al. utilized SnO₂-Ti₃C₂ MXene (Ti₃C₂ MXene + SnO₂) nanocomposites with varying Ti₃C₂ contents (0, 0.5, 1.0, 2.0, and 2.5 wt%) as ETLs and applied in planar-structured PSCs with an architecture of ITO/SnO₂ + Ti₃C₂T_x/MAPbI₃/Spiro-OMeTAD/Ag (Fig. 8a) [124]. The corresponding cross-sectional SEM image of the PSC and energy-level diagram of each component are shown in Fig. 8b–c. The lowest occupied molecular orbital reduces from -4.39 eV for pure SnO₂ ETL to -4.63 eV for SnO₂ + Ti₃C₂T_x ETL, facilitating fast electron transfer. The PCE of the device fabricated with pure Ti₃C₂ as the ETL increases from 17.2 to 18.3% when SnO₂ and 1.0 wt%

Ti₃C₂ are combined. The metallic Ti₃C₂ MXene nanosheets demonstrated superior charge transfer pathways, improving electron extraction and mobility while lowering electron transfer resistance at the ETL/perovskite interface, resulting in higher photocurrents [124].

ETL materials with good optoelectrical properties and energy levels comparable to the perovskite layer are essential to meet the demand for commercialization. Niu et al. introduced Nb₂C MXenes as an additive to SnO₂ ETL for the first time, which caused the SnO₂ grains to develop clearly [125]. The incorporation of Nb₂C MXenes leads to an increase in lattice spacing of (101) and (110) planes corresponding to SnO₂ ETL from 0.32 to 0.33 nm and 0.240 to 0.253 nm, respectively. Further, the roughness and average grain size increased from 3.76 and 179 nm for SnO₂ ETL to 11.1 and 256 nm for the SnO₂-Nb₂C ETL, respectively. In addition, the Nb₂C inclusion in SnO₂ also reduces surface energy between the perovskite and the ETL, improving the surface wettability so that the perovskite solution can spread smoothly on the ETL. The light reflection also reduced, indicating improved light absorption and an improved fill factor. The electron mobility for the SnO₂ ETLs increased from 2.3 × 10⁻⁵ to 1.39 × 10⁻⁴ cm² V⁻¹ s⁻¹ for the SnO₂-Nb₂C ETLs, indicating faster electron transfer from perovskites to ETLs. Hence, the PSCs based on the architecture of ITO/SnO₂-Nb₂C/Perovskite/Spiro-OMeTAD/Ag exhibited the best PCE of 22.86% (18.96% for the control device) with improved V_{oc} , J_{sc} and FF. The PSCs with the modified ETL maintain 98% of the original efficiencies after 40 days at 25 °C under a humidity of 40–60% [125].

Yin et al. utilized fluoroalkylsilane and dodecyltrimethoxysilane functionalized MXene nanosheets as dopants into the SnO₂ ETL to fabricate PSC devices with modified ETL layers, respectively, denoted as SnO₂-MF and SnO₂-MH [126]. To fabricate high-performance devices, it is necessary to have an ETL with improved energy alignment and improved charge transfer, which will aid in the efficient extraction and transport of photogenerated carriers. The SnO₂-MH ETL has improved band alignment, as evidenced by DFT calculations and ultraviolet photoelectron spectra measurements. In the meantime, functionalized MXene nanosheets exhibit strong electrical conductivity and mobility and may quickly and effectively establish a zero Schottky barrier heterojunction with SnO₂. Finally, the appropriate surface energy attained by functionalized MXene additives can increase the grain size of the perovskite thin film. The schematic of PSC and

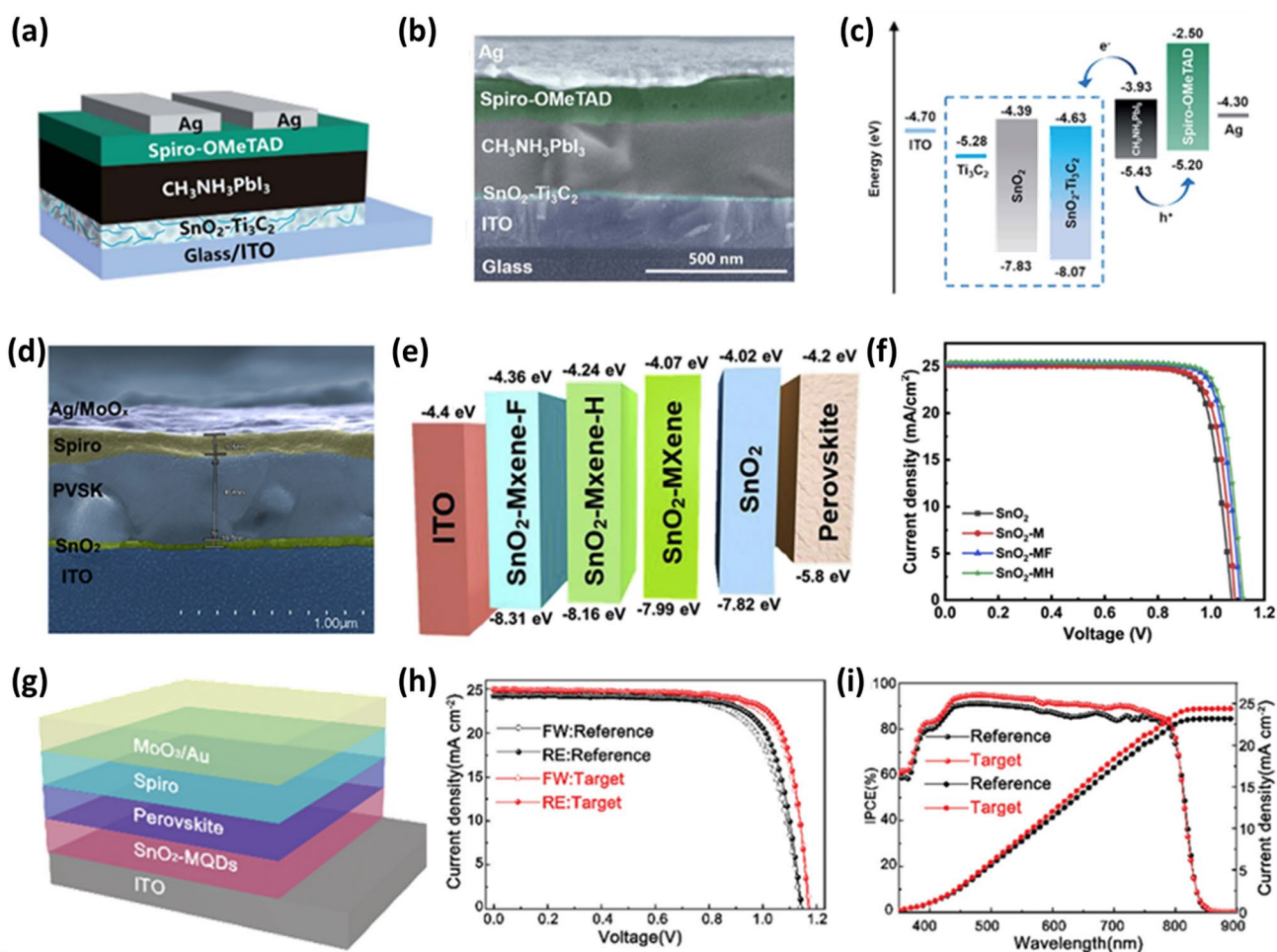


Fig. 8 **a** Device architecture of ITO/ETL/MAPbI₃/Spiro-OMeTAD/Ag based on representative SnO₂-Ti₃C₂ as the ETL. **b** Cross-sectional SEM image of the PSC device. **c** Schematic energy-level diagram of each layer [124]. – Copyright © The Royal Society of Chemistry. **d** Cross-sectional image with ITO/SnO₂-MH/Perovskite/Spiro/Ag structure. **e** Energy-level diagram of the ITO/ETL/AL structure based on SnO₂, SnO₂-M, SnO₂-MF, and SnO₂-MH as the ETLs. **f** *J*-*V* curves of the champion devices based on each ETL under reverse scans for the FAPbI₃ system [126]. Copyright © 2022 Cell Press. **g** Schematic of the planar heterojunction structure used for the SnO₂-based PSCs. **h** *J*-*V* curves of one of the best SnO₂-based and MQDs-SnO₂-based PSCs devices under both forward and reverse scans. **i** IPCE curves and integrated current density of these two devices [127]. Copyright © 2021 The Royal Society of Chemistry

the energy-level diagram of different SnO₂, ITO and perovskite layers are sketched in Fig. 8d–e. The devices based on the SnO₂-MH ETL with the device architecture of ITO/SnO₂-MH/FAPbI₃/Spiro/MoO_x/Ag significantly enhanced their PCE from 21% (with no additive) to 23.66%. The champion device exhibited a maximum PCE of 24.1% with a *J*_{sc} of 25.49 mA cm⁻², a *V*_{oc} of 1.121 V, and a FF of 84.4% (Fig. 8f). The PSCs also demonstrated better operational stability and moisture resistance [126].

Yang et al. fabricated a modified SnO₂ bottom layer to produce highly crystalline perovskite films to improve the photovoltaic performance of PSCs [127]. To produce highly

crystalline and durable perovskite films, perovskite crystallization mechanisms must be modulated. Ti₃C₂T_x quantum dots (MQDs) were introduced into SnO₂ ETL to investigate the crystallization kinetics of the perovskite. It was discovered that perovskite nucleation from the precursor solution could be induced quickly by Ti₃C₂T_x MQDs-modified SnO₂ (MQDs-SnO₂) ETL, resulting in the formation of an intermediate perovskite phase after anti-solvent treatment. As a result, the perovskite film crystal quality and phase stability are significantly improved. A steady-state PCE of 23.3%, with a *J*_{sc} of 24.96 mA cm⁻², a *V*_{oc} of 1.172 V, and an FF of 0.798 were attained for PSCs with a device structure of ITO/

SnO₂-MQD/Perovskite/Spiro/MoO_x/Au (Fig. 8g–h) by taking advantage of the excellent charge extraction capabilities of the MQDs-SnO₂ layer. The PSC with MQDs-SnO₂ ETL has higher incident photon-to-electron conversion efficiency (IPCE) over the entire visible region compared to the pristine device. The integrated J_{sc} value of 24.39 mA cm⁻² is very close to the observed J_{sc} value of 24.96 mA cm⁻² as observed by a solar simulator (Fig. 8i). The fabricated PSC also demonstrated exceptional stability against humidity and light soaking [127].

2.5 MXenes as HTLs or Additives in HTLs

2.5.1 MXenes as HTLs

In PSCs, the HTL plays a vital role in controlling the crystallization of a perovskite film and the hole transfer efficiency at the perovskite/HTL interface. Although many successes in PSC by organic hole transport materials (HTMs) such as N,N'-bis(3-methylphenyl)-N,N'-bis(phenyl) benzidine, poly(trimethylene terephthalate-co-trimethylene isophthalate)-Terephthalic acid (PTTI-TPA), triphenylamine-based HTM incorporating pyridine core (coded as H-Pyr) and pyridine-based polymer semiconductor (PPY2), the organic HTLs fail to scale up the mass-production due to complexity of synthesis, purification and the manufacturing cost associated with the synthesis procedures [128–130]. In contrast, the common inorganic HTM NiO_x requires an annealing temperature above 200 °C and is unsuitable for flexible devices. Hence, low-cost and low-temperature processed HTMs with excellent electrical properties are necessary. Nb₂CT_x MXene is a promising HTM due to good conductivity and an adjustable WF [131, 132]. Furthermore, the Nb₂CT_x MXene has three atomic layers compared to the five atomic layers of the Ti₃C₂T_x MXene (excluding atomic layers of surface functional groups). Hence Nb₂CT_x has a larger specific area, and consequently, the contact area with the perovskite layer is also larger. This promptly increased the charge transfer in PSCs. The charge transfer depends upon the WF of Nb₂CT_x MXene. However, the WF can be controlled depending on the type and quantity of the surface-terminated functional groups [59, 133]. As observed from First-principles calculations, the WF of the pristine Nb₂CT_x nanosheets with -O, -OH, and -F surface functional groups is approximately 4.7 eV, which is not enough to transport

holes across the Nb₂CT_x/MAPbI₃ interface. Commonly, O-terminated Nb₂CT_x shows a higher WF compared to the F- and OH-terminated counterparts. This WF difference arises due to the different surface dipole moments and a difference in charge transfer between the terminated functional groups and Nb atoms [59, 61]. In 2021, Zhang et al. synthesized the highly photoelectric Nb₂CT_x MXene by oxygen plasma treatment and used it as the HTL in inverted PSCs [134]. The oxygen plasma-treated Nb₂CT_x MXene nanosheets showed enhanced conductivity and high transmittance. The oxygen plasma treatment modified the WF of Nb₂CT_x from 4.68 eV (pristine) to 5.04 eV by enhancing the O functional groups on the Nb₂CT_x surface. In other words, the high electronegative O atoms pull electrons from Nb atoms, thus reducing the Fermi level of Nb₂CT_x. At the same time, the O functional groups induce a dipole moment with O atoms facing toward Nb atoms, uplifting the vacuum level. The combined effect of the downshifted Fermi level and uplifted vacuum level increased the WF of the Nb₂CT_x. This high WF reduced energy offset/loss at the interface between the HTL/perovskite absorber layer and eased the hole transfer from the perovskite layer to HTL, leading to suppressed charge recombination and high J_{sc} . Furthermore, the photoluminescence (PL) spectra from the perovskite film with the oxygen plasma treated Nb₂CT_x (Nb₂CT_x/MAPbI₃) indicated the most significant PL intensity quenching, suggesting an improved hole extraction ability of Nb₂CT_x. From time-resolved PL spectra, the average PL lifetime is found to decrease from 16.51 ns (glass/MAPbI₃) to 2.26 ns (ITO/MAPbI₃), 1.64 ns (ITO/Nb₂CT_x/MAPbI₃), and 0.72 ns (ITO/treated Nb₂CT_x/MAPbI₃), which further confirms the excellent hole transportability of Nb₂CT_x. The PSC with the plasma-treated Nb₂CT_x MXene HTL with a device structure of ITO/Nb₂CT_x/MAPbI₃/PCBM/Ag exhibits a higher PCE of 20.74% with increased V_{oc} and J_{sc} than those with the pristine Nb₂CT_x (18.1%) and without Nb₂CT_x MXene HTLs (15.5%). The higher external quantum efficiency (EQE) values indicate the enhanced J_{sc} , suggesting more efficient charge separation and collection efficiency. The PSCs with oxygen plasma-treated Nb₂CT_x HTLs attain the highest EQE and integrated J_{sc} (22.75 mA cm⁻²), close to the J_{sc} values obtained from the J - V measurements (Fig. 9c). Additionally, the flexible and large area (0.99 cm²) PSCs with oxygen plasma treated Nb₂CT_x HTLs exhibit the highest PCE of 17.3% and 17.9%, respectively. Moreover, the Nb₂CT_x

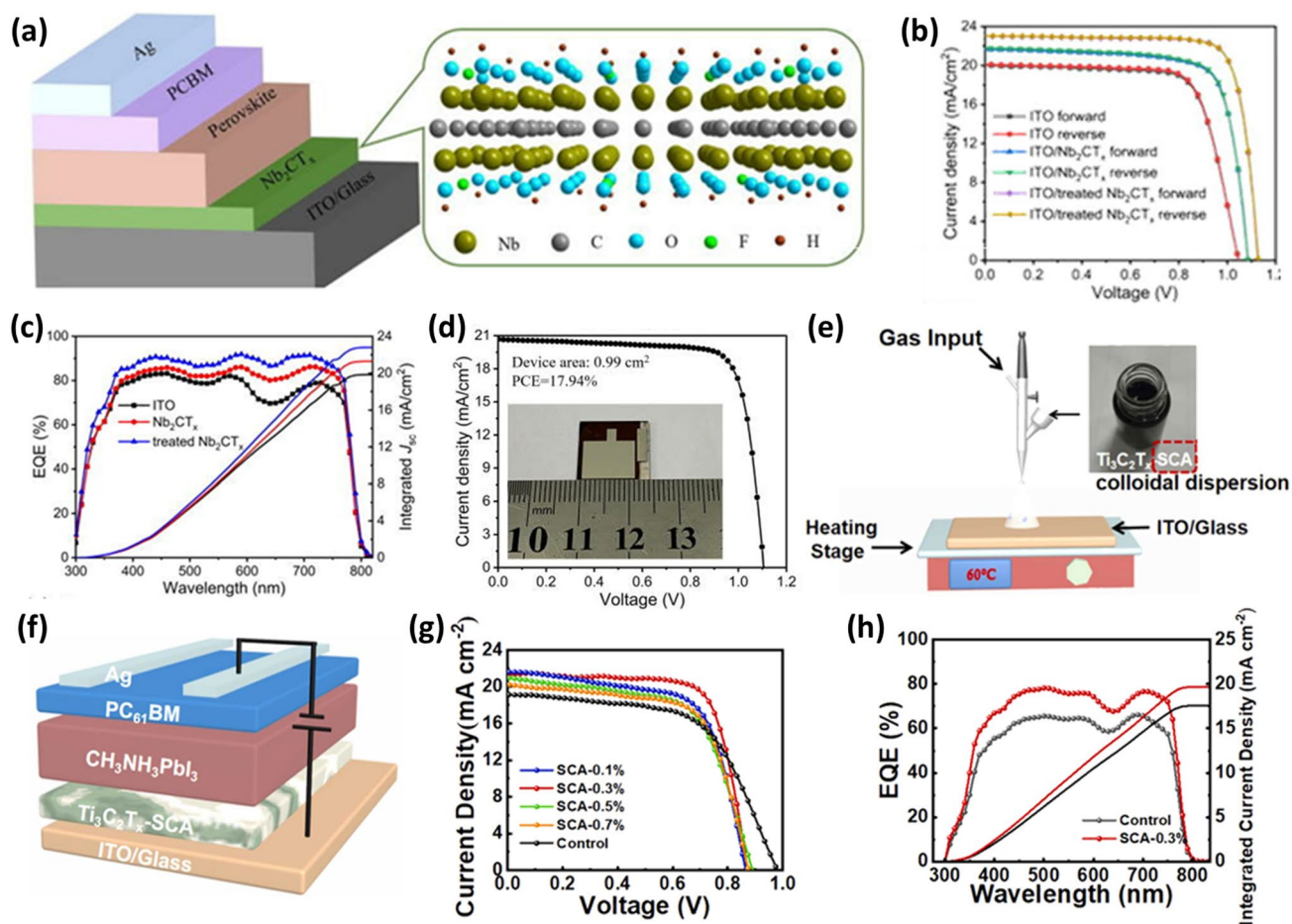


Fig. 9 **a** A schematic diagram of the device structure and the structure of Nb_2CT_x MXene. **b** J - V curves of PVSCs measured under different scan directions. **c** External quantum efficiency (EQE) and integrated J_{sc} curves of different PSCs. **d** J - V curves of the flexible PSCs utilizing oxygen plasma-treated Nb_2CT_x HTL [134]. Copyright © 2021 AIP Publishing. **e** Schematic representation of spray coating process to form the $\text{Ti}_3\text{C}_2\text{T}_x$ -SCA film and structural formula of vinyl tris (2-methoxy ethoxy) silane. **f** Schematic diagram of a device with ITO/HTL/Perovskite/ $\text{PC}_{61}\text{BM}/\text{Ag}$ structure. **g** J - V curve of PSCs based on $\text{Ti}_3\text{C}_2\text{T}_x$, with different volume fractions of SCA as HTL. **h** EQE spectrum and corresponding integrated current density [139]. Copyright © 2022 Elsevier

HTL-based PSCs show excellent long-term stability in the glovebox for 70 days and thermal stability at 85 °C [134].

A silane coupling agent (SCA) can connect various materials and enhance the interface properties [135, 136]. Furthermore, this coupling agent reduces the cost by increasing the corrosion resistance of the material [137, 138]. However, SCA is hard to use directly for bonding. Including hydroxyl groups in SCA is a possibility to improve the interface bonding. In 2022, Du et al. fabricated an HTL by spraying $\text{Ti}_3\text{C}_2\text{T}_x$ MXene nanosheets with varying concentrations of the SCA (vinyltris (2-methoxyethoxysilane)) (0, 0.1, 0.3, 0.5, and 0.7 vol%) [139]. As shown in the schematic of the spray deposition device (Fig. 9e), the ITO glass

substrate is placed on the 60 °C hot stage, and the nozzle of the spray gun is set 20 cm above. The $\text{Ti}_3\text{C}_2\text{T}_x$ -SCA dispersion of different proportions was deposited uniformly on the ITO substrate, setting the spray speed of the spray gun to 2 mL min^{-1} . A flat, pin-hole-free $\text{Ti}_3\text{C}_2\text{T}_x$ film was produced with a mixing content of 0.3 V/V% by utilizing SCA to efficiently adjust the interface distribution of $\text{Ti}_3\text{C}_2\text{T}_x$ after film fabrication. The superior production of $\text{Ti}_3\text{C}_2\text{T}_x$ films enabled better hole transfer paths, improved hole extraction (hole mobility increases from 1.30×10^{-6} to $3.08 \times 10^{-7} \text{ cm}^2 \text{ V}^{-1} \text{ s}^{-1}$), and lower transfer resistance from 369.3Ω to 194.1Ω at the HTL/perovskite interface. The compared values are for the $\text{Ti}_3\text{C}_2\text{T}_x$ HTL and

Ti₃C₂T_x+0.3% SCA HTL. As a result, the device with the structure of ITO/ Ti₃C₂T_x-0.3SCA/MAPbI₃/PC₆₁BM/Ag exhibited an increased PCE from 11.1% (pristine Ti₃C₂T_x) to 13.7%. The schematic of the PSC and the *J*–*V* curves of PSCs with Ti₃C₂T_x-SCA, having different concentrations of SCA, are shown in Fig. 9f–g. However, the *V*_{oc} dropped by 11%. The voltage drop is attributed to stacking due to high surface roughness (root-mean-square (RMS)=0.87 nm for only nanosheet to 4.07 nm for nanosheet and SCA) and good coverage of Ti₃C₂T_x [38, 39]. Additionally, the calculated EQE (17.75 and 19.94 mA cm⁻².) are well consistent with the observed *J*_{sc} variations (19.19 mA cm⁻² and 21.30 mA cm⁻²) for the PSCs with or without SCA (Fig. 9h). Moreover, the PSC based on Ti₃C₂T_x-SCA HTL exhibited excellent stability at ambient air humidity ~20% and room temperature, and retained about 80% of the initial PCE after 80 h of storage [139].

2.5.2 MXenes as Additives in HTLs

As stated earlier, apart from the complexity of synthesis and purification, the poor conductivity, low carrier mobility, resistance to processing solvents, and low transmittance in the UV–vis range of the inorganic HTMs such as CuO_x, Fe₂O₃, CuSCN, and NiO_x and the organic-based polymers

poly (3-hexylthiophene) P3HT, poly(triaryl amine) (PTAA), modified fluorene–dithiophene (FDT), and poly[2,5-bis(2-decyldodecyl)-pyrrolo[3,4-c]pyrrole-1,4(2H,5H)-dione-(E)-1,2-di(2,2'-bithiophen-5-yl)-ethene] (PDPPDBTE) limit the commercial applications as HTLs in PSCs [140–146]. Solution-processed poly (3,4-ethylene dioxythiophene):poly(styrenesulfonate) (PEDOT:PSS) is used as a common HTL due to its high conductivity, appropriate WF, and high transparency. However, its acidic and hygroscopic nature leads to a low efficiency and stability of PSCs [147].

In contrast, transition metal carbide (Mo₂C) and carbon nanotubes (CNTs) are promising HTL candidates owing to their high metallic conductivity, higher charge extraction probability, and tunable WF [148–152]. Hussain et al. combined Mo₂C and CNTs to form a conductive Mo₂C-CNT hybrid network for the first time with a PEDOT:PSS HTL in PSCs with a device configuration of ITO/Mo₂C-CNT@ PEDOT:PSS/MAPbI₃/PCBM/LiF [153]. As seen from the energy-level diagram in Fig. 10a, the absorbed light produces electron–hole pairs as the light is incident on the active layer. The pairs get separated and move toward the ETL and HTL. The modified PEDOT:PSS with Mo₂C-CNT act as exciton dissociation centers and facilitate fast charge separation between MAPbI₃ and ITO and fast charge transfer to the anode. The schematic of the fabricated PSC with the

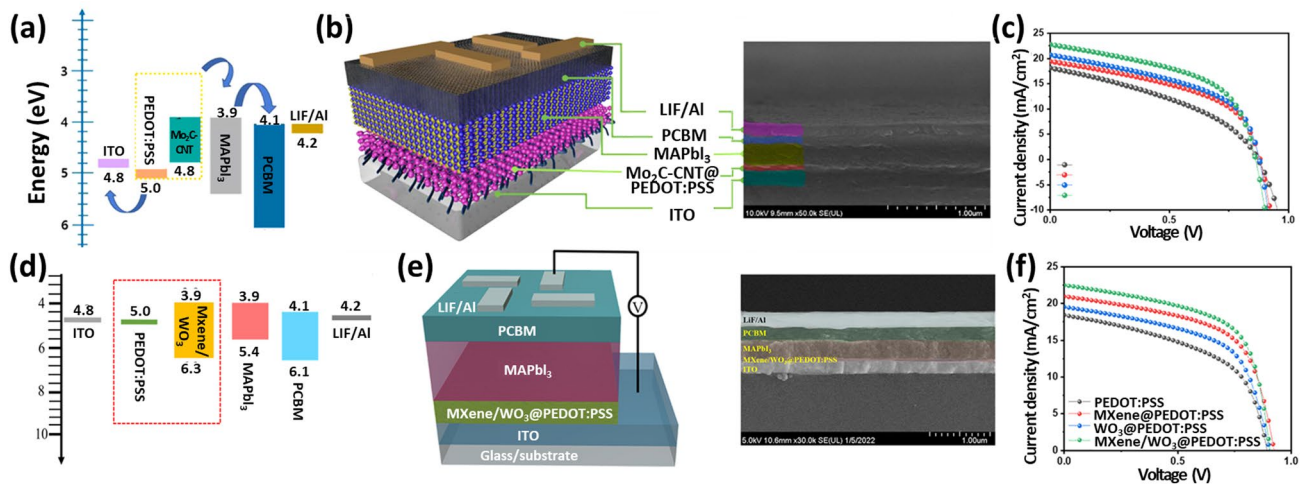


Fig. 10 **a** Energy-level diagram for ITO/Mo₂C-CNTs@PEDOT:PSS/MAPbI₃/PCBM/LiF/Al structure. **b** Schematic of the fabricated PSC with a device architecture of ITO/ITO/Mo₂C-CNTs@PEDOT:PSS/MAPbI₃/PCBM/LiF/Al and its cross-sectional field-emission scanning electron microscopy (FE-SEM) image. **c** *J*–*V* characteristics of prepared PSC devices using pure and 1.5 wt% of Mo₂C, CNTs, and Mo₂C-CNTs blended PEDOT:PSS HTLs [153]. Copyright © 2021 Elsevier. **d** Energy-level diagram, **e** schematic view, and cross-sectional FE-SEM image of the ITO/MXene/WO₃@PEDOT:PSS HTL/MAPbI₃/PCBM/LiF/Al prototype structure. **f** *J*–*V* profiles of PSCs with pure and 2 wt% of WO₃, MXene, and MXene/WO₃ doped HTL [154]. Copyright © 2022 Wiley

modified HTL, 1.5 wt% Mo₂C-CNT@PEDOT:PSS HTL, of PEDOT:PSS and Mo₂C-CNT is shown in Fig. 10b. The PSC with the modified HTL exhibits the highest PCE of 12% compared to 9.2% (Pure PEDOT:PSS), 9.82% (Mo₂C@PEDOPT:PSS) and 10.61% (CNT@PEDOPT:PSS) under AM 1.5 G illumination at 100 mW cm⁻² (Fig. 10c). Additionally, the pure and Mo₂C, CNT, and Mo₂C-CNT blended PEDOT:PSS HTLs showed a conductivity of 410.12, 581.73, 604.25, and 712.34 S cm⁻¹, respectively, thus evidencing high charge carrier collection/extraction and low internal resistance [148]. In further work, Hussain et al. decorated WO₃ nanoparticles on 2D conductive Ti₃C₂T_x MXene sheets to fabricate an MXene/WO₃ hybrid structure and then blended HTL with PEDOT:PSS for PSCs using a simple solution process [154]. The n-type WO₃ semiconducting material is a promising HTL candidate owing to high electron mobilities (10–20 cm² V⁻¹ s⁻¹), a tunable bandgap (2.7–3.9 eV), inexpensiveness, high stability against moisture, and possible fabrication at room temperature [6]. On the other hand, Ti₃C₂T_x MXene possesses high electrical conductivity (2 × 10⁴ S cm⁻¹) and high mobility of 1 cm² V⁻¹ s⁻¹ [28, 30]. An MXene/WO₃ hybrid structure with 1, 2, and 3 wt% was used with PEDOT:PSS to change the perovskite hybrid module's HTL for a highly efficient planar solar cell with a configuration of glass/ITO/MXene/WO₃@PEDOPT:PSS/MAPbI₃/PCBM/LiF/Al. The corresponding energy band diagram and schematic are shown in Fig. 10d–e. The energy band level of MXene/WO₃ is well matched with the perovskite active layer and forms good interfacial contact. The fabricated perovskite solar cell using the optimal device configuration of 2 wt% MXene/WO₃/PEDOT:PSS HTL achieves the highest PCE of 12.26 ± 0.12%. The PCEs of PSCs with pure PEDOT:PSS, WO₃/PEDOT:PSS, and WO₃/PEDOT:PSS are 9.19 ± 0.12%, 10.13 ± 0.14% and 11.42 ± 0.13%, respectively. Furthermore, the PSCs with pure MXene, WO₃, and MXene/WO₃ nanostructure as HTLs show low PCEs of 6.51%, 6.68%, and 6.87%, respectively. Additionally, the RMS surface roughness of the MXene/WO₃ composite with PEDOT:PSS decreases to 21.71 nm for WO₃ (35.79 nm) and MXene (34.23 nm) blended PEDOT:PSS, indicating better adaptable surface behavior with finely dispersed nanoparticles and reduced domain sizes, which results in enhanced interfacial characteristics. The MXene/WO₃ heterostructure also showed high crystallinity, low shunt resistance ~ 5004 ± 68 Ω cm², and series resistance ~ 157 ± 2 Ω cm². These results

suggest better exciton separation and passivation of trapping centers by the densely blended smooth MXene/WO₃ thin films. These blended nanostructures efficiently tune the HTL/perovskite interface through their active interface for charge transfer and collection and suitably alter energy band alignment, resulting in facile charge extraction and the shortest charge carrier lifetime [154].

2.6 MXenes as Electrodes or Additives in Electrodes

The large-scale commercialization of PSCs is constrained by the high cost of commonly used HTM—(Spiro-OMeTAD, PTAA, NiO_x, etc.) and noble metal electrodes (Au and Ag) [155, 156]. Low-cost coal-based carbon electrodes are considered reasonable replacements for both the HTMs and the noble metal electrodes in PSCs. However, the PCEs of PSCs with carbon electrodes are still lower than those of conventional devices. In 2019, Cao et al. were the first to use a more conductive 2D MXene material (Ti₃C₂) with an energy level comparable to carbon materials as back electrodes in HTM and noble-metal-free MAPbI₃ PSCs [157]. Using a straightforward hot-pressing technique at 85 °C and 0.4 MPa, a seamless interfacial contact between the MAPbI₃ perovskite layer and Ti₃C₂ material was achieved, as seen in Fig. 11a–b. The WF of the Ti₃C₂ material was found to be 4.96 eV and matches well with the valence band (5.4 eV) of the MAPbI₃ layer. The hole charge carriers easily transfer from the perovskite layer to the Ti₃C₂ electrode and the electrons from the TiO₂ layer to the FTO electrode. Furthermore, the square resistance decreased from 30.93 to 25.34 Ω sq⁻¹ as the thickness of the Ti₃C₂ electrodes increased from 280 to 330 nm. The Nyquist plot measured under the illumination of 100 mW cm⁻² at a bias voltage of 0.60 V and a frequency range of 100 mHz to 1 MHz shows a similar series and decreased charge transport resistance. The decreased charge transport resistance means efficient hole extraction. However, as the thickness of the electrode increases further, transport resistance increases, and hence the PSC shows low photovoltaic performance. Because of the better conductivity and favorable interfacial contact between the optimally thick Ti₃C₂ electrode and the perovskite layer, the champion PSC based on this electrode with the device structure of FTO/TiO₂/MAPbI₃/Ti₃C₂T_x exhibited a PCE of 13.83% with a V_{oc} of 0.95 V, a J_{sc} of 22.97 mA cm⁻², and an FF of 63% (Fig. 11c). The resulting PCE value is 27% higher than that of the control PSC (10.87%) based on carbon electrodes. A

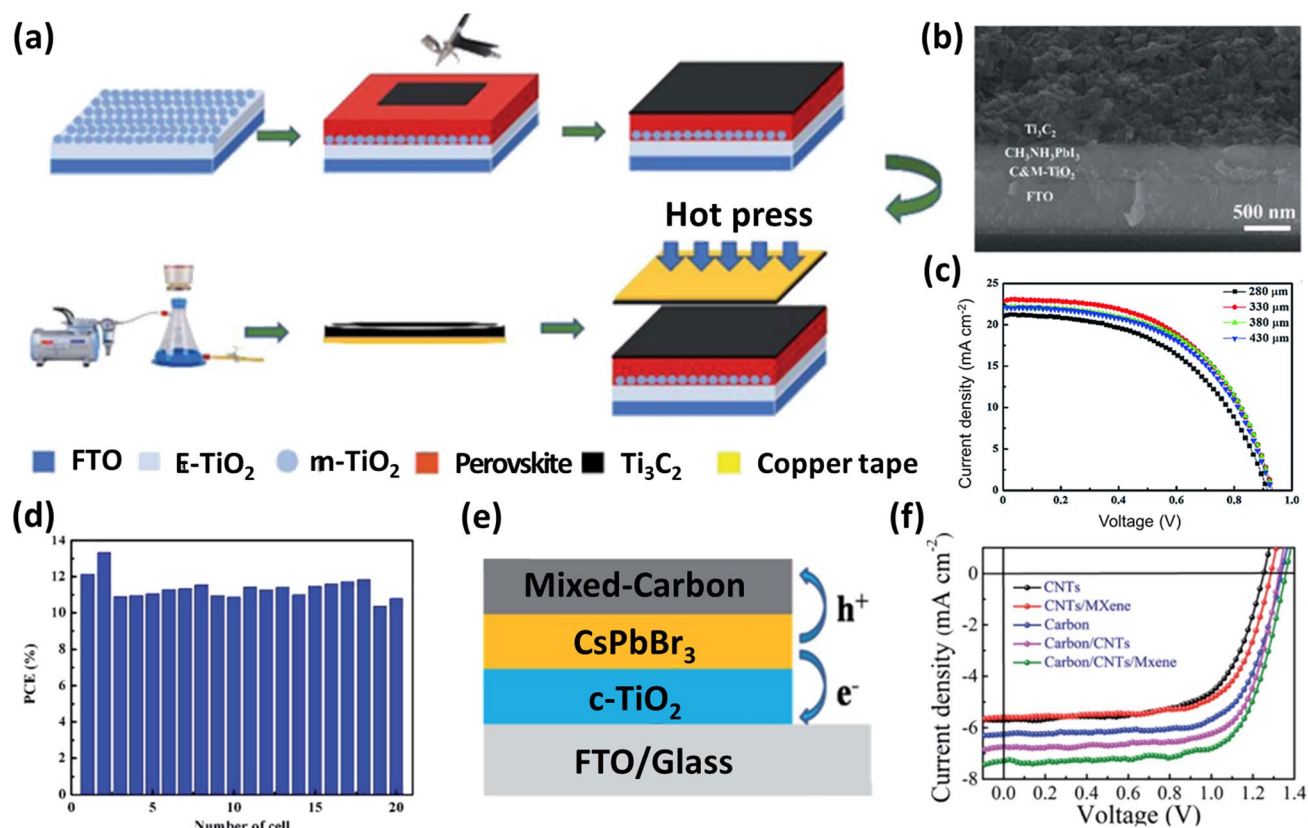


Fig. 11 **a** Schematic diagram showing the fabrication process of the Ti_3C_2 electrode by the hot-pressing method. **b** Cross-sectional SEM image of the PSC based on Ti_3C_2 electrode. **c** $J-V$ curves of devices with different thicknesses of the Ti_3C_2 electrode. **d** PCE histogram of the PSCs obtained from the measurements of 20 devices [157]. Copyright © 2019 The Royal Society of Chemistry. **e** Schematic structure of the CsPbBr_3 solar cell with mixed carbon electrode. **f** $J-V$ curves of devices with different types of electrodes [161]. Copyright © 2020 The Royal Society of Chemistry

good reproducibility in terms of manufacturability without significant batch-to-batch variations was also observed in the fabrication of PSCs based on Ti_3C_2 electrodes (Fig. 11d). The device also demonstrated greater stability than the conventional FTO/compact (c) and mesoporous (m) -TiO_2 /Perovskite/Spiro-OMeTAD/Au device for 360 h when stored at room temperature at an RH of 30%. The Ti_3C_2 electrode plays the role of an encapsulating layer, preventing the active or absorber layer from reacting with air and water [157].

As stated earlier, the high costs of HTMs and noble metals impede the scaling of commercialization of PSCs. The straightforward manufacturing processes, low cost, and great stability of carbon-based inorganic PSCs have shown excellent performance in photovoltaics. Although devices with carbon electrodes are less efficient than those with traditional structures, interest in their potential large-scale applications has grown. However, the commercially available

carbon paste forms a point contact with the perovskite layer because of the point-to-point contact in the carbon electrode. As a result, many pinholes remain at the interface between the electrode and the perovskite layer, impeding the carrier transport [158]. CNTs with a one-dimensional (1D) structure show high conductivity and direct transfer paths for charge carriers, and 2D $\text{Ti}_3\text{C}_2\text{T}_x$ MXene has high surface areas and shows high conductivity via accelerating the charge carriers [31, 124, 159, 160]. In 2020, Mi et al. incorporated commercial CNTs and 2D Ti_3C_2 MXene into the carbon paste and formed a mixed carbon electrode for the inorganic CsPbBr_3 perovskite-based PSC [161]. This mixed carbon electrode offers a network structure and a multi-dimensional charge transfer path due to a good interface with the perovskite absorber layer. MXenes nanosheets fill the voids of carbon powders. This synergistic structure significantly boosts the conductivity of the carbon electrode and carrier transport.

The pure carbon electrode only shows point-to-point contact, and the device with the structure of FTO/c-TiO₂/CsPbBr₃/pure carbon exhibits a PCE of 5.9%. For the inorganic CsPbBr₃ PSC with the mixed carbon electrode, the champion device with the configuration of FTO/c-TiO₂/CsPbBr₃/mixed carbon achieves a decent PCE of 7.09% with a V_{oc} of 1.357 V, a J_{sc} of 7.16 mA cm⁻², and an FF of 72.97% (Fig. 11e–f). Furthermore, the devices with the mixed carbon electrodes show good reproducibility and excellent stability by retaining 80% of their initial PCEs after storage in air for one month [161].

Wearable and other flexible optoelectronic systems require flexible transparent electrodes (FTEs). The excellent conductivity and transparency properties of ITO have placed it as the most reported transparent electrode material among rigid photoelectric devices [162–165]. However, poor mechanical stability (brittleness) and expensive manufacturing equipment costs of ITO electrodes prevent them from being used in flexible electronics. Silver nanowires (AgNWs) have low sheet resistance and high transmittance and are solution-processable [166–168]. They also show super-bending resistance and mechanical stability compared to ITO electrodes. However, AgNWs suffer from high roughness and low adhesion with the substrate and are prone to oxidation and high wire-wire junction resistance [169, 170]. Metal oxide nanoparticles and 2D materials such as electrochemically exfoliated graphene, graphene oxide, and reduced graphene oxide can modify the conductivity and roughness of AgNW networks [171–173]. However, poor doping stability hinders the performance of graphene-based devices [174]. Ti₃C₂T_x MXene, a 2D material, can enhance the performance of AgNW networks due to its high electrical conductivity, carrier mobility, tunable WF, and superior mechanical properties [126, 175]. In 2022, Chen et al. combined 1D AgNWs and 2D Ti₃C₂T_x MXene nanosheets to fabricate composite Ti₃C₂T_x MXene FTEs for flexible solar cell devices [176]. Under electrostatic interaction, a composite 1D:2D structure (AgNW:MXene) FTE is produced. The 1D AgNWs deposited on hydrophilic PET substrates are coated with the MXene nanosheets to form a conductive AgNW:MXene composite network, as shown in Fig. 12a. The MXene nanosheets weld the crossing junctions and the broken junctions. Using capillary force, 2D MXene nanosheets fill the gaps in the AgNW networks and join the wire-wire connections. These provide more

continuous conductive paths, improving the conductivity of the electrodes. Additionally, the oxygen-containing functional groups of MXene nanosheets adhere strongly to the PET substrate via a strong hydrogen bonding interaction. The photoelectric performance of FTEs is determined by the figure of merit (FoM). The FTE fabricated with 5 mg mL⁻¹ AgNWs dispersion deposited with a concentration of 0.5 mg mL⁻¹ MXene shows an FoM by a low sheet resistance of 10.91 Ω sq⁻¹ (12.09 Ω sq⁻¹ for AgNW without MXene) and a high transmittance of 82.84% (81.96%) at 550 nm. The roughness of the AgNW:MXene FTEs is also decreased, as observed from the RMS roughness of AgNW:MXene FTEs (13.6 nm) compared to the pristine AgNW FTEs (19.2 nm). The mechanical endurance of FTEs determines the ability of FTE to sustain a continuous conductive path to collect charge under an external mechanical stress [177]. The PET/AgNW:MXene shows a surface Young's modulus of 0.78 GPa, compared to 0.96 and 1.15 GPa of PET/ITO and PET/AgNW, respectively. Additionally, the AgNW:MXene FTEs exhibit superior long-term stability at 60% RH and 120 °C for 240 h, as well as strong mechanical resilience after 1,000 cycles of bending tests at a 5 mm curvature radius. Furthermore, WF matching is important for accelerating the charge transfer. The WF of AgNW:MXene is calculated to be 4.81 eV, which lies in the required normal range for optoelectronic devices. As a result, the inverted PSC with a device structure of PET/AgNW:MXene/NiO_x/Perovskite/PC₆₁BM/Ag (Fig. 12b) and an area of 0.1 cm² show a high PCE of 20.22% (18.7% for the cell with pristine AgNWs only) with V_{oc} of 1.06 V, J_{sc} of 25.16 mA cm⁻², and FF of 75.5% (Fig. 12c) [176].

3 MXenes as Interfacial Layers

3.1 At the Interfaces Between Perovskites and Electrodes

MXenes are promising candidates in photovoltaics because of their high transmittance, tunable WF (2.14–5.65 eV), and metallic conductivity. Chen et al. introduced 2D Ti₃C₂ MXene nanosheets as an interlayer into all-inorganic CsPbBr₃ PSCs for the first time [160]. The MXene interlayer was formed on the FTO/c-TiO₂/CsPbBr₃ substrate via spin-coating of the Ti₃C₂ MXene nanosheet dispersion

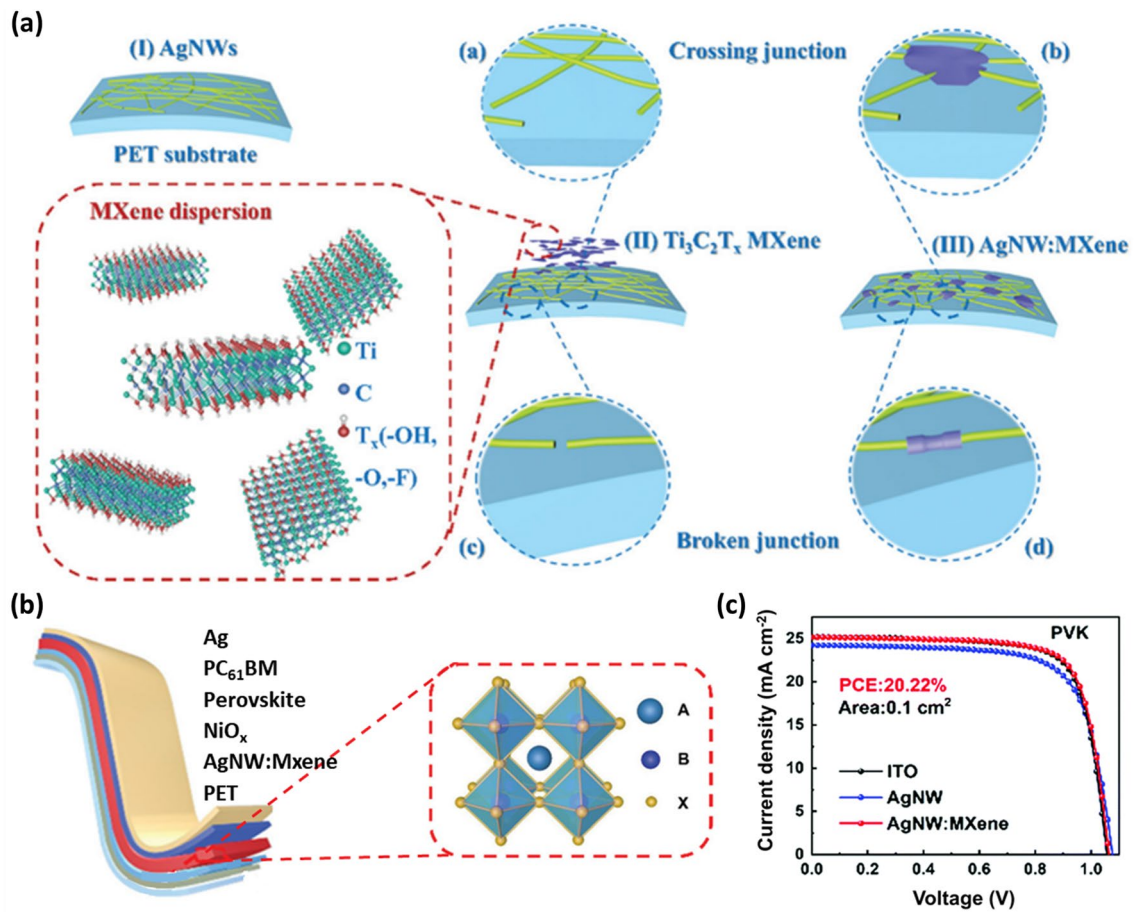


Fig. 12 a Schematic of the $Ti_3C_2T_x$ MXene and the fabrication procedure of AgNW:MXene flexible transparent conductive electrodes. b Flexible PSCs with the structure of PET/AgNW:MXene/ NiO_x /Perovskite/ $PC_{61}BM$ /Ag. c $J-V$ curves of the flexible PSCs based on ITO, AgNW, and AgNW:MXene electrodes [176]. Copyright © 2022 The Royal Society of Chemistry

solution (Fig. 13a–b). The selected area electron diffraction (SAED) pattern of Ti_3C_2 MXene nanosheets shows a few highly crystalline layers with the device structure of FTO/ TiO_2 / $CsPbBr_3$ / Ti_3C_2 MXene/Carbon to achieve a better interfacial energy-level alignment, which aids in the elimination of the energy-level mismatch, speeds up hole extraction, and lowers recombination at the interface of the perovskite/carbon electrode. Additionally, the Ti_3C_2 MXene nanosheets’ surface functional groups offer powerful interactions between the MXene and under-coordinated Pb atoms. This significantly lessens the deep trap defects in the $CsPbBr_3$ films. The device with the Ti_3C_2 -MXene interlayer displays an exceptional initial PCE of $\sim 9\%$ (Fig. 13c), with a long-term stability of more than 1900 h

in a moist environment and more than 600 h under heat circumstances [160].

3.2 At the Interfaces Between Perovskites and ETLs

Proper device design and specialized interface engineering are required to improve optoelectronic characteristics and the charge extraction process at the selective electrodes to increase the PCE of PSCs. In 2019, Agresti et al. used 2D $Ti_3C_2T_x$ MXene ($T_x = -O, -OH, \text{ and } -F$) to tune the WF of the perovskite absorber and engineered a perovskite/ETL interface. It was observed that the OH-terminated surface of MXene reduced the WF of the perovskite, while the O-terminated surface increased the WF. This nonlinear

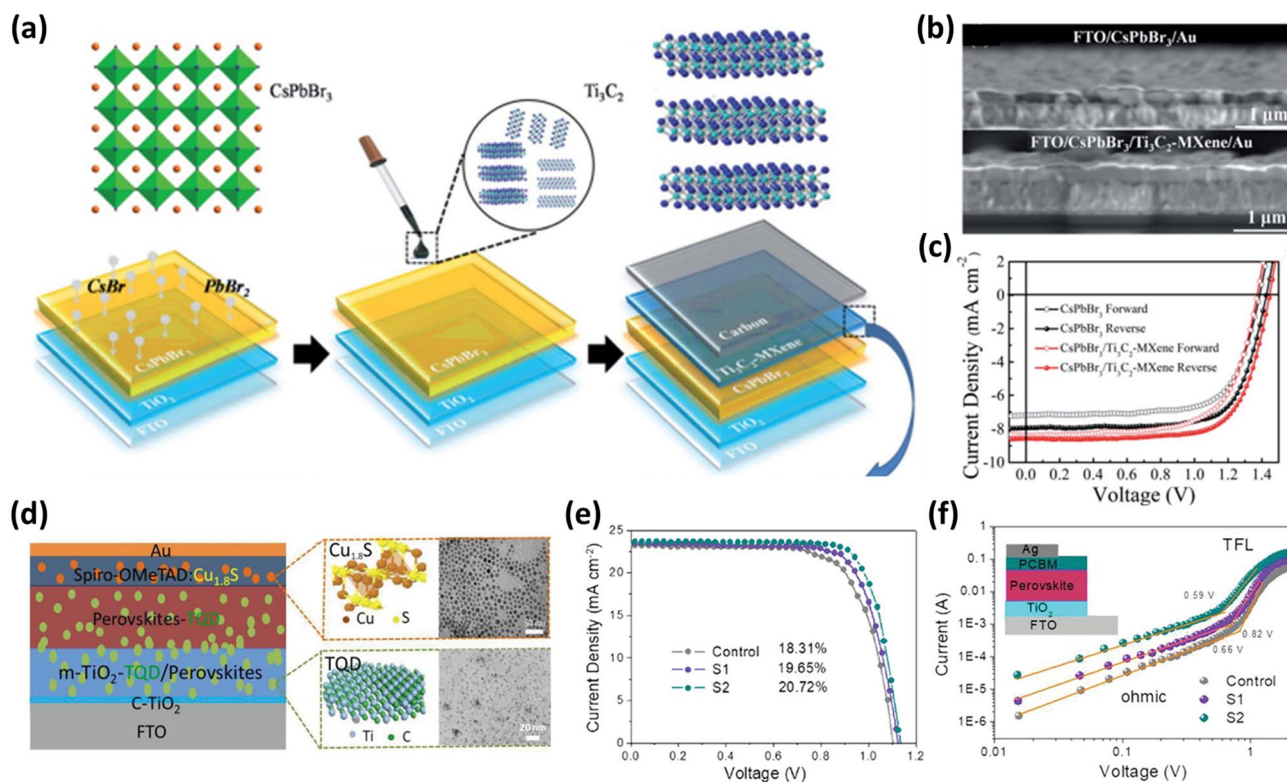


Fig. 13 **a** Crystal structure diagrams of CsPbBr₃ and Ti₃C₂ MXene, and schematic for the fabrication of the CsPbBr₃/Ti₃C₂ MXene-based solar cell. **b** Cross-sectional SEM images of FTO/CsPbBr₃/Au devices with/without Ti₃C₂ MXene. **c** *J-V* curves of devices with/without Ti₃C₂ MXene [160]. Copyright © 2019 The Royal Society of Chemistry. **d** Architecture of the perovskite solar cells, schematic structure and TEM images of Cu_{1.8}S and Ti₃C₂ QDs, and the cross-sectional SEM of a complete device. **e** *J-V* curves for FTO/TiO₂/perovskite, FTO/TiO₂/MQD/perovskite, and FTO/TiO₂/MQD/MQD-perovskite devices measured under simulated AM 1.5 sunlight of 100 mW cm⁻² irradiance. **f** Double logarithmic *J-V* characteristics in electron-only devices with the structure of FTO/TiO₂/Perovskite/PCBM/Ag (control), FTO/TiO₂/TQD/Perovskite/PCBM/Ag (S1), and FTO/TiO₂/TQD-Perovskite/PCBM/Ag (S2) devices [180]. Copyright © 2020 WILEY-VCH Verlag GmbH & Co. KGaA, Weinheim

behavior is reported in the literature [178]. Furthermore, light absorption was increased in MXene-doped perovskites. The addition of Ti₃C₂T_x to halide perovskite and TiO₂ layers enables the adjustment of the materials' WFs without changing the other electronic characteristics. The PSC with MXene-doped perovskite active layer also showed higher PCE (17.4%) than that with the un-doped perovskite absorber layer (15.6%) [179]. Additionally, the band alignment between these layers can be altered using the dipole induced by Ti₃C₂T_x at the perovskite/ETL interface. WF tuning and interface engineering work together to significantly improve the PCE of MXene-modified PSCs to 20% with a V_{oc} of 1.09 V, a J_{sc} of 23.82 mA cm⁻² and an FF of 77.6%, as well as a reduction in hysteresis compared to reference cells without MXene [179]. Chen et al. used Ti₃C₂T_x QDs (TQDs) to engineer a perovskite/TiO₂ ETL interface and

perovskite absorber and introduced Cu_{1.8}S nanocrystals to optimize the Spiro-OMeTAD HTL in PSCs (Fig. 13d) [180]. The QDs with a diameter of about 5.2 nm and a thickness of ~1 nm in the absorber layer significantly contribute to the improved crystalline quality of the perovskite film, and large grain sizes are formed. Furthermore, TQDs improve electron extraction and collection at the perovskite/ETL. Cu_{1.8}S improves the hole extraction at perovskite/HTL interfaces. With the improved J_{sc} , V_{oc} , and FF because of the synergistic effect of both TQD/Cu_{1.8}S, the hysteresis-free PCE of PSCs significantly increased from 18.3 to 21.6% (V_{oc} of 1.14 V, J_{sc} of 24.12 mA cm⁻², FF of 78.70%) (Fig. 13e). The TQD and/or Cu_{1.8}S nanocrystals doping also significantly improves the long-term ambient and light stability of PSCs by improving perovskite crystallization, reducing HTL film aggregation and crystallization, and preventing

ETL from ultraviolet-induced photocatalysis. The results show that TQD and $\text{Cu}_{1.8}\text{S}$ can function as ultrafast electron and hole tunnels for optoelectronic devices. The trap-filled limit voltage (V_{TFL}) values of FTO/ TiO_2 /Perovskite/PCBM/Ag (control), FTO/ TiO_2 /MQD/Perovskite/PCBM/Ag (S1), and FTO/ TiO_2 /MQD/MQD-Perovskite/PCBM/Ag (S2) electron-only devices were found to be 0.82, 0.66, and 0.59 V, respectively. The electron trap-state densities of perovskites are $1.59 \times 10^{16} \text{ cm}^{-3}$ (control), $1.28 \times 10^{16} \text{ cm}^{-3}$ (S1), and $1.15 \times 10^{16} \text{ cm}^{-3}$ (S2) (Fig. 13f). The large grain size and low grain boundary density in the perovskite film resulted in a lower trap density [180]. Crystal deformations, such as lattice strain at the surfaces and grain boundaries, owing to the soft perovskite lattice, affect the charge extraction-transfer dynamics and recombination, leading to a low PCE. Zhou et al. added an inorganic 2D $\text{Ti}_3\text{C}_2\text{Cl}_x$ MXene to the bulk and surface of the CsPbBr_3 film [90]. This method dramatically reduces the superficial lattice tensile strain. The expanded perovskite lattice is compressed and confined to act as lattice "tape", in which the Pb-Cl bond functions as "glue", and the 2D Ti_3C_2 immobilizes the lattice. This compression and confinement result from the strong interaction between Cl atoms in $\text{Ti}_3\text{C}_2\text{Cl}_x$ and the under-coordinated Pb^{2+} in the CsPbBr_3 lattice. Under light irradiation, the carrier transfer is affected because defects and strain are introduced to the perovskite film. Hence, a smaller number of holes is available at the perovskite top surface. The MXene interlayer, defective states, and grain boundaries are passivated, leading to the availability of charge carriers and thus enhanced photovoltage. The champion all-inorganic CsPbBr_3 PSC is finally able to attain the PCE as high as 11.08% with an ultrahigh V_{oc} up to 1.702 V, which is the highest efficiency record for this type of PSCs to date. Additionally, the unencapsulated device exhibits almost unaltered performance at 85 °C for 30 days and at 80% RH for 100 days [90].

High-efficiency photovoltaic (PV) devices can be produced by adding 2D MXenes to the ETL of PSCs. However, the oxidation that results from the ambient fabrication of the ETLs causes an inevitable decline in the electrical characteristics of MXene. To enhance the photovoltaic performance of PSCs, Bati et al. used metallic single-walled carbon nanotubes (m-SWCNTs) to make MXene/SWCNT composites [181]. The champion device with a configuration of ITO/ SnO_2 :MXene/SWCNT(2:1)/(FAPbI₃)_x(MAPbBr₃)_{1-x}/Spiro-OMeTAD/Au attained a maximum PCE of 21.42%, a J_{sc} of 25.09 mA cm^{-2} , a V_{oc} of 1.073 V and an FF of 80% with

the optimum composition. The improved PL and reduced charge transfer resistance confirmed a low trap density and improved charge extraction and transport characteristics owing to the improved conductivity facilitated by the presence of carbon nanotubes and decreased oxygen vacancies on the surface of SnO_2 . The MXene/SWCNTs approach offers a promising route to realize high-performance PSCs [125, 181].

As discussed earlier, the major causes of PSCs' instability and low PCE are defects at the interfaces of perovskite thin films. Wu et al. used a composite ETL made of SnO_2 -MXene to enhance interfacial contact and passivate defects at the SnO_2 /perovskite interface in PSCs [182]. The newly developed MXene controls SnO_2 dispersion and allows the perovskite film to grow vertically. The Lewis acid-base interaction of the -OH functional groups on the MXene surface and Sn atoms in SnO_2 weakens the van der Waals interactions between neighboring crystals, impeding the accumulation of SnO_2 nanocrystals. The lattice matching between MXene and perovskite nullifies the generated interfacial stress and induces vertical growth of perovskites (Fig. 14a). The average grain size of SnO_2 -MXene/perovskite ($\sim 1 \mu\text{m}$) increased compared to the grain size of the control SnO_2 /perovskite ($\sim 356 \text{ nm}$). Additionally, the conductivity of SnO_2 increased from 1.85×10 to $9.62 \times 10 \text{ S cm}^{-1}$. This resulted in a higher current in MXene-PSCs (25.07 mA cm^{-2}) than in pristine PSCs (24.16 mA cm^{-2}). The lifetime of SnO_2 /perovskite ($\tau_1 = 20.73 \text{ ns}$, $\tau_2 = 80.24 \text{ ns}$) is longer than that of charge carriers in SnO_2 -MXene/perovskite ($\tau_1 = 17.34 \text{ ns}$, $\tau_2 = 48.20 \text{ ns}$). Hence charges are extracted faster in the SnO_2 -MXene ETL than in the pristine SnO_2 ETL. Moreover, the MXene introduction also downshifts the valence band edge to -7.93 eV (SnO_2 -MXene) from -7.72 eV (SnO_2), which indicates the suppression of hole recombination and hole migration to the ITO electrode (Fig. 14b). The PCE of the SnO_2 -MXene-based device with a structure of ITO/ SnO_2 -MXene/Perovskite/Spiro-OMeTAD/Au attained a PCE of 23.07%, with a V_{oc} of 1.13 eV, a J_{sc} of 25.07 mA cm^{-2} , and an FF of 81.1%. The attained PCE is 15% higher than for the SnO_2 -based device (20.03%). Furthermore, even after 500 h of storage at 30–40% relative humidity in ambient air, the unencapsulated device still retained almost 90% of its initial PCE [182].

Another research group led by Liu et al. used Au@ Nb_2CT_x -MXene in PSCs to nullify charge accumulation and interfacial defects at SnO_2 , leading to poor charge transfer

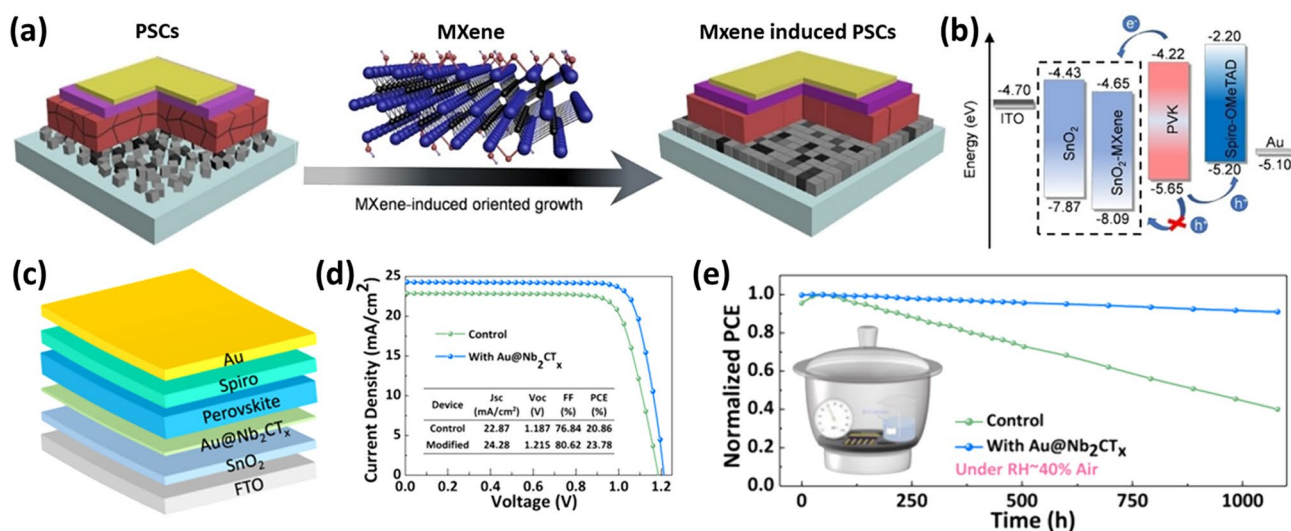


Fig. 14 **a** Schematic of PSCs and MXene-PSCs films, MXene induces vertical growth of perovskite and improves the interfacial contact between perovskite and SnO₂. **b** Energy level diagram of the device SnO₂- MXene interface illustrating hindrance of hole transport [182]. Copyright © 2022 Wiley. **c** Structure of PSCs modified by Au@Nb₂CT_x- MXene. **d** *J* / *V* curves of the control and Au@Nb₂CT_x-MXene-modified devices measured under the reverse scan. **e** Stability test of the control and Au@Nb₂CT_x- MXene-modified PSCs in ambient air under RH ~ 40% for over 1000 h [184]. Copyright © 2023 American Chemical Society

from the perovskite layer to the charge transport layer [183]. An Nb₂CT_x-MXene multilayer was obtained by Nb₂AlCl via selective etching of Al atoms by HF treatment, and a further MXene monolayer was derived from the multilayer via tetramethylammonium hydroxide (TMAOH) treatment. Further, Au nanoparticles were coated on MXenes to form Au@Nb₂CT_x-MXene (Fig. 14c). In PSCs, Nb₂CT_x- MXene increases conductivity (3.37×10^{-6} S cm⁻¹), thus lowering Sn vacancies in the SnO₂ layer's interstitial void and consequently lowering defect density and aligning the band-gap. With the inclusion of Au NPs, Au@Nb₂CT_x-MXene improves the perovskite film quality, controls the tensile tension of perovskites, and stifles Auger recombination. As a result, the Au@Nb₂CT_x-MXene-modified device exhibits a very high *V*_{oc} of 1.215 V, a *J*_{sc} of 24.28 mA cm⁻², an FF of 80.62%, and a PCE of 23.78%, compared to the control device with Nb₂CT_x- MXene (PCE of 20.86%) (Fig. 14d). In addition, the unencapsulated devices preserve 90% of their initial PCE values after being exposed to air with a relative humidity of 40% for 1000 h and continue to function at or above 80% of their initial efficiency after being exposed to sunlight for 500 h (Fig. 14e) [183].

As reported earlier by Zhou et al., 2D Ti₃C₂Cl_x MXene was inserted into the bulk and surface of CsPbBr₃ film [90]. The 2D Ti₃C₂Cl_x MXene was deposited on the surface of

SnO₂ ETL. Inclusion of MXenes into bulk and surface of the device results in decreased defects and strains and leaving more holes for larger voltage (Fig. 15a–b). The defect reduction can be quantified in terms of the reduced trap-filled limit voltage (*V*_{TFL}). The *V*_{TFL} decreases from 0.78 (pristine) to 0.56 V for Ti₃C₂Cl_x passivated perovskite film and the defect density (*n*_t) decreased from 5.93×10^{15} to 1.92×10^{15} cm⁻³, respectively (Fig. 15c).

3.3 At the Interfaces Between Perovskites and HTLs

CsPbI₃ inorganic perovskites have garnered much interest for their outstanding thermal stability and suitable band-gap for tandem solar cells. However, due to nonradiative recombination, CsPbI₃ PSCs show low PCEs and a high *V*_{oc} loss (0.5 vs. 0.3 V for hybrid perovskites) [184]. To improve the functionality of CsPbI₃ PSCs, Xu et al. synthesized Ti₃C₂F_x MQDs with abundant Ti–F groups by a liquid-phase exfoliation technology and used them as interface passivators [185]. The Ti₃C₂F_x MQDs function as efficient passivators primarily in three ways: 1) p-type Ti₃C₂F_x MQDs can adjust the energy levels of perovskite films and provide a reliable pathway for hole transfer; 2) Ti₃C₂F_x MQDs can effectively passivate defects and reduce interfacial nonradiative recombination; and

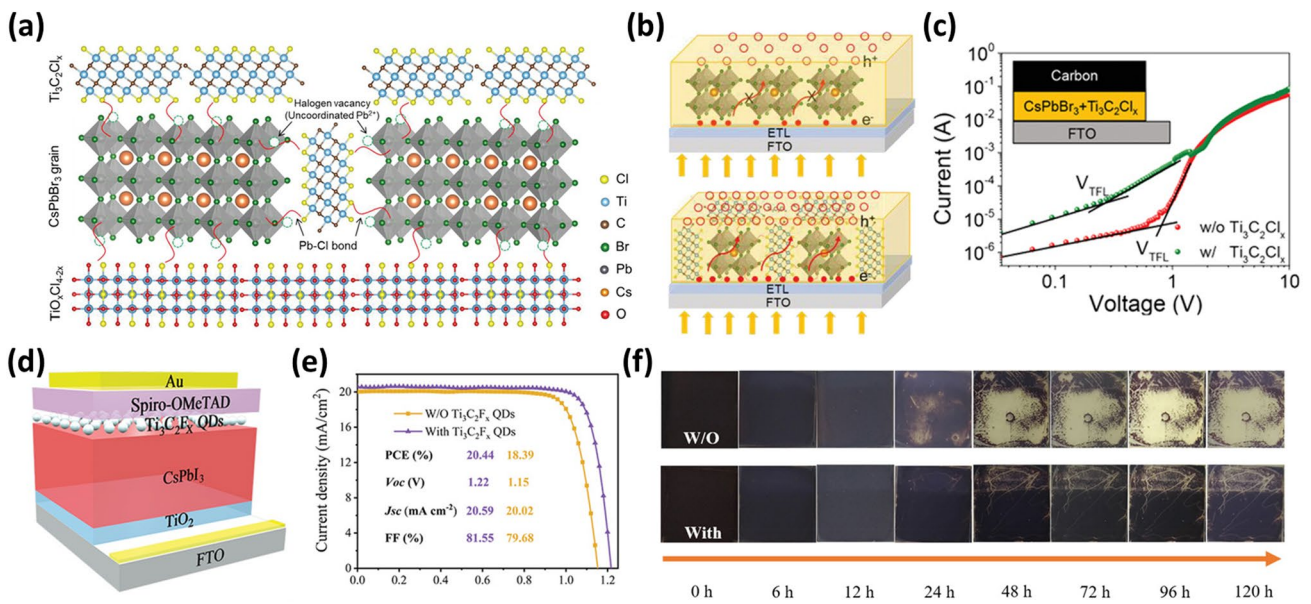


Fig. 15 **a** Schematic diagram of full defect passivation in CsPbBr₃ film by Ti₃C₂Cl_x MXene. **b** Illustration for the photogenerated carrier transfer in pristine and Ti₃C₂Cl_x containing perovskite films. **c** Dark *J*–*V* curves for the hole-only devices with and without Ti₃C₂Cl_x MXene [90]. Copyright © 2021 Wiley–VCH GmbH. **d** Schematic image of a CsPbI₃ PSC with the structure of FTO/TiO₂/CsPbI₃/Ti₃C₂F_x QDs/Spiro-OMeTAD/Au. **e** *J*–*V* curves of devices comprising pristine and Ti₃C₂F_x QDs treated CsPbI₃ films. **f** Photographs of control and Ti₃C₂F_x QDs-treated CsPbI₃ films aged in ambient air conditions (RH: ≈35%, T = 25 °C) [185]. Copyright © 2022 Wiley

3) Ti₃C₂F_x MQDs form a barrier layer. As a result, the champion CsPbI₃ PSC treated with Ti₃C₂F_x MQDs (FTO/TiO₂/CsPbI₃/Ti₃C₂F_x MQDs/Spiro-OMeTAD/Au) displays excellent PCE of 20.4% (18.4% for the pristine) with high *V*_{oc} of 1.22 V, *J*_{sc} of 20.59 mA cm⁻², and FF of 81.5% (Fig. 15d). The air stability of Ti₃C₂F_x MQDs treated CsPbI₃ film is remarkably enhanced after 120 h of storage in air with an RH of 35%, as shown in the photographs of the films (Fig. 15e). In addition, after 600 h of storage in ambient air, the target device without encapsulation maintained 93% of its initial efficiency [185].

Even at ambient temperatures, the perovskites based on formamidinium (FA) suffer an unnecessary spontaneous yellow phase transition yet promise a high PCE in photovoltaics. This has inspired significant efforts, which pose a formidable challenge to the soft perovskite lattice’s powerful anchoring. To effectively delay the lattice instability in FA-based perovskites, Guo et al. developed a rational design of interfacial ionic bonding between halogen (F, Cl, Br or I)-terminated nano-MXenes and perovskites [186]. They used pulsed laser irradiation to produce the halogen-terminated nano-MXenes using the green anti-solvent of

ethyl acetate (Fig. 16a). The halogen-terminated nano-MXenes form heterointerfaces between nanocrystals and the perovskite (Fig. 16b–c). The strong heterointerface between perovskite and nano-MXenes also allows for efficient control of the WF of perovskite films, lowering of the interfacial charge transfer barrier, and effective modulation of deep-energy-level defects. The champion device with a structure of FTO/TiO₂/FAPbI₃/nano-Ti₃C₂T_x/Spiro-OMeTAD/Au attained the highest PCE of 24.2%, a *J*_{sc} of 25.84 mA cm⁻², a *V*_{oc} of 1.132 V and an FF of 82.6%. This is the highest efficiency utilizing MXene in PSCs reported so far. The stabilized power outputs for the pristine and the modified PSCs are 22.07% and 23.79%, respectively (Fig. 16d). These advantages enable unencapsulated FA-based perovskite solar cells to maintain over 90% of their initial efficiency after operation at maximum power point under continuous illumination for 1000 h and more than 85% of their initial efficiency even after annealing for 1000 h at 85 °C in an inert atmosphere [186].

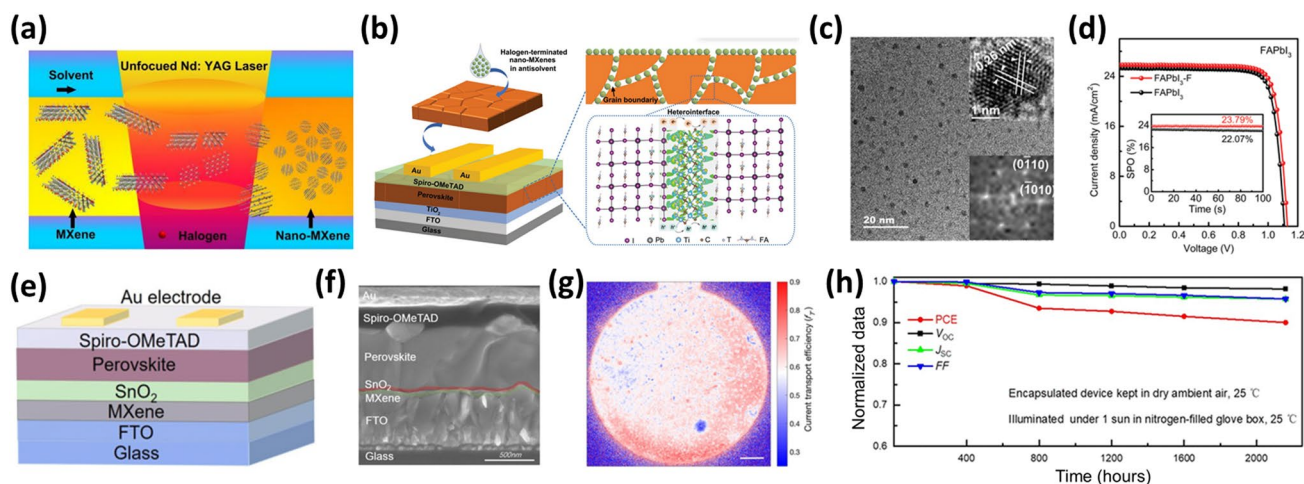


Fig. 16 **a** Schematic diagram of nano-MXenes prepared via the pulsed laser irradiation. **b** Schematic of ionic-bonding heterointerface of hybrid perovskite via interfacial embedding of halogen-terminated nano-MXenes, Pb-T based ionic lattice anchoring and carrier dynamics modulation. **c** High-resolution transmission electron microscopy images and fast fourier transform patterns of nano- $\text{Ti}_3\text{C}_2\text{F}_x$. **d** J - V curves of the champion PSCs based on FAPbI_3 films and the stabilized power outputs of the corresponding devices (insets) [187]. Copyright © 2022 Wiley-VCH GmbH. **e-f** Device configuration and cross-sectional SEM image of the entire device. **g** Spatially resolved f_T maps of MXene-modified devices (scale bar, 1 mm). **h** Shelf lifetime tracking of the optimized PSC [191]. Copyright © 2020 American Chemical Society

3.4 At the Interfaces Between ETLs and Electrodes

The high annealing temperature ($> 450^\circ\text{C}$), critical photo-instability of TiO_2 , and spontaneous aggregation of SnO_2 hinder the scale-up of the commercial application of PSCs [187–189]. Furthermore, inadequate charge extraction and hysteresis are due to the energy-level mismatch between the conduction band minimum (CBM) of SnO_2 and the WF of FTO at the interface. Hence interface engineering is essential for charge extraction in PSCs. Wang et al. introduced a strong interface interacting with 2D carbide MXene to improve the electron mobility and charge transfer ability of SnO_2 ETL (Fig. 16e–f) [190]. The MXene-modified SnO_2 ETL induced a preferable growth orientation route for perovskite films. It reduced the trap density and thereby reduced the non-radiative recombination. As shown in Fig. 16g, the MXene-modified device has a few localized defects, and the carrier transport is homogeneously enhanced, as reflected by the current transport efficiency (f_T) values over the active area of the entire device. Furthermore, the modified SnO_2 /perovskite interface provided a better platform for charge extraction and transfer. The PSC with MXene-modified SnO_2 and a device structure of $\text{FTO}/(0.5 \text{ mg mL}^{-1} \text{ MXene})/\text{SnO}_2/\text{Perovskite}/\text{Spiro-OMeTAD}/\text{Au}$ achieved a PCE of 20.7%

with ultralow saturated current density and negligible hysteresis. Moreover, the champion PSC demonstrated an excellent shelf lifetime by retaining 90% of its initial PCE after 3 months. However, no significant degradation is observed in the V_{oc} of the PSC with an MXene interlayer (Fig. 16h) [190].

The electrical conductivity of 2D MXene can be adjusted by changing the termination groups and applying controlled oxidation, which has enormous promise for solar applications. Yang et al. added in-situ oxidized $\text{Ti}_3\text{C}_2\text{T}_x$ ($\text{O-Ti}_3\text{C}_2\text{T}_x$) MXene to create a nanoscale heterojunction with SnO_2 that was used as an ETL in a MAPbI_3 PSC with a device structure of $\text{FTO}/\text{O-Ti}_3\text{C}_2\text{T}_x/\text{SnO}_2/\text{MAPbI}_3/\text{Spiro-OMeTAD}/\text{Ag}$ [191]. The properties of $\text{Ti}_3\text{C}_2\text{T}_x$ are modified to have their energy levels well-matched with the perovskite by taking advantage of the change from metallicity to semiconductor during the oxidation process. Additionally, the $\text{O-Ti}_3\text{C}_2\text{T}_x$ insertion increased the SnO_2 ETL electron mobility. As a result, the $\text{O-Ti}_3\text{C}_2\text{T}_x/\text{SnO}_2$ heterojunction provided better electron extraction and decreased recombination between the ETL and the perovskite, increased PCE from 17.7 to 20.1%, and enhanced stability with preserving 80% of its initial PCE in air [191].

4 Prospects and Conclusions

MXenes have significantly impacted the device performance and stability of the PSCs. The roles and functions of MXenes in PSCs are summarized as shown in Fig. 17. As an application, a detailed overview of MXenes in PSCs starting from the first report in 2018 to recent advances, has been provided. MXenes play multiple roles as different components of PSC. The roles are broadly divided into five categories depending on their functions: additive in perovskite absorber layers, ETLs/additives in ETLs, HTLs/additives in HTL, electrodes, and interfacial layers. As additives in absorbers, MXenes retard the crystallization rate and enlarge the crystal sizes of perovskites by controlling the morphology. Furthermore, MXenes mitigate perovskite lattice instability and passivate the bulk and surface defects, prolonging the carrier lifetimes and reducing charge recombination. In addition, these materials induce hydrophobic features on the surface of the absorber layer and prevent deprotonation of protonated organic amine in perovskites. Most importantly, MXenes can tune the work function of the perovskite absorber layer for efficient charge transfer. The combined effect of these features improves the PCE and stability of the PSCs. Similarly, as/in ETL, MXenes tune the work functions of the ETLs for well-matched band alignment with the perovskite layer to facilitate smooth electron transport. These observations are further supported by the improved electron mobilities and the reduced interface recombination for the ETL/perovskite. In addition, MXenes mitigate the defects in the ETL layer, which is a prerequisite for improved crystallinity of the next perovskite layer. As electrodes, MXenes pose as emerging materials in transparent hybrid electrodes in PSCs. MXenes as/or in HTLs provide a superior hole transfer path, improve hole extraction, and decrease charge transfer resistance at the HTL/perovskite interface via tuning the WF of the HTLs. The presence of MXenes in electrodes provides improved adhesion to the substrates and superior continuous conductive paths for improved electrical conductivity. In addition, because of their low square resistance, MXenes act as promising electrodes. MXenes are also used as additional interfacial layers in ETL/electrodes, perovskite/electrode, perovskite/ETL, and perovskite/HTL layers. These layers help in efficient charge extractions and transfers via improved

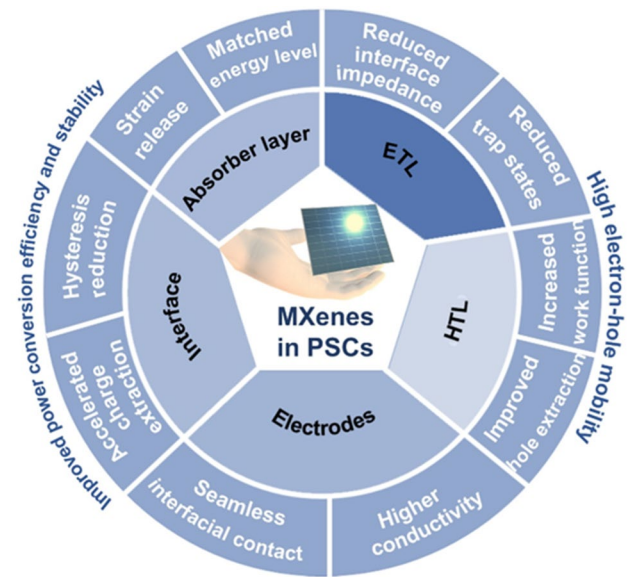


Fig. 17 Positions and functions of MXenes in PSCs

interfacial energy alignment, reduce recombination (trap defects) at the interfaces, provide a well-controlled growth platform for smooth perovskite films, and passivate perovskite grains for improved film quality. These essential features provide a promising route for highly efficient and stable PSCs. Different roles of MXenes and their photovoltaic performance in PSCs are summarized in Tables 1, 2, 3, 4, and 5. Until now, MXene-assisted PSCs have attained the highest PCE of 24.17% and the highest reported stability time reported so far is 2000 h. In addition, the PSCs with a large area of 0.99 cm² and the minimodules with the size of 25 cm² are reported so far. However, MXene's applications in perovskite solar cells are in their infancy, and many advancements are yet to come. Several distinct MXenes with varying compositions, surface terminations, band topologies, and WFs have been reported. However, only a limited number of MXenes such as Ti₃C₂T_x (T_x = -O, -OH, -F, -Cl, -Br, -I, -NH₂), V₂CT_x, Mo₂C, and Nb₂CT_x have been reported in PSCs so far. Hence theoretical studies are required to further understand the charge transport/extraction behavior and WF modification of new MXene compositions, MXene/perovskite, MXene/ETL, and MXene/HTL interfaces. A more detailed theoretical investigation is required to elucidate the optical, electrical, and mechanical properties of MXenes, effects of various termination groups of MXenes, surface modifications, variation of WF, and energy-level

Table 1 Role of MXenes as additives in the perovskite absorber layers in PSCs [The letter “C” in the bracket stands for the control (reference or pristine) device)]

Device structure	V_{oc} [V]	J_{sc} [mA cm ⁻²]	FF [%]	PCE [%]	Refs.
ITO/SnO ₂ /MAPbI ₃ /Spiro-OMeTAD/Au (C)	1.00	20.67	75	15.58	[31]
ITO/SnO ₂ /MAPbI ₃ :Ti ₃ C ₂ T _x /Spiro-OMeTAD/Au	1.03	22.26	76	17.41	
ITO/PTAA/CsPbI ₃ /CPTA/BCP/Ag (C)	1.18	19.05	80.33	18.05	[88]
ITO/PTAA/CsPbI ₃ /O-Ti ₃ C ₂ T _x -CsPbI ₃ /CPTA/BCP/Ag	1.21	19.85	81.61	19.69	
FTO/SnO ₂ -TiO _x Cl _{4-2x} /CsPbBr ₃ :Ti ₃ C ₂ Cl _x /Ti ₃ C ₂ Cl _x /Carbon (C)	1.59	7.32	79.9	9.18	[90]
FTO/SnO ₂ -TiO _x Cl _{4-2x} /CsPbBr ₃ :Ti ₃ C ₂ Cl _x /Ti ₃ C ₂ Cl _x /Carbon	1.702	7.87	82.7	11.08	
ITO/NiO/MAPbI ₃ /PCBM/BCP/Ag (C)	1.09	21.41	77	17.97	[91]
ITO/NiO/MAPbI ₃ + Ti ₃ C ₂ T _x /PCBM/BCP/Ag	1.08	22.33	77	18.57	
ITO/SnO ₂ /(BA) ₂ (MA) ₄ Pb ₅ I ₆ /Spiro-OMeTAD/Ag (C)	1.09	18.84	66.70	13.69	[96]
ITO/SnO ₂ /(BA) ₂ (MA) ₄ Pb ₅ I ₆ -Ti ₃ C ₂ T _x /Spiro-OMeTAD/Ag	1.11	20.87	67.84	15.71	
ITO/SnO ₂ /FA _{1-x} MA _x PbI _{3-y} Br _y /Spiro-OMeTAD/Au (C)	1.07	25.02	71	19.03	[97]
ITO/SnO ₂ /FA _{1-x} MA _x PbI _{3-y} Br _y :Cs-Ti ₃ C ₂ T _x /Spiro-OMeTAD/Au	1.10	26	76	21.57	
FTO/SnO ₂ /Rb _{0.05} Cs _{0.05} (FA _{0.83} MA _{0.17}) _{0.90} Pb(I _{0.83} Br _{0.17}) ₃ /Spiro-OMeTAD/Au (C)	1.14	21.16	77.85	18.78	[98]
FTO/SnO ₂ /Rb _{0.05} Cs _{0.05} (FA _{0.83} MA _{0.17}) _{0.90} Pb(I _{0.83} Br _{0.17}) ₃ :Ti ₃ C ₂ T _x QDs/Spiro-OMeTAD/Au	1.19	22.27	80.42	21.31	
FTO/SnO ₂ /MAPbI ₃ /Spiro-MeOTAD/Au (C)	1.08	21.53	70.47	16.45	[106]
FTO/SnO ₂ /MAPbI ₃ :Ti ₃ C ₂ T _x /Spiro-MeOTAD/Au	1.12	23.48	73.66	19.27	
FTO/c-TiO ₂ /m-TiO ₂ /D-149-Cs ₂ AgBiBr ₆ /Spiro-OMeTAD/Ag (C)	0.716	8.20	69.1	4.06	[107]
FTO/c-TiO ₂ /m-TiO ₂ /D149-Cs ₂ AgBiBr ₆ @Ti ₃ C ₂ T _x /Spiro-OMeTAD/Ag	0.722	8.85	70.1	4.47	
FTO/c-TiO ₂ /m-TiO ₂ /m-ZrO ₂ /MAPbI ₃ /Carbon (C)	0.80	23.03	61.81	11.35	[108]
FTO/c-TiO ₂ /m-TiO ₂ /m-ZrO ₂ /MAPbI ₃ :Ti ₃ C ₂ T _x /Carbon	0.81	17.64	61.12	13.62	
ITO/PTAA/MAPbI ₃ /PCBM:BCP/Ag (C)	1.00	20.60	73.20	15.01	[110]
ITO/PTAA/MAPbI ₃ :V ₂ CT _x /PCBM:BCP/Ag	1.03	23.12	73.90	17.61	
ITO/P-Nb ₂ CT _x /FA _{0.85} Cs _{0.15} PbI ₃ /Spiro-OMeTAD/Ag (C)	1.054	23.82	71.49	17.95	[112]
ITO/T-Nb ₂ CT _x /FA _{0.85} Cs _{0.15} PbI ₃ :T-Nb ₂ CT _x /Spiro-OMeTAD/Ag	1.124	25.07	77.36	21.79	
FTO/c-TiO ₂ /m-TiO ₂ /CsFAMAIr perovskite/Spiro-OMeTAD/Au (C)	1.10	23.11	71.83	18.3	[180]
FTO/c-TiO ₂ /m-TiO ₂ /Ti ₃ C ₂ T _x QD/Ti ₃ C ₂ T _x QD + CsFAMAIr perovskite/Spiro-OMeTAD/Au	1.12	23.51	74.62	20.72	

alignment on the photovoltaic parameters of MXene-based PSCs. In addition, different new synthesis routes and post-treatments such as laser irradiation, UV-ozone treatment, etc. need to be explored to obtain high quality pure and functionalized MXenes. MXenes should be transparent in the photovoltaic response range of PSCs in addition to having strong flexibility and high electrical conductivity. In addition, the benefits that MXenes provide in terms of material characteristics and performance should ensure affordable price, environmental compatibility, long-term stability, and sustainable manufacturing in upscaling the production of MXene and its commercial uses in PSCs (small size and large size) and solar cell modules [192]. Furthermore, the additional cost due to MXenes inclusion in PSCs needs to be evaluated. As a next step, a plethora of unexplored MXenes materials needs to be studied and

optoelectronic properties are to be optimized to improve both PCE and stability of PSCs further. Apart from PSCs, the MXenes have drawn interest in other perovskite-based optoelectronic devices such as photodetectors, photodiodes, phototransistors, and plasmonic, etc. [193]. MXenes are used in photodetectors (PDs) in various roles, such as transparent electrodes, Schottky contacts, light absorbers, and plasmonic materials [194]. Ti₃C₂T_x quantum dots (TQDs) are used to boost the charge carriers of 2D perovskite Ca₂Nb₃O₁₀ (CNO) nanosheets (NS) and enhance the performance of the TQD-modified 2D perovskite CNO NS PD. Other such examples are CsPbBr₃ NSs/Ti₃C₂T_x MXene and CsPbBr₃ NCs/Ti₃C₂T_x MXenes nanocomposite PDs [195]. Similarly, plasmonic Nb₂CT_x MXene-MAPbI₃ heterostructure is reported for self-powered visible-NIR photodiodes [196].

Table 2 Role of MXenes as ETL/ additives in ETL in PSCs [The letter “C” in the bracket stands for the control (reference or pristine) device)]

Device structure	V_{oc} [V]	J_{sc} [mA cm ⁻²]	FF [%]	PCE [%]	Refs.
ITO/NiO/MAPbI ₃ /PCBM/BCP/Ag (C)	1.09	21.41	77	17.97	[91]
ITO/NiO/Ti ₃ C ₂ T _x doped- MAPbI ₃ /MXene-PCBM/BCP/Ag	1.09	22.88	77	19.20	
FTO/SnO ₂ /(FAPbI ₃) _{0.97} (MAPbBr ₃) _{0.03} /Spiro-OMeTAD (C)	1.07	21.88	71.90	16.83	[120]
FTO/MDCN air & N ₂ /(FAPbI ₃) _{0.97} (MAPbBr ₃) _{0.03} /Spiro-OMeTAD	1.10	24.16	74.05	19.14	
ITO/SnO ₂ /MA _{0.15} FA _{0.85} PbI _x Br _(3-x) /Spiro-OMeTAD/Ag (C)	1.111	20.65	70.99	16.28	[121]
ITO/SnO ₂ /Ti ₃ C ₂ T _x /MA _{0.15} FA _{0.85} PbI _x Br _(3-x) /Spiro-OMeTAD/Ag	1.113	23.65	76.01	20.35	
FTO/TiO ₂ /Cs ₂ AgBiBr ₆ /Spiro-OMeTAD /MoO ₃ /Ag (C)	0.93	3.29	65	2.00	[122]
FTO/Ti ₃ C ₂ T _x @TiO ₂ (0.2 wt%)/Cs ₂ AgBiBr ₆ /Spiro-OMeTAD /MoO ₃ /Ag	0.96	4.14	70	2.81	
ITO/NiO _x /MAPbI ₃ /PC ₆₁ BM/BCP/Ag (C)*	1.04	21.53	72	15.55	[123]
ITO/NiO _x /MAPbI ₃ /Ti ₃ C ₂ T _x -PC ₆₁ BM/ BCP/Ag*	1.06	22.90	77	18.37	
ITO/NiO _x /MAPbI ₃ /Ti ₃ C ₂ T _x /BCP/Ag*	0.72	5.47	50	2.01	
FTO/SnO ₂ /MAPbI ₃ /Spiro-OMeTAD/Ag (C)	1.06	23.04	72.88	17.78	[124]
FTO/SnO ₂ -Ti ₃ C ₂ MXene/MAPbI ₃ /Spiro-OMeTAD/Ag	1.07	23.44	75.86	18.84	
ITO/MAPbI ₃ /Spiro-OMeTAD/Ag (C)	0.80	15.87	40	5	[111]
ITO/Ti ₃ C ₂ T _x /MAPbI ₃ /Spiro-OMeTAD/Ag	1.08	22.63	70	17.17	
ITO/SnO ₂ /CsFAMAIr perovskite/Spiro-OMeTAD/Ag (C)	1.111	24.71	69.1	18.96	[125]
ITO/SnO ₂ -Nb ₂ C/CsFAMAIr perovskite/Spiro-OMeTAD/Ag	1.138	25.29	79.5	22.86	
ITO/P-Nb ₂ CT _x /FA _{0.85} Cs _{0.15} PbI ₃ /Spiro-OMeTAD/Ag (C)	1.054	23.82	71.49	17.95	[112]
ITO/T-Nb ₂ CT _x /FA _{0.85} Cs _{0.15} PbI ₃ /Spiro-OMeTAD/Ag	1.117	24.55	73.79	20.23	
TO/T-Nb ₂ CT _x /FA _{0.85} Cs _{0.15} PbI ₃ + T-Nb ₂ CT _x /Spiro-OMeTAD/Ag	1.124	25.07	77.36	21.79	
FTO/TiO ₂ :SnO ₂ :Ti ₃ C ₂ T _x /(FAPbI ₃) _{0.97} (MAPbBr ₃) _{0.03} /Spiro-OMeTAD/Au	1.10	22.03	77.78	18.9	[113]
ITO/SnO ₂ /FAPbI ₃ /Spiro-OMeTAD/MoO _x /Ag (C)	1.093	25.22	81.11	22.36	[126]
ITO/Ti ₃ C ₂ T _x -H-doped SnO ₂ /FAPbI ₃ /Spiro-OMeTAD/MoO _x /Ag	1.121	25.49	84.42	24.12	
ITO/SnO ₂ /FA _{0.9} MA _{0.05} Cs _{0.05} PbI _{0.98} Br _{0.02} /Spiro-MeOTAD/MoO ₃ /Au (C)	1.140	24.26	75.8	20.96	[127]
ITO/SnO ₂ -Ti ₃ C ₂ T _x QDs/FA _{0.9} MA _{0.05} Cs _{0.05} PbI _{0.98} Br _{0.02} /Spiro-MeOTAD /MoO ₃ /Au	1.172	24.96	79.8	23.34	
ITO/MAPbI ₃ /Spiro-OMeTAD/Ag (C)	1.03	20.61	70	14.86	[114]
ITO/HO-Ti ₃ C ₂ T _x @Ti ₃ C ₂ T _x /MAPbI ₃ /Spiro-OMeTAD/Ag	1.07	23.11	74	18.29	
FTO/c-TiO ₂ : Ti ₃ C ₂ T _x /m-TiO ₂ :Ti ₃ C ₂ T _x /Ti ₃ C ₂ T _x /MAPbI ₃ :Ti ₃ C ₂ T _x /Spiro-OMeTAD/Au	1.09	23.82	77.6	20.14	[179]
FTO/c-TiO ₂ /m-TiO ₂ /Ti ₃ C ₂ T _x QD/CsFAMAIr perovskite/Spiro-OMeTAD/Au	1.12	23.51	74.62	19.65	[180]

The sign“*” represents the maximum values of the photovoltaic parameters

Table 3 Role of MXenes as HTL/ additives in HTL in PSCs [The letter “C” in the bracket stands for the control (reference or pristine) device)]

Device structure	V_{oc} [V]	J_{sc} [mA cm ⁻²]	FF [%]	PCE [%]	Refs.
ITO/MAPbI ₃ /PCBM/Ag (C)	1.047	20.16	73.57	15.53	[134]
ITO/Nb ₂ CT _x /MAPbI ₃ /PCBM/Ag	1.128	23.06	79.75	20.74	
ITO/ Ti ₃ C ₂ T _x -SCA/MAPbI ₃ /PC ₆₁ BM/Ag	0.87	21.30	73.47	13.65	[139]
ITO/PEDOT:PSS/MAPbI ₃ /PCBM/LiF/Al (C)	0.884	18.145	59	9.28	[153]
ITO/Mo ₂ C-CNT@PEDOT:PSS/MAPbI ₃ /PCBM/LiF/Al*	0.881	22.219	62	12.14	
ITO/PEDOT:PSS/MAPbI ₃ /PCBM/LiF/Al (C)	0.904	18.59	56.73	9.31	[154]
ITO/Ti ₃ C ₂ T _x /WO ₃ @PEDOT:PSS/MAPbI ₃ /PCBM/LiF/Al*	0.924	22.73	60.71	12.38	

The sign“*” represents the maximum values of the photovoltaic parameters

In recent years, perovskite solar cells have undergone significant scientific developments. Low-cost, low-temperature solution-based fabrication processes, advances

in multi-cation and -anion perovskites, improvements in all-inorganic perovskites, Pb-free perovskites, application of 2D/3D perovskites, defects passivation via solvent

Table 4 Role of MXenes as electrodes in PSCs [The letter “C” in the bracket stands for the control (reference or pristine) device]]

Device structure	V_{oc} [V]	J_{sc} [mA cm ⁻²]	FF [%]	PCE [%]	Refs.
FTO/TiO ₂ /MAPbI ₃ /Coal (C)	0.84	21.39	60	10.87	[157]
FTO/TiO ₂ /MAPbI ₃ /Ti ₃ C ₂ T _x	0.95	22.96	63	13.83	
FTO/c-TiO ₂ /CsPbBr ₃ /Carbon + CNTs (C)	1.250	5.81	65.68	4.77	[161]
FTO/c-TiO ₂ /CsPbBr ₃ /Carbon + CNTs + Ti ₃ C ₂ -MXene	1.357	7.16	72.97	7.09	
PET/AgNW:Ti ₃ C ₂ T _x /NiO _x /Cs _{0.05} FA _{0.85} MA _{0.10} Pb(I _{0.97} Br _{0.03}) ₃ /PC ₆₁ BM/Ag	1.06	25.16	75.52	20.22	[176]

Table 5 Role of MXenes as interfacial layers in PSCs [the letter “C” in the bracket stands for the control (reference or pristine) device]

Device structure	V_{oc} [V]	J_{sc} [mA cm ⁻²]	FF [%]	PCE [%]	Refs.
FTO/SnO ₂ -TiO _x Cl _{4-2x} /CsPbBr ₃ :Ti ₃ C ₂ Cl _x /Ti ₃ C ₂ Cl _x /Carbon	1.702	7.87	82.7	11.08	[90]
ITO/NiO _x /MAPbI ₃ /Ti ₃ C ₂ T _x /PC ₆₁ BM/BCP/Ag*	1.05	20.74	74	15.99	[123]
FTO/TiO ₂ /CsPbBr ₃ /Carbon (C)	1.387	7.10	72.18	7.11	[160]
FTO/TiO ₂ /CsPbBr ₃ /Ti ₃ C ₂ MXene/Carbon	1.444	8.54	73.08	9.01	
FTO/c-TiO ₂ :Ti ₃ C ₂ T _x /m-TiO ₂ :Ti ₃ C ₂ T _x /Ti ₃ C ₂ T _x /MAPbI ₃ :Ti ₃ C ₂ T _x /Spiro-OMeTAD/Au	1.09	23.82	77.6	20.14	[179]
ITO/SnO ₂ /FA _x MA _{1-x} I _{3-y} Br _y /Spiro-OMeTAD/Au (C)	1.043	24.71	73	18.84	[181]
ITO/SnO ₂ /Ti ₃ C ₂ T _x :m-SWCNT/FA _x MA _{1-x} I _{3-y} Br _{3-y} /Spiro-OMeTAD/Au	1.073	25.09	80	21.42	
ITO/SnO ₂ /CsFAMAIBr perovskite/Spiro-OMeTAD/Au (C)	1.09	24.16	75.18	20.03	[182]
ITO/SnO ₂ -MXene/CsFAMAIBr perovskite/Spiro-OMeTAD/Au	1.13	25.07	81.1	23.07	
FTO/SnO ₂ /Nb ₂ CT _x /CsFAMAIBr perovskite/Spiro-OMeTAD/Au	1.187	22.87	76.84	20.86	[183]
FTO/SnO ₂ /Au@Nb ₂ CT _x /CsFAMAIBr perovskite/Spiro-OMeTAD/Au	1.215	24.28	80.62	23.78	
FTO/SnO ₂ /CsPbI ₃ /Spiro-OMeTAD/Au (C)	1.15	20.02	79.68	18.39	[185]
FTO/SnO ₂ /CsPbI ₃ /Flourine-functionalized Ti ₃ C ₂ T _x QDs/Spiro-OMeTAD/Au (C)	1.22	20.59	81.55	20.44	
FTO/TiO ₂ /FAPbI ₃ /Spiro-OMeTAD/Au (C)	1.102	25.30	79.81	22.25	[186]
FTO/TiO ₂ /FAPbI ₃ /nano-Ti ₃ C ₂ F _x /Spiro-OMeTAD/Au	1.132	25.84	82.63	24.17	
FTO/Ti ₃ C ₂ T _x /SnO ₂ /Cs _{0.05} FA _{0.76} MA _{0.19} PbI _{2.715} Br _{0.285} /Spiro-OMeTAD/Au	1.11	24.34	76.4	20.65	[190]
FTO/SnO ₂ /MAPbI ₃ /Spiro-OMeTAD/Ag (C)	1.046	23.22	72.8	17.68	[191]
FTO/O-Ti ₃ C ₂ T _x /SnO ₂ /MAPbI ₃ /Spiro-OMeTAD/Ag	1.075	23.88	74.8	20.09	

The sign“*” represents the maximum values of the photovoltaic parameters

engineering, compositional engineering, interface engineering, device engineering, consistent improvements in the photovoltaic performance (PCE and stability) of tandem solar cells, solar concentrators incorporating scattering effects and spectral modification, and flexibility of perovskite solar cells hold the promise for scalability and large-scale commercialization of PSCs with high performance-to-cost ratios. In this review article, we have succinctly analyzed the incorporation of 2D MXene materials into the perovskite absorber layer, ETL/HTL, electrode, and interfaces. High optical transparency, wide tunable work function via functionalization of surface terminal groups, flexibility and superior mechanical properties of

MXenes and their optimum concentrations are the key factors in producing high quality and uniform films, reducing trap states density and improving charge carrier extraction and collection capabilities in PSCs. These features present MXenes as tremendous potential candidates for PSC applications. This review highlights the recent advances of MXenes in PSCs that is simply a fractional part, and many key improvements in the MXene-modified PSCs are about to come in the near future.

Acknowledgements This research was supported by the National Research Foundation of Korea (NRF) grant funded by the Korean government (MSIT) (No. 2022M3J7A1062940 and 2022033777) and supported by Korea Electric Power Corporation (Grant Number: R21XO01-5). This work was supported by the Technology Innovation Program (or Industrial Strategic Technology

Development Program) (1415172732/20011410, Development of SPD smart film and service of aftermarket for energy saving in building and automobiles) funded By the Ministry of Trade, Industry & Energy (MOTIE, Korea). This research was also supported by Basic Science Research Program through the National Research Foundation of Korea (NRF) funded by the Ministry of Education (2018R1A6A1A03023788 and 2021R111A1A01055790).

Funding Open access funding provided by Shanghai Jiao Tong University.

Open Access This article is licensed under a Creative Commons Attribution 4.0 International License, which permits use, sharing, adaptation, distribution and reproduction in any medium or format, as long as you give appropriate credit to the original author(s) and the source, provide a link to the Creative Commons licence, and indicate if changes were made. The images or other third party material in this article are included in the article's Creative Commons licence, unless indicated otherwise in a credit line to the material. If material is not included in the article's Creative Commons licence and your intended use is not permitted by statutory regulation or exceeds the permitted use, you will need to obtain permission directly from the copyright holder. To view a copy of this licence, visit <http://creativecommons.org/licenses/by/4.0/>.

References

- H. Min, D.Y. Lee, J. Kim, G. Kim, K.S. Lee et al., Perovskite solar cells with atomically coherent interlayers on SnO₂ electrodes. *Nature* **598**(7881), 444–450 (2021). <https://doi.org/10.1038/s41586-021-03964-8>
- W.E.I. Sha, X. Ren, L. Chen, W.C.H. Choy, The efficiency limit of CH₃NH₃PbI₃ perovskite solar cells. *Appl. Phys. Lett.* **106**(22), 221104 (2015). <https://doi.org/10.1063/1.4922150>
- G. Nazir, S.Y. Lee, J.H. Lee, A. Rehman, J.K. Lee et al., Stabilization of perovskite solar cells: recent developments and future perspectives. *Adv. Mater.* **34**(50), 2204380 (2022). <https://doi.org/10.1002/adma.202204380>
- K. Wang, L. Zheng, Y. Hou, A. Nozariasbmarz, B. Poudel et al., Overcoming shockley-queisser limit using halide perovskite platform? *Joule* **6**(4), 756–771 (2022). <https://doi.org/10.1016/j.joule.2022.01.009>
- P. Wang, Y. Wu, B. Cai, Q. Ma, X. Zheng et al., Solution-processable perovskite solar cells toward commercialization: progress and challenges. *Adv. Funct. Mater.* **29**(47), 1807661 (2019). <https://doi.org/10.1002/adfm.201807661>
- W. Nie, H. Tsai, R. Asadpour, J.-C. Blancon, A.J. Neukirch et al., High-efficiency solution-processed perovskite solar cells with millimeter-scale grains. *Science* **347**(6221), 522–525 (2015). <https://doi.org/10.1126/science.aaa0472>
- H.J. Snaith, Present status and future prospects of perovskite photovoltaics. *Nat. Mater.* **17**(5), 372–376 (2018). <https://doi.org/10.1038/s41563-018-0071-z>
- N.J. Jeon, J.H. Noh, W.S. Yang, Y.C. Kim, S. Ryu et al., Compositional engineering of perovskite materials for high-performance solar cells. *Nature* **517**(7535), 476–480 (2015). <https://doi.org/10.1038/nature14133>
- D. Bi, C. Yi, J. Luo, J.-D. Décoppet, F. Zhang et al., Polymer-templated nucleation and crystal growth of perovskite films for solar cells with efficiency greater than 21%. *Nat. Energy* **1**(10), 16142 (2016). <https://doi.org/10.1038/nenergy.2016.142>
- Q. Jiang, L. Zhang, H. Wang, X. Yang, J. Meng et al., Enhanced electron extraction using SnO₂ for high-efficiency planar-structure HC(NH₂)₂PbI₃-based perovskite solar cells. *Nat. Energy* **2**(1), 16177 (2016). <https://doi.org/10.1038/nenergy.2016.177>
- Q. Jiang, Y. Zhao, X. Zhang, X. Yang, Y. Chen et al., Surface passivation of perovskite film for efficient solar cells. *Nat. Photon.* **13**(7), 460–466 (2019). <https://doi.org/10.1038/s41566-019-0398-2>
- R. Azmi, E. Ugur, A. Seitekhan, F. Aljamaan, A.S. Subbiah et al., Damp heat-stable perovskite solar cells with tailored-dimensionality 2d/3d heterojunctions. *Science* **376**(6588), 73–77 (2022). <https://doi.org/10.1126/science.abm5784>
- S. Riaz, S.-J. Park, Thioacetamide-derived nitrogen and sulfur co-doped carbon quantum dots for “green” quantum dot solar cells. *J. Ind. Eng. Chem.* **105**, 111–120 (2022). <https://doi.org/10.1016/j.jiec.2021.09.009>
- B. Anasori, M.R. Lukatskaya, Y. Gogotsi, 2d metal carbides and nitrides (MXenes) for energy storage. *Nat. Rev. Mater.* **2**(2), 16098 (2017). <https://doi.org/10.1038/natrevmats.2016.98>
- X. Fan, Y. Ding, Y. Liu, J. Liang, Y. Chen, Plasmonic Ti₃C₂T_x MXene enables highly efficient photothermal conversion for healable and transparent wearable device. *ACS Nano* **13**(7), 8124–8134 (2019). <https://doi.org/10.1021/acsnano.9b03161>
- Y. Sun, D. Jin, Y. Sun, X. Meng, Y. Gao et al., G-C₃N₄/Ti₃C₂T_x (MXenes) composite with oxidized surface groups for efficient photocatalytic hydrogen evolution. *J. Mater. Chem. A* **6**(19), 9124–9131 (2018). <https://doi.org/10.1039/C8TA02706D>
- Q. Tao, M. Dahllqvist, J. Lu, S. Kota, R. Meshkian et al., Two-dimensional Mo_{1.33}C MXene with divacancy ordering prepared from parent 3d laminate with in-plane chemical ordering. *Nat. Commun.* **8**(1), 14949 (2017). <https://doi.org/10.1038/ncomms14949>
- Y. Cai, J. Shen, G. Ge, Y. Zhang, W. Jin et al., Stretchable Ti₃C₂T_x MXene/carbon nanotube composite based strain sensor with ultrahigh sensitivity and tunable sensing range. *ACS Nano* **12**(1), 56–62 (2018). <https://doi.org/10.1021/acsnano.7b06251>
- Q. Xu, W. Yang, Y. Wen, S. Liu, Z. Liu et al., Hydrochromic full-color MXene quantum dots through hydrogen bonding toward ultrahigh-efficiency white light-emitting diodes. *Appl. Mater. Today* **16**, 90–101 (2019). <https://doi.org/10.1016/j.apmt.2019.05.001>



20. S. Ahn, T.-H. Han, K. Maleski, J. Song, Y.-H. Kim et al., A 2D titanium carbide MXene flexible electrode for high-efficiency light-emitting diodes. *Adv. Mater.* **32**(23), 2000919 (2020). <https://doi.org/10.1002/adma.202000919>
21. Z. Li, Z. Zhuang, F. Lv, H. Zhu, L. Zhou et al., The marriage of the FeN₄ moiety and mxene boosts oxygen reduction catalysis: Fe 3d electron delocalization matters. *Adv. Mater.* **30**(43), 1803220 (2018). <https://doi.org/10.1002/adma.201803220>
22. J.-H. Lee, G. Yang, C.-H. Kim, R.L. Mahajan, S.-Y. Lee et al., Flexible solid-state hybrid supercapacitors for the internet of everything (IOE). *Energy Environ. Sci.* **15**(6), 2233–2258 (2022). <https://doi.org/10.1039/D1EE03567C>
23. M. Hadadian, J.-P. Correa-Baena, E.K. Goharshadi, A. Ummadisingu, J.-Y. Seo et al., Enhancing efficiency of perovskite solar cells via n-doped graphene: crystal modification and surface passivation. *Adv. Mater.* **28**(39), 8681–8686 (2016). <https://doi.org/10.1002/adma.201602785>
24. L.-L. Jiang, Z.-K. Wang, M. Li, C.-C. Zhang, Q.-Q. Ye et al., Passivated perovskite crystallization via g-C₃N₄ for high-performance solar cells. *Adv. Funct. Mater.* **28**(7), 1705875 (2018). <https://doi.org/10.1002/adfm.201705875>
25. C. Ma, Y. Shi, W. Hu, M.-H. Chiu, Z. Liu et al., Heterostructured WS₂/CH₃NH₃PbI₃ photoconductors with suppressed dark current and enhanced photodetectivity. *Adv. Mater.* **28**(19), 3683–3689 (2016). <https://doi.org/10.1002/adma.201600069>
26. A. Capasso, F. Matteocci, L. Najafi, M. Prato, J. Buha et al., Few-layer MoS₂ flakes as active buffer layer for stable perovskite solar cells. *Adv. Energy Mater.* **6**(16), 1600920 (2016). <https://doi.org/10.1002/aenm.201600920>
27. J.-H. Lee, Y.-S. Kim, H.-J. Ru, S.-Y. Lee, S.-J. Park, Highly flexible fabrics/epoxy composites with hybrid carbon nanofillers for absorption-dominated electromagnetic interference shielding. *Nano-Micro Lett.* **14**(1), 188 (2022). <https://doi.org/10.1007/s40820-022-00926-1>
28. W. Chen, K. Li, Y. Wang, X. Feng, Z. Liao et al., Black phosphorus quantum dots for hole extraction of typical planar hybrid perovskite solar cells. *J. Phys. Chem. Lett.* **8**(3), 591–598 (2017). <https://doi.org/10.1021/acs.jpcclett.6b02843>
29. A.D. Dillon, M.J. Ghidui, A.L. Krick, J. Griggs, S.J. May et al., Highly conductive optical quality solution-processed films of 2d titanium carbide. *Adv. Funct. Mater.* **26**(23), 4162–4168 (2016). <https://doi.org/10.1002/adfm.201600357>
30. Y. Dall'Agnese, M.R. Lukatskaya, K.M. Cook, P.-L. Taberna, Y. Gogotsi et al., High capacitance of surface-modified 2d titanium carbide in acidic electrolyte. *Electrochem. Commun.* **48**, 118–122 (2014). <https://doi.org/10.1016/j.elecom.2014.09.002>
31. Z. Guo, L. Gao, Z. Xu, S. Teo, C. Zhang, Communications High electrical conductivity 2d mxene serves as additive of perovskite for efficient solar cells. *Small* **14**(47), 1802738 (2018). <https://doi.org/10.1002/sml.201802738>
32. G. Murali, J. Rawal, J.K.R. Modigunta, Y.H. Park, J.-H. Lee et al., A review on MXenes: new-generation 2D materials for supercapacitors. *Sustain. Energy Fuels* **5**(22), 5672–5693 (2021). <https://doi.org/10.1039/D1SE00918D>
33. G. Murali, J.K. Reddy Modigunta, Y.H. Park, J.-H. Lee, J. Rawal et al., A review on MXene synthesis, stability, and photocatalytic applications. *ACS Nano* **16**, 13370–13429 (2022). <https://doi.org/10.1021/acsnano.2c04750>
34. S.-J. Park, H.-C. Kim, H.-Y. Kim, Roles of work of adhesion between carbon blacks and thermoplastic polymers on electrical properties of composites. *J. Colloid Interface Sci.* **255**(1), 145–149 (2002). <https://doi.org/10.1006/jcis.2002.8481>
35. M. Naguib, M. Kurtoglu, V. Presser, J. Lu, J. Niu et al., Two-dimensional nanocrystals produced by exfoliation of Ti₃AlC₂. *Adv. Mater.* **23**(37), 4248–4253 (2011). <https://doi.org/10.1002/adma.201102306>
36. A. VahidMohammadi, J. Rosen, Y. Gogotsi, The world of two-dimensional carbides and nitrides (MXenes). *Science* **372**(6547), eabf1581 (2021). <https://doi.org/10.1126/science.abf1581>
37. J. Halim, S. Kota, M.R. Lukatskaya, M. Naguib, M.-Q. Zhao et al., Synthesis and characterization of 2d molybdenum carbide (MXene). *Adv. Funct. Mater.* **26**(18), 3118–3127 (2016). <https://doi.org/10.1002/adfm.201505328>
38. J. Zhou, X. Zha, F.Y. Chen, Q. Ye, P. Eklund et al., A two-dimensional zirconium carbide by selective etching of Al₃C₃ from nanolaminated Zr₃Al₃C₅. *Angew. Chem. Int. Ed.* **55**(16), 5008–5013 (2016). <https://doi.org/10.1002/anie.201510432>
39. R. Khaledialidusti, M. Khazaei, S. Khazaei, K. Ohno, High-throughput computational discovery of ternary-layered max phases and prediction of their exfoliation for formation of 2D MXenes. *Nanoscale* **13**(15), 7294–7307 (2021). <https://doi.org/10.1039/D0NR08791B>
40. L. Gao, C. Li, W. Huang, S. Mei, H. Lin et al., MXene/polymer membranes: synthesis, properties, and emerging applications. *Chem. Mater.* **32**(5), 1703–1747 (2020). <https://doi.org/10.1021/acs.chemmater.9b04408>
41. C.A. Voigt, M. Ghidui, V. Natu, M.W. Barsoum, Anion adsorption, Ti₃C₂Tz MXene multilayers, and their effect on claylike swelling. *J. Phys. Chem. C* **122**(40), 23172–23179 (2018). <https://doi.org/10.1021/acs.jpcc.8b07447>
42. C.E. Shuck, A. Sarycheva, M. Anayee, A. Levitt, Y. Zhu et al., Scalable synthesis of Ti₃C₂Tx mxene. *Adv. Engin. Mater.* **22**(3), 1901241 (2020). <https://doi.org/10.1002/adem.201901241>
43. J. Halim, M.R. Lukatskaya, K.M. Cook, J. Lu, C.R. Smith et al., Transparent conductive two-dimensional titanium carbide epitaxial thin films. *Chem. Mat.* **26**, 2374–2381 (2014). <https://doi.org/10.1021/cm500641a>
44. M. Alhabeib, K. Maleski, T.S. Mathis, A. Sarycheva, C.B. Hatter et al., Selective etching of silicon from Ti₃SiC₂ (MAX) to obtain 2D titanium carbide (MXene). *Angew. Chem. Int. Ed.* **57**(19), 5444–5448 (2018). <https://doi.org/10.1002/anie.201802232>
45. X. Wang, C. Garnero, G. Rochard, D. Magne, S. Morisset et al., A new etching environment (FeF₃/HCl) for the synthesis of two-dimensional titanium carbide mxenes: a route towards selective reactivity vs. water. *J. Mater. Chem. A*

- 5(41), 22012–22023 (2017). <https://doi.org/10.1039/C7TA01082F>
46. M. Ghidui, M.R. Lukatskaya, M.-Q. Zhao, Y. Gogotsi, M.W. Barsoum, Conductive two-dimensional titanium carbide ‘clay’ with high volumetric capacitance. *Nature* **516**(7529), 78–81 (2014). <https://doi.org/10.1038/nature13970>
47. M. Li, J. Lu, K. Luo, Y. Li, K. Chang et al., Element replacement approach by reaction with lewis acidic molten salts to synthesize nanolaminated max phases and MXenes. *J. Am. Chem. Soc.* **141**(11), 4730–4737 (2019). <https://doi.org/10.1021/jacs.9b00574>
48. Y. Li, H. Shao, Z. Lin, J. Lu, L. Liu et al., A general lewis acidic etching route for preparing mxenes with enhanced electrochemical performance in non-aqueous electrolyte. *Nat. Mater.* **19**(8), 894–899 (2020). <https://doi.org/10.1038/s41563-020-0657-0>
49. T. Li, L. Yao, Q. Liu, J. Gu, R. Luo et al., Fluorine-free synthesis of high-purity $Ti_3C_2T_x$ (T=OH, O) via alkali treatment. *Angew. Chem. Int. Ed.* **57**(21), 6115–6119 (2018). <https://doi.org/10.1002/anie.201800887>
50. X. Yu, X. Cai, H. Cui, S.-W. Lee, X.-F. Yu et al., Fluorine-free preparation of titanium carbide mxene quantum dots with high near-infrared photothermal performances for cancer therapy. *Nanoscale* **9**(45), 17859–17864 (2017). <https://doi.org/10.1039/C7NR05997C>
51. J. Xuan, Z. Wang, Y. Chen, D. Liang, L. Cheng et al., Organic-base-driven intercalation and delamination for the production of functionalized titanium carbide nanosheets with superior photothermal therapeutic performance. *Angew. Chem. Int. Ed.* **55**(47), 14569–14574 (2016). <https://doi.org/10.1002/anie.201606643>
52. V. Natu, R. Pai, M. Sokol, M. Carey, V. Kalra et al., 2D Ti_3C_2Tz MXene synthesized by water-free etching of Ti_3AlC_2 in polar organic solvents. *Chem* **6**(3), 616–630 (2020). <https://doi.org/10.1016/j.chempr.2020.01.019>
53. H. Shi, P. Zhang, Z. Liu, S. Park, M.R. Lohe et al., Ambient-stable two-dimensional titanium carbide (MXene) enabled by iodine etching. *Angew. Chem. Int. Ed.* **60**(16), 8689–8693 (2021). <https://doi.org/10.1002/anie.202015627>
54. A.E. Ghazaly, H. Ahmed, A.R. Rezk, J. Halim, P.O.Å. Persson et al., Ultrafast, one-step, salt-solution-based acoustic synthesis of Ti_3C_2 MXene. *ACS Nano* **15**(3), 4287–4293 (2021). <https://doi.org/10.1021/acsnano.0c07242>
55. W. Sun, S.A. Shah, Y. Chen, Z. Tan, H. Gao et al., Electrochemical etching of Ti_2AlC to Ti_2CT_x (MXene) in low-concentration hydrochloric acid solution. *J. Mater. Chem. A* **5**(41), 21663–21668 (2017). <https://doi.org/10.1039/C7TA05574A>
56. S.-Y. Pang, Y.-T. Wong, S. Yuan, Y. Liu, M.-K. Tsang et al., Universal strategy for Hf-free facile and rapid synthesis of two-dimensional MXenes as multifunctional energy material. *J. Am. Chem. Soc.* **141**(24), 9610–9616 (2019). <https://doi.org/10.1021/jacs.9b02578>
57. Y. Xie, P.R.C. Kent, Hybrid density functional study of structural and electronic properties of functionalized $Ti_{n+1}X_n$ (X=C, N) monolayers. *Phys. Rev. B* **87**(23), 235441 (2013). <https://doi.org/10.1103/PhysRevB.87.235441>
58. M. Khazaei, M. Arai, T. Sasaki, C.-Y. Chung, N.S. Venkataramanan et al., Novel electronic and magnetic properties of two-dimensional transition metal carbides and nitrides. *Adv. Funct. Mater.* **23**(17), 2185–2192 (2013). <https://doi.org/10.1002/adfm.201202502>
59. M. Khazaei, M. Arai, T. Sasaki, A. Ranjbar, Y. Liang et al., OH-terminated two-dimensional transition metal carbides and nitrides as ultralow work function materials. *Phys. Rev. B* **92**(7), 075411 (2015). <https://doi.org/10.1103/PhysRevB.92.075411>
60. H.A. Tahini, X. Tan, S.C. Smith, The origin of low workfunctions in oh terminated MXenes. *Nanoscale* **9**(21), 7016–7020 (2017). <https://doi.org/10.1039/C7NR01601H>
61. Y. Liu, H. Xiao, W.A. Goddard III., Schottky-barrier-free contacts with two-dimensional semiconductors by surface-engineered MXenes. *J. Am. Chem. Soc.* **138**(49), 15853–15856 (2016). <https://doi.org/10.1021/jacs.6b10834>
62. J. Lei, A. Kutana, B.I. Yakobson, Predicting stable phase monolayer Mo_2C (MXene), a superconductor with chemically-tunable critical temperature. *J. Mater. Chem. C* **5**(14), 3438–3444 (2017). <https://doi.org/10.1039/C7TC00789B>
63. Y. Liang, M. Khazaei, A. Ranjbar, M. Arai, S. Yunoki et al., Theoretical prediction of two-dimensional functionalized mxene nitrides as topological insulators. *Phys. Rev. B* **96**(19), 195414 (2017). <https://doi.org/10.1103/PhysRevB.96.195414>
64. M. Khazaei, A. Ranjbar, M. Arai, S. Yunoki, Topological insulators in the ordered double transition metals $M'_2M''C_2$ MXenes (M'=Mo, W; M''=Ti, Zr, Hf). *Phys. Rev. B* **94**(12), 125152 (2016). <https://doi.org/10.1103/PhysRevB.94.125152>
65. B. Anasori, C. Shi, E.J. Moon, Y. Xie, C.A. Voigt et al., Control of electronic properties of 2d carbides (MXenes) by manipulating their transition metal layers. *Nanoscale Horizons* **1**(3), 227–234 (2016). <https://doi.org/10.1039/C5NH00125K>
66. C. Si, J. Zhou, Z. Sun, Half-metallic ferromagnetism and surface functionalization-induced metal–insulator transition in graphene-like two-dimensional Cr_2C crystals. *ACS Appl. Mater. Interfaces* **7**(31), 17510–17515 (2015). <https://doi.org/10.1021/acsmi.5b05401>
67. I. Mathews, S. Sofia, E. Ma, J. Jean, H.S. Laine et al., Economically sustainable growth of perovskite photovoltaics manufacturing. *Joule* **4**(4), 822–839 (2020). <https://doi.org/10.1016/j.joule.2020.01.006>
68. L. Li, Y. Wang, X. Wang, R. Lin, X. Luo et al., Flexible all-perovskite tandem solar cells approaching 25% efficiency with molecule-bridged hole-selective contact. *Nat. Energy* **7**(8), 708–717 (2022). <https://doi.org/10.1038/s41560-022-01045-2>
69. L.A. Muscarella, E.M. Hutter, S. Sanchez, C.D. Dieleman, T.J. Savenije et al., Crystal orientation and grain size: do they determine optoelectronic properties of $MAPBi_3$ perovskite? *J. Phys. Chem. Lett.* **10**(20), 6010–6018 (2019). <https://doi.org/10.1021/acs.jpcllett.9b02757>



70. E. Ochoa-Martinez, M. Ochoa, R.D. Ortuso, P. Ferdowsi, R. Carron et al., Physical passivation of grain boundaries and defects in perovskite solar cells by an isolating thin polymer. *ACS Energy Lett.* **6**(7), 2626–2634 (2021). <https://doi.org/10.1021/acsenergylett.1c01187>
71. J.-P. Correa-Baena, M. Saliba, T. Buonassisi, M. Grätzel, A. Abate et al., Promises and challenges of perovskite solar cells. *Science* **358**(6364), 739–744 (2017). <https://doi.org/10.1126/science.aam6323>
72. J.Y. Kim, J.-W. Lee, H.S. Jung, H. Shin, N.-G. Park, High-efficiency perovskite solar cells. *Chem. Rev.* **120**(15), 7867–7918 (2020). <https://doi.org/10.1021/acs.chemrev.0c00107>
73. C. Pereyra, H. Xie, M. Lira-Cantu, Additive engineering for stable halide perovskite solar cells. *J. Energy Chem.* **60**, 599–634 (2021). <https://doi.org/10.1016/j.jechem.2021.01.037>
74. S. Palei, H. Kim, J.H. Seo, D. Singh, K. Seo, Stability and efficiency enhancement of perovskite solar cells using phenyltriethylammonium iodide. *Adv. Mater. Interfaces* **9**(16), 2200464 (2022). <https://doi.org/10.1002/admi.202200464>
75. T. Webb, S.J. Sweeney, W. Zhang, Device architecture engineering: progress toward next generation perovskite solar cells. *Adv. Funct. Mater.* **31**(35), 2103121 (2021). <https://doi.org/10.1002/adfm.202103121>
76. J. Li, R. Xia, W. Qi, X. Zhou, J. Cheng et al., Encapsulation of perovskite solar cells for enhanced stability: structures mater, and characterization. *J. Power Sources* **485**, 229313 (2021). <https://doi.org/10.1016/j.jpowsour.2020.229313>
77. W. Ke, M.G. Kanatzidis, Prospects for low-toxicity lead-free perovskite solar cells. *Nat. Commun.* **10**(1), 965 (2019). <https://doi.org/10.1038/s41467-019-08918-3>
78. P.-K. Kung, M.-H. Li, P.-Y. Lin, J.-Y. Jhang, M. Pantaler et al., Lead-free double perovskites for perovskite solar cells. *Solar RRL* **4**(2), 1900306 (2020). <https://doi.org/10.1002/solr.201900306>
79. J. Wang, J. Dong, F. Lu, C. Sun, Q. Zhang et al., Two-dimensional lead-free halide perovskite materials and devices. *J. Mater. Chem. A* **7**(41), 23563–23576 (2019). <https://doi.org/10.1039/C9TA06455A>
80. M. Wang, W. Wang, B. Ma, W. Shen, L. Liu et al., Lead-free perovskite materials for solar cells. *Nano-Micro Lett.* **13**(1), 62 (2021). <https://doi.org/10.1007/s40820-020-00578-z>
81. N.F. Montcada, M. Méndez, K.T. Cho, M.K. Nazeeruddin, E. Palomares, Photo-induced dynamic processes in perovskite solar cells: the influence of perovskite composition in the charge extraction and the carrier recombination. *Nanoscale* **10**(13), 6155–6158 (2018). <https://doi.org/10.1039/C8NR0180D>
82. A. Listorti, E.J. Juarez-Perez, C. Frontera, V. Roiati, L. Garcia-Andrade et al., Effect of mesostructured layer upon crystalline properties and device performance on perovskite solar cells. *J. Phys. Chem. Lett.* **6**(9), 1628–1637 (2015). <https://doi.org/10.1021/acs.jpcclett.5b00483>
83. H.S. Jung, N.-G. Park, Perovskite solar cells: from materials to devices. *Small* **11**(1), 10–25 (2015). <https://doi.org/10.1002/sml.201402767>
84. S.-S. Li, C.-H. Chang, Y.-C. Wang, C.-W. Lin, D.-Y. Wang et al., Intermixing-seeded growth for high-performance planar heterojunction perovskite solar cells assisted by precursor-capped nanoparticles. *Energy Environ. Sci.* **9**(4), 1282–1289 (2016). <https://doi.org/10.1039/C5EE03229F>
85. C. Lan, S. Zhao, C. Zhang, W. Liu, S. Hayase et al., Concentration gradient-controlled growth of large-grain $\text{CH}_3\text{NH}_3\text{PbI}_3$ films and enhanced photovoltaic performance of solar cells under ambient conditions. *CrystEngComm* **18**(48), 9243–9251 (2016). <https://doi.org/10.1039/C6CE02151D>
86. Z. Xiao, Q. Dong, C. Bi, Y. Shao, Y. Yuan et al., Solvent annealing of perovskite-induced crystal growth for photovoltaic-device efficiency enhancement. *Adv. Mater.* **26**(37), 6503–6509 (2014). <https://doi.org/10.1002/adma.201401685>
87. N. Tripathi, Y. Shirai, M. Yanagida, A. Karen, K. Miyano, Novel surface passivation technique for low-temperature solution-processed perovskite pv cells. *ACS Appl. Mater. Interfaces* **8**(7), 4644–4650 (2016). <https://doi.org/10.1021/acsami.5b11286>
88. J.H. Heo, F. Zhang, J.K. Park, H. Joon Lee, D.S. Lee et al., Surface engineering with oxidized $\text{Ti}_3\text{C}_2\text{Tx}$ MXene enables efficient and stable p-i-n-structured CsPbI_3 perovskite solar cells. *Joule* **6**(7), 1672–1688 (2022). <https://doi.org/10.1016/j.joule.2022.05.013>
89. L. Zhu, J. Shi, S. Lv, Y. Yang, X. Xu et al., Temperature-assisted controlling morphology and charge transport property for highly efficient perovskite solar cells. *Nano Energy* **15**, 540–548 (2015). <https://doi.org/10.1016/j.nanoen.2015.04.039>
90. Q. Zhou, J. Duan, J. Du, Q. Guo, Q. Zhang et al., Tailored lattice “tape” to confine tensile interface for 11.08%-efficiency all-inorganic CsPbBr_3 perovskite solar cell with an ultrahigh voltage of 1.702 V. *Adv. Sci.* **8**(19), 2101418 (2021). <https://doi.org/10.1002/advs.202101418>
91. D. Saranin, S. Pescetelli, A. Pazniak, D. Rossi, A. Liedl et al., Transition metal carbides (MXenes) for efficient NiO-based inverted perovskite solar cells. *Nano Energy* **82**, 105771 (2021). <https://doi.org/10.1016/j.nanoen.2021.105771>
92. P. Cheng, P. Wang, Z. Xu, X. Jia, Q. Wei et al., Ligand-size related dimensionality control in metal halide perovskites. *ACS Energy Lett.* **4**(8), 1830–1838 (2019). <https://doi.org/10.1021/acsenergylett.9b01100>
93. X. Xiao, J. Dai, Y. Fang, J. Zhao, X. Zheng et al., Suppressed ion migration along the in-plane direction in layered perovskites. *ACS Energy Lett.* **3**(3), 684–688 (2018). <https://doi.org/10.1021/acsenergylett.8b00047>
94. C. Ortiz-Cervantes, P. Carmona-Monroy, D. Solis-Ibarra, Two-dimensional halide perovskites in solar cells: 2D or not 2D? *Chemoschem* **12**(8), 1560–1575 (2019). <https://doi.org/10.1002/cssc.201802992>
95. H. Tsai, R. Asadpour, J.-C. Blancon, C.C. Stoumpos, J. Even et al., Design principles for electronic charge

- transport in solution-processed vertically stacked 2D perovskite quantum wells. *Nat. Commun.* **9**(1), 2130 (2018). <https://doi.org/10.1038/s41467-018-04430-2>
96. X. Jin, L. Yang, X.-F. Wang, Efficient two-dimensional perovskite solar cells realized by incorporation of $\text{Ti}_3\text{C}_2\text{T}_x$ MXene as nano-dopants. *Nano-Micro Lett.* **13**(1), 68 (2021). <https://doi.org/10.1007/s40820-021-00602-w>
97. A.S.R. Bati, A.A. Sutanto, M. Hao, M. Batmunkh, Y. Yamauchi et al., Cesium-doped $\text{Ti}_3\text{C}_2\text{T}_x$ MXene for efficient and thermally stable perovskite solar cells. *Cell Rep. Phys. Sci.* **2**(10), 100598 (2021). <https://doi.org/10.1016/j.xcrp.2021.100598>
98. X. Liu, Z. Zhang, J. Jiang, C. Tian, X. Wang et al., Chlorine-terminated mxene quantum dots for improving crystallinity and moisture stability in high-performance perovskite solar cells. *Chem. Eng. J.* **432**, 134382 (2022). <https://doi.org/10.1016/j.cej.2021.134382>
99. J.-H. Im, I.-H. Jang, N. Pellet, M. Grätzel, N.-G. Park, Growth of $\text{CH}_3\text{NH}_3\text{PbI}_3$ cuboids with controlled size for high-efficiency perovskite solar cells. *Nat. Nanotechnol.* **9**(11), 927–932 (2014). <https://doi.org/10.1038/nnano.2014.181>
100. J. Burschka, N. Pellet, S.-J. Moon, R. Humphry-Baker, P. Gao et al., Sequential deposition as a route to high-performance perovskite-sensitized solar cells. *Nature* **499**(7458), 316–319 (2013). <https://doi.org/10.1038/nature12340>
101. X. Zhang, H. Xiong, J. Qi, C. Hou, Y. Li et al., Antisolvent-derived intermediate phases for low-temperature flexible perovskite solar cells. *ACS Appl. Energ. Mater.* **1**(11), 6477–6486 (2018). <https://doi.org/10.1021/acsam.8b01413>
102. H.-S. Kim, C.-R. Lee, J.-H. Im, K.-B. Lee, T. Moehl et al., Lead iodide perovskite sensitized all-solid-state submicron thin film mesoscopic solar cell with efficiency exceeding 9%. *Sci. Rep.* **2**(1), 591 (2012). <https://doi.org/10.1038/srep00591>
103. J.-H. Im, H.-S. Kim, N.-G. Park, Morphology-photovoltaic property correlation in perovskite solar cells: one-step versus two-step deposition of $\text{CH}_3\text{NH}_3\text{PbI}_3$. *APL Mater.* **2**(8), 081510 (2014). <https://doi.org/10.1063/1.4891275>
104. D. Bi, S.-J. Moon, L. Häggman, G. Boschloo, L. Yang et al., Using a two-step deposition technique to prepare perovskite ($\text{CH}_3\text{NH}_3\text{PbI}_3$) for thin film solar cells based on ZrO_2 and TiO_2 mesostructures. *RSC Adv.* **3**(41), 18762–18766 (2013). <https://doi.org/10.1039/C3RA43228A>
105. J. Shi, Y. Luo, H. Wei, J. Luo, J. Dong et al., Modified two-step deposition method for high-efficiency $\text{TiO}_2/\text{CH}_3\text{NH}_3\text{PbI}_3$ heterojunction solar cells. *ACS Appl. Mater. Interfaces* **6**(12), 9711–9718 (2014). <https://doi.org/10.1021/am502131t>
106. Y. Zhao, X. Zhang, X. Han, C. Hou, H. Wang et al., Tuning the reactivity of PbI_2 film via monolayer $\text{Ti}_3\text{C}_2\text{T}_x$ mxene for two-step-processed $\text{CH}_3\text{NH}_3\text{PbI}_3$ solar cells. *Chem. Eng. J.* **417**, 127912 (2021). <https://doi.org/10.1016/j.cej.2020.127912>
107. L. Yang, P. Hou, B. Wang, C. Dall’Agnese, Y. Dall’Agnese et al., Performance improvement of dye-sensitized double perovskite solar cells by adding $\text{Ti}_3\text{C}_2\text{T}_x$ MXene. *Chem. Eng. J.* **446**, 136963 (2022). <https://doi.org/10.1016/j.cej.2022.136963>
108. S. Bykkam, A. Mishra, D.N. Prasad, M.R. Maurya, J.-J. Cabibihan et al., 2d-MXene as an additive to improve the power conversion efficiency of monolithic perovskite solar cells. *Mater. Lett.* **309**, 131353 (2022). <https://doi.org/10.1016/j.matlet.2021.131353>
109. M.F.U. Din, V. Held, S. Ullah, S. Sousani, M. Omastova et al., A synergistic effect of the ion beam sputtered ni ox hole transport layer and mxene doping on inverted perovskite solar cells. *Nanotechnology* **33**(42), 425202 (2022). <https://doi.org/10.1088/1361-6528/ac7ed4>
110. Y. Li, D. Wang, L. Yang, S. Yin, Preparation and performance of perovskite solar cells with two dimensional MXene as active layer additive. *J. Alloy Compd.* **904**, 163742 (2022). <https://doi.org/10.1016/j.jallcom.2022.163742>
111. L. Yang, C. Dall’Agnese, Y. Dall’Agnese, G. Chen, Y. Gao et al., Surface-modified metallic $\text{Ti}_3\text{C}_2\text{T}_x$ mxene as electron transport layer for planar heterojunction perovskite solar cells. *Adv. Funct. Mater.* **29**(46), 1905694 (2019). <https://doi.org/10.1002/adfm.201905694>
112. J. Zhang, C. Huang, Y. Sun, H. Yu, Amino-functionalized niobium-carbide mxene serving as electron transport layer and perovskite additive for the preparation of high-performance and stable methylammonium-free perovskite solar cells. *Adv. Funct. Mater.* **32**(24), 2113367 (2022). <https://doi.org/10.1002/adfm.202113367>
113. J. Wang, Z. Cai, D. Lin, K. Chen, L. Zhao et al., Plasma oxidized $\text{Ti}_3\text{C}_2\text{T}_x$ MXene as electron transport layer for efficient perovskite solar cells. *ACS Appl. Mater. Interfaces* **13**(27), 32495–32502 (2021). <https://doi.org/10.1021/acsami.1c07146>
114. L. Yang, D. Kan, C. Dall’Agnese, Y. Dall’Agnese, B. Wang et al., Performance improvement of MXene-based perovskite solar cells upon property transition from metallic to semiconductive by oxidation of $\text{Ti}_3\text{C}_2\text{T}_x$ in air. *J. Mater. Chem. A* **9**(8), 5016–5025 (2021). <https://doi.org/10.1039/D0TA11397B>
115. P. Wu, S. Wang, X. Li, F. Zhang, Advances in SnO_2 -based perovskite solar cells: from preparation to photovoltaic applications. *J. Mater. Chem. A* **9**(35), 19554–19588 (2021). <https://doi.org/10.1039/D1TA04130D>
116. W.-Q. Wu, D. Chen, Y.-B. Cheng, R.A. Caruso, Thin films of tin oxide nanosheets used as the electron transporting layer for improved performance and ambient stability of perovskite photovoltaics. *Solar RRL* **1**(11), 1700117 (2017). <https://doi.org/10.1002/solr.201700117>
117. L. Huang, X. Zhou, R. Wu, C. Shi, R. Xue et al., Oriented haloing metal-organic framework providing high efficiency and high moisture-resistance for perovskite solar cells. *J. Power Sources* **433**, 226699 (2019). <https://doi.org/10.1016/j.jpowsour.2019.226699>
118. B. Ding, S.-Y. Huang, Q.-Q. Chu, Y. Li, C.-X. Li et al., Low-temperature SnO_2 -modified TiO_2 yields record efficiency for normal planar perovskite solar modules. *J. Mater. Chem. A* **6**(22), 10233–10242 (2018). <https://doi.org/10.1039/C8TA01192C>



119. X. Huang, Z. Hu, J. Xu, P. Wang, L. Wang et al., Low-temperature processed SnO₂ compact layer by incorporating TiO₂ layer toward efficient planar heterojunction perovskite solar cells. *Solar Energy Mater. Solar Cells* **164**, 87–92 (2017). <https://doi.org/10.1016/j.solmat.2017.02.010>
120. L. Huang, X. Zhou, R. Xue, P. Xu, S. Wang et al., Low-temperature growing anatase TiO₂/SnO₂ multi-dimensional heterojunctions at mxene conductive network for high-efficient perovskite solar cells. *Nano-Micro Lett.* **12**(1), 44 (2020). <https://doi.org/10.1007/s40820-020-0379-5>
121. H. Zheng, Y. Wang, B. Niu, R. Ge, Y. Lei et al., Controlling the defect density of perovskite films by mxene/SnO₂ hybrid electron transport layers for efficient and stable photovoltaics. *J. Phys. Chem. C* **125**(28), 15210–15222 (2021). <https://doi.org/10.1021/acs.jpcc.1c04361>
122. Z. Li, P. Wang, C. Ma, F. Igbari, Y. Kang et al., Single-layered MXene nanosheets doping TiO₂ for efficient and stable double perovskite solar cells. *J. Am. Chem. Soc.* **143**(6), 2593–2600 (2021). <https://doi.org/10.1021/jacs.0c12739>
123. V.S.N. Chava, P.S. Chandrasekhar, A. Gomez, L. Echegoyen, S.T. Sreenivasan, Mxene-based tailoring of carrier dynamics, defect passivation, and interfacial band alignment for efficient planar p–i–n perovskite solar cells. *ACS Appl. Energy Mater.* **4**(11), 12137–12148 (2021). <https://doi.org/10.1021/acsaem.1c01669>
124. L. Yang, Y. Dall’Agnese, K. Hantanasirisakul, C.E. Shuck, K. Maleski et al., SnO₂–Ti₃C₂ MXene electron transport layers for perovskite solar cells. *J. Mater. Chem. A* **7**(10), 5635–5642 (2019). <https://doi.org/10.1039/C8TA12140K>
125. Y. Niu, C. Tian, J. Gao, F. Fan, Y. Zhang et al., Nb₂C MXenes modified SnO₂ as high quality electron transfer layer for efficient and stability perovskite solar cells. *Nano Energy* **89**, 106455 (2021). <https://doi.org/10.1016/j.nanoen.2021.106455>
126. L. Yin, C. Liu, C. Ding, C. Zhao, I.Z. Mitrovic et al., Functionalized-mxene-nanosheet-doped tin oxide enhances the electrical properties in perovskite solar cells. *Cell Rep. Phys. Sci.* **3**(6), 100905 (2022). <https://doi.org/10.1016/j.xcrp.2022.100905>
127. Y. Yang, H. Lu, S. Feng, L. Yang, H. Dong et al., Modulation of perovskite crystallization processes towards highly efficient and stable perovskite solar cells with MXene quantum dot-modified SnO₂. *Energy Environ. Sci.* **14**(6), 3447–3454 (2021). <https://doi.org/10.1039/D1EE00056J>
128. Z. Wang, D. Zhang, G. Yang, J. Yu, Exceeding 19% efficiency for inverted perovskite solar cells used conventional organic small molecule tpd as hole transport layer. *Appl. Phys. Lett.* **118**(18), 183301 (2021). <https://doi.org/10.1063/5.0050512>
129. B. Li, K. Yang, Q. Liao, Y. Wang, M. Su et al., Imide-functionalized triarylamine-based donor-acceptor polymers as hole transporting layers for high-performance inverted perovskite solar cells. *Adv. Funct. Mater.* **31**(21), 2100332 (2021). <https://doi.org/10.1002/adfm.202100332>
130. S. Ma, X. Zhang, X. Liu, R. Ghadari, M. Cai et al., Pyridine-triphenylamine hole transport material for inverted perovskite solar cells. *J. Energy Chem.* **54**, 395–402 (2021). <https://doi.org/10.1016/j.ijechem.2020.06.002>
131. L. Gao, C. Ma, S. Wei, A.V. Kuklin, H. Zhang et al., Applications of few-layer Nb₂C MXene: narrow-band photodetectors and femtosecond mode-locked fiber lasers. *ACS Nano* **15**(1), 954–965 (2021). <https://doi.org/10.1021/acsnano.0c07608>
132. O. Mashtalir, M.R. Lukatskaya, M.-Q. Zhao, M.W. Barsoum, Y. Gogotsi, Amine-assisted delamination of Nb₂C MXene for Li-ion energy storage devices. *Adv. Mater.* **27**(23), 3501–3506 (2015). <https://doi.org/10.1002/adma.201500604>
133. Y. Liu, P. Stradins, S.-H. Wei, Van der waals metal-semiconductor junction: weak fermi level pinning enables effective tuning of schottky barrier. *Sci. Adv.* **2**(4), e1600069 (2016). <https://doi.org/10.1126/sciadv.1600069>
134. J. Zhang, C. Huang, H. Yu, Modulate the work function of Nb₂C_x MXene as the hole transport layer for perovskite solar cells. *Appl. Phys. Lett.* **119**(3), 033506 (2021). <https://doi.org/10.1063/5.0057978>
135. S. Saha, A.K. Bhowmick, Computer simulation of thermo-plastic elastomers from rubber-plastic blends and comparison with experiments. *Polymer* **103**, 233–242 (2016). <https://doi.org/10.1016/j.polymer.2016.09.065>
136. Y. Xie, C.A.S. Hill, Z. Xiao, H. Militz, C. Mai, Silane coupling agents used for natural fiber/polymer composites: a review. *Compos. A: Appl. Sci. Manuf.* **41**(7), 806–819 (2010). <https://doi.org/10.1016/j.compositesa.2010.03.005>
137. H. Zhu, J. Liang, J. Xu, M. Bo, J. Li et al., Research on anti-chloride ion penetration property of crumb rubber concrete at different ambient temperatures. *Constr. Build. Mater.* **189**, 42–53 (2018). <https://doi.org/10.1016/j.conbuildmat.2018.08.193>
138. J. Yu, N. Wang, M. Wang, J. Zhang, D. Hou, Recyclable rubber-cement composites produced by interfacial strengthened strategy from polyvinyl alcohol. *Constr. Build. Mater.* **264**, 120541 (2020). <https://doi.org/10.1016/j.conbuildmat.2020.120541>
139. J.-B. Du, L. Yang, X. Jin, C.-L. Liu, H.-H. Wang et al., Spray deposition of vinyl tris(2-methoxyethoxy) silane-doped Ti₃C₂T_x mxene hole transporting layer for planar perovskite solar cells. *J. Alloy Compd.* **900**, 163372 (2022). <https://doi.org/10.1016/j.jallcom.2021.163372>
140. Z.-K. Yu, W.-F. Fu, W.-Q. Liu, Z.-Q. Zhang, Y.-J. Liu et al., Solution-processed CuOx as an efficient hole-extraction layer for inverted planar heterojunction perovskite solar cells. *Chinese Chem. Lett.* **28**(1), 13–18 (2017). <https://doi.org/10.1016/j.ccllet.2016.06.021>
141. W. Hu, T. Liu, X. Yin, H. Liu, X. Zhao et al., Hematite electron-transporting layers for environmentally stable planar perovskite solar cells with enhanced energy conversion and lower hysteresis. *J. Mater. Chem. A* **5**(4), 1434–1441 (2017). <https://doi.org/10.1039/C6TA09174A>
142. S. Ye, W. Sun, Y. Li, W. Yan, H. Peng et al., CuscN-based inverted planar perovskite solar cell with an average pce of 15.6%. *Nano Lett.* **15**(6), 3723–3728 (2015). <https://doi.org/10.1021/acs.nanolett.5b00116>

143. J. You, L. Meng, T.-B. Song, T.-F. Guo, Y. Yang et al., Improved air stability of perovskite solar cells via solution-processed metal oxide transport layers. *Nat. Nanotechnol.* **11**(1), 75–81 (2016). <https://doi.org/10.1038/nnano.2015.230>
144. Y. Guo, C. Liu, K. Inoue, K. Harano, H. Tanaka et al., Enhancement in the efficiency of an organic–inorganic hybrid solar cell with a doped P3HT hole-transporting layer on a void-free perovskite active layer. *J. Mater. Chem. A* **2**(34), 13827–13830 (2014). <https://doi.org/10.1039/C4TA02976C>
145. L. Hu, L. Zhang, W. Ren, C. Zhang, Y. Wu et al., High efficiency perovskite solar cells with PTAA hole transport layer enabled by PMMA:F4-TCNQ buried interface layer. *J. Mater. Chem. C* **10**(26), 9714–9722 (2022). <https://doi.org/10.1039/D2TC01494G>
146. Y.S. Kwon, J. Lim, H.-J. Yun, Y.-H. Kim, T. Park, A diketopyrrolopyrrole-containing hole transporting conjugated polymer for use in efficient stable organic–inorganic hybrid solar cells based on a perovskite. *Energy Environ. Sci.* **7**(4), 1454–1460 (2014). <https://doi.org/10.1039/C3EE44174A>
147. J. Liu, M. Durstock, L. Dai, Graphene oxide derivatives as hole- and electron-extraction layers for high-performance polymer solar cells. *Energy Environ. Sci.* **7**(4), 1297–1306 (2014). <https://doi.org/10.1039/C3EE42963F>
148. L. Lu, T. Xu, W. Chen, J.M. Lee, Z. Luo et al., The role of n-doped multiwall carbon nanotubes in achieving highly efficient polymer bulk heterojunction solar cells. *Nano Lett.* **13**(6), 2365–2369 (2013). <https://doi.org/10.1021/nl304533j>
149. Y. Liu, G.-D. Li, L. Yuan, L. Ge, H. Ding et al., Carbon-protected bimetallic carbide nanoparticles for a highly efficient alkaline hydrogen evolution reaction. *Nanoscale* **7**(7), 3130–3136 (2015). <https://doi.org/10.1039/C4NR06295G>
150. C. Xu, L. Wang, Z. Liu, L. Chen, J. Guo et al., Large-area high-quality 2d ultrathin Mo₂C superconducting crystals. *Nat. Mater.* **14**(11), 1135–1141 (2015). <https://doi.org/10.1038/nmat4374>
151. Y.J. Heo, J.W. Lee, Y.R. Son, J.H. Lee, C.S. Yeo et al., Large-scale conductive yarns based on twistable korean traditional paper (Hanji) for supercapacitor applications: toward high-performance paper supercapacitors. *Adv. Energy Mater.* **8**(27), 1801854 (2018). <https://doi.org/10.1002/aenm.201801854>
152. Y.-J. Heo, J.-H. Lee, S.-H. Kim, S.-J. Mun, S.-Y. Lee et al., Derived millimeter-thick yarn supercapacitors enabling high volumetric energy density. *ACS Appl. Mater. Interfaces* **14**(37), 42671–42682 (2022). <https://doi.org/10.1021/acsami.2c10746>
153. S. Hussain, H. Liu, D. Vikraman, M. Hussain, S.H.A. Jaffery et al., Characteristics of Mo₂C-CNTs hybrid blended hole transport layer in the perovskite solar cells and X-ray detectors. *J. Alloy Compd.* **885**, 161039 (2021). <https://doi.org/10.1016/j.jallcom.2021.161039>
154. S. Hussain, H. Liu, M. Hussain, M.T. Mehran, H.-S. Kim et al., Development of MXene/WO₃ embedded pedot:PSS hole transport layers for highly efficient perovskite solar cells and X-ray detectors. *Int. J. Energ. Res.* **46**(9), 12485–12497 (2022). <https://doi.org/10.1002/er.8020>
155. H. Li, G. Tong, T. Chen, H. Zhu, G. Li et al., Interface engineering using a perovskite derivative phase for efficient and stable CsPbBr₃ solar cells. *J. Mater. Chem. A* **6**(29), 14255–14261 (2018). <https://doi.org/10.1039/C8TA03811B>
156. H. Yuan, Y. Zhao, J. Duan, Y. Wang, X. Yang et al., All-inorganic CsPbBr₃ perovskite solar cell with 10.26% efficiency by spectra engineering. *J. Mater. Chem. A* **6**(47), 24324–24329 (2018). <https://doi.org/10.1039/C8TA08900K>
157. J. Cao, F. Meng, L. Gao, S. Yang, Y. Yan et al., Alternative electrodes for htmcs and noble-metal-free perovskite solar cells: 2d MXenes electrodes. *RSC Adv.* **9**(59), 34152–34157 (2019). <https://doi.org/10.1039/C9RA06091J>
158. G. Tong, X. Geng, Y. Yu, L. Yu, J. Xu et al., Rapid, stable and self-powered perovskite detectors via a fast chemical vapor deposition process. *RSC Adv.* **7**(30), 18224–18230 (2017). <https://doi.org/10.1039/C7RA01430A>
159. S.N. Habisreutinger, R.J. Nicholas, H.J. Snaith, Carbon nanotubes in perovskite solar cells. *Adv. Energy Mater.* **7**(10), 1601839 (2017). <https://doi.org/10.1002/aenm.201601839>
160. T. Chen, G. Tong, E. Xu, H. Li, P. Li et al., Accelerating hole extraction by inserting 2D Ti₃C₂-MXene interlayer to all inorganic perovskite solar cells with long-term stability. *J. Mater. Chem. A* **7**(36), 20597–20603 (2019). <https://doi.org/10.1039/C9TA06035A>
161. L. Mi, Y. Zhang, T. Chen, E. Xu, Y. Jiang, Carbon electrode engineering for high efficiency all-inorganic perovskite solar cells. *RSC Adv.* **10**(21), 12298–12303 (2020). <https://doi.org/10.1039/D0RA00288G>
162. T.M. Barnes, M.O. Reese, J.D. Bergeson, B.A. Larsen, J.L. Blackburn et al., Comparing the fundamental physics and device performance of transparent, conductive nanostructured networks with conventional transparent conducting oxides. *Adv. Energy Mater.* **2**(3), 353–360 (2012). <https://doi.org/10.1002/aenm.201100608>
163. B.-H. Jiang, H.-E. Lee, J.-H. Lu, T.-H. Tsai, T.-S. Shieh et al., High-performance semitransparent organic photovoltaics featuring a surface phase-matched transmission-enhancing Ag/ITO electrode. *ACS Appl. Mater. Interfaces* **12**(35), 39496–39504 (2020). <https://doi.org/10.1021/acsami.0c10906>
164. H. Wang, Y. Guo, L. He, L. Kloo, J. Song et al., Efficient naphthalene imide-based interface engineering materials for enhancing perovskite photovoltaic performance and stability. *ACS Appl. Mater. Interfaces* **12**(37), 42348–42356 (2020). <https://doi.org/10.1021/acsami.0c11620>
165. S.J. Lee, S.H. Lee, H.W. Kang, S. Nahm, B.H. Kim et al., Flexible electrochromic and thermochromic hybrid smart window based on a highly durable ITO/graphene transparent electrode. *Chem. Eng. J.* **416**, 129028 (2021). <https://doi.org/10.1016/j.cej.2021.129028>
166. X. Zhang, V.A. Öberg, J. Du, J. Liu, E.M.J. Johansson, Extremely lightweight and ultra-flexible infrared light-converting quantum dot solar cells with high power-per-weight output using a solution-processed bending durable silver

- nanowire-based electrode. *Energy Environ. Sci.* **11**(2), 354–364 (2018). <https://doi.org/10.1039/C7EE02772A>
167. J. Han, J. Yang, W. Gao, H. Bai, Ice-templated, large-area silver nanowire pattern for flexible transparent electrode. *Adv. Funct. Mater.* **31**(16), 2010155 (2021). <https://doi.org/10.1002/adfm.202010155>
168. S. Lee, J. Jang, T. Park, Y.M. Park, J.S. Park et al., Electrodeposited silver nanowire transparent conducting electrodes for thin-film solar cells. *ACS Appl. Mater. Interfaces* **12**(5), 6169–6175 (2020). <https://doi.org/10.1021/acsami.9b17168>
169. M.-R. Azani, A. Hassanpour, T. Torres, Benefits, problems, and solutions of silver nanowire transparent conductive electrodes in indium tin oxide (ITO)-free flexible solar cells. *Adv. Energy Mater.* **10**(48), 2002536 (2020). <https://doi.org/10.1002/aenm.202002536>
170. Y. Yang, B. Xu, J. Hou, Solution-processed silver nanowire as flexible transparent electrodes in organic solar cells. *Chin. J. Chem.* **39**(8), 2315–2329 (2021). <https://doi.org/10.1002/cjoc.202000696>
171. J. Han, S. Yuan, L. Liu, X. Qiu, H. Gong et al., Fully indium-free flexible Ag nanowires/ZnO: F composite transparent conductive electrodes with high haze. *J. Mater. Chem. A* **3**(10), 5375–5384 (2015). <https://doi.org/10.1039/C4TA05728G>
172. T. Lei, R. Peng, W. Song, L. Hong, J. Huang et al., Bendable and foldable flexible organic solar cells based on Ag nanowire films with 10.30% efficiency. *J. Mater. Chem. A* **7**(8), 3737–3744 (2019). <https://doi.org/10.1039/C8TA11293B>
173. A.G. Ricciardulli, S. Yang, G.-J.A.H. Wetzelaer, X. Feng, P.W.M. Blom, Hybrid silver nanowire and graphene-based solution-processed transparent electrode for organic optoelectronics. *Adv. Funct. Mater.* **28**(14), 1706010 (2018). <https://doi.org/10.1002/adfm.201706010>
174. X. Meng, X. Hu, X. Yang, J. Yin, Q. Wang et al., Roll-to-roll printing of meter-scale composite transparent electrodes with optimized mechanical and optical properties for photoelectronics. *ACS Appl. Mater. Interfaces* **10**(10), 8917–8925 (2018). <https://doi.org/10.1021/acsami.8b00093>
175. J. Zhang, N. Kong, S. Uzun, A. Levitt, S. Seyedin et al., Scalable manufacturing of free-standing, strong $\text{Ti}_3\text{C}_2\text{T}_x$ mxene films with outstanding conductivity. *Adv. Mater.* **32**(23), 2001093 (2020). <https://doi.org/10.1002/adma.202001093>
176. W. Chen, R. Zhang, X. Yang, H. Wang, H. Yang et al., A 1D:2D structured agnw: Mxene composite transparent electrode with high mechanical robustness for flexible photovoltaics. *J. Mater. Chem. C* **10**(22), 8625–8633 (2022). <https://doi.org/10.1039/D2TC01178F>
177. X. Fan, Doping and design of flexible transparent electrodes for high-performance flexible organic solar cells: recent advances and perspectives. *Adv. Funct. Mater.* **31**(8), 2009399 (2021). <https://doi.org/10.1002/adfm.202009399>
178. A. Di Vito, A. Pecchia, M. Auf der Maur, A. Di Carlo, Nonlinear work function tuning of lead-halide perovskites by MXenes with mixed terminations. *Adv. Funct. Mater.* **30**(47), 1909028 (2020). <https://doi.org/10.1002/adfm.201909028>
179. A. Agresti, A. Pazniak, S. Pescetelli, A. Di Vito, D. Rossi et al., Titanium-carbide mxenes for work function and interface engineering in perovskite solar cells. *Nat. Mater.* **18**(11), 1228–1234 (2019). <https://doi.org/10.1038/s41563-019-0478-1>
180. X. Chen, W. Xu, N. Ding, Y. Ji, G. Pan et al., Dual interfacial modification engineering with 2D mxene quantum dots and copper sulphide nanocrystals enabled high-performance perovskite solar cells. *Adv. Funct. Mater.* **30**(30), 2003295 (2020). <https://doi.org/10.1002/adfm.202003295>
181. A.S.R. Bati, M. Hao, T.J. Macdonald, M. Batmunkh, Y. Yamauchi et al., 1D–2D synergistic mxene-nanotubes hybrids for efficient perovskite solar cells. *Small* **17**(32), 2101925 (2021). <https://doi.org/10.1002/sml.202101925>
182. C. Wu, W. Fang, Q. Cheng, J. Wan, R. Wen et al., Mxene-regulated perovskite vertical growth for high-performance solar cells. *Angew. Chem. Int. Ed.* **61**(43), e202210970 (2022). <https://doi.org/10.1002/anie.202210970>
183. S. Liu, D. Zhou, X. Zhuang, R. Sun, H. Zhang et al., Interfacial Engineering of Au@Nb₂CT_x-MXene modulates the growth strain, suppresses the auger recombination, and enables an open-circuit voltage of over 1.2 V in perovskite solar cells. *ACS Appl. Mater. Interfaces* **15**, 3961–3973 (2023). <https://doi.org/10.1021/acsami.2c18362>
184. M. Jeong, I.W. Choi, E.M. Go, Y. Cho, M. Kim et al., Stable perovskite solar cells with efficiency exceeding 24.8% and 0.3-V voltage loss. *Science* **369**(6511), 1615–1620 (2020). <https://doi.org/10.1126/science.abb7167>
185. D. Xu, T. Li, Y. Han, X. He, S. Yang et al., Fluorine functionalized mxene QDs for near-record-efficiency CsPbI₃ solar cell with high open-circuit voltage. *Adv. Funct. Mater.* **32**(33), 2203704 (2022). <https://doi.org/10.1002/adfm.202203704>
186. P. Guo, C. Liu, X. Li, Z. Chen, H. Zhu et al., Laser manufactured nano-mxenes with tailored halogen terminations enable interfacial ionic stabilization of high performance perovskite solar cells. *Adv. Energy Mater.* (2022). <https://doi.org/10.1002/aenm.202202395>
187. T. Leijtens, G.E. Eperon, S. Pathak, A. Abate, M.M. Lee et al., Overcoming ultraviolet light instability of sensitized TiO₂ with meso-superstructured organometal tri-halide perovskite solar cells. *Nat. Commun.* **4**(1), 2885 (2013). <https://doi.org/10.1038/ncomms3885>
188. Q. Jiang, X. Zhang, J. You, SnO₂: a wonderful electron transport layer for perovskite solar cells. *Small* **14**(31), 1801154 (2018). <https://doi.org/10.1002/sml.201801154>
189. Q. Liu, M.-C. Qin, W.-J. Ke, X.-L. Zheng, Z. Chen et al., Enhanced stability of perovskite solar cells with low-temperature hydrothermally grown SnO₂ electron transport layers. *Adv. Funct. Mater.* **26**(33), 6069–6075 (2016). <https://doi.org/10.1002/adfm.201600910>
190. Y. Wang, P. Xiang, A. Ren, H. Lai, Z. Zhang et al., Mxene-modulated electrode/SnO₂ interface boosting charge transport in perovskite solar cells. *ACS Appl. Mater. Interfaces* **12**(48),

- 53973–53983 (2020). <https://doi.org/10.1021/acsami.0c17338>
191. L. Yang, B. Wang, C. Dall'Agnese, Y. Dall'Agnese, G. Chen et al., Hybridization of SnO₂ and an in-situ-oxidized Ti₃C₂Tx mxene electron transport bilayer for high-performance planar perovskite solar cells. *ACS Sustain. Chem. Eng.* **9**(40), 13672–13680 (2021). <https://doi.org/10.1021/acssuschemeng.1c05245>
192. S.A.A. Shah, M.H. Sayyad, K. Khan, J. Sun, Z. Guo, Application of mxenes in perovskite solar cells: a short review. *Nano Mater.* **11**(8), 2151 (2021). <https://doi.org/10.3390/nano11082151>
193. Z. Liu, H.N. Alshareef, MXenes for optoelectronic devices. *Adv. Electr. Mater.* **7**(9), 2100295 (2021). <https://doi.org/10.1002/aelm.202100295>
194. J. Ghosh, P.K. Giri, Recent advances in perovskite/2D Materials based hybrid photodetectors. *J. Phys. Mater.* **4**(3), 032008 (2021). <https://doi.org/10.1088/2515-7639/abf544>
195. Y. Zheng, Y. Wang, Z. Li, Z. Yuan, S. Guo et al., MXene quantum dots/perovskite heterostructure enabling highly specific ultraviolet detection for skin prevention. *Matter* **6**(2), 506–520 (2023). <https://doi.org/10.1016/j.matt.2022.11.020>
196. Z. Liu, J.K. El-Demellawi, O.M. Bakr, B.S. Ooi, H.N. Alshareef, Plasmonic Nb₂CTx MXene-MaPbI₃ heterostructure for self-powered visible-NIR photodiodes. *ACS Nano* **16**(5), 7904–7914 (2022). <https://doi.org/10.1021/acsnano.2c00558>

